UNIVERSITÀ DEGLI STUDI DI TRIESTE

XXVIII CICLO DEL DOTTORATO DI RICERCA IN NANOTECNOLOGIE

NOVEL BIOMATERIALS FOR INNOVATIVE THERAPIES IN THE SEVERE WOUNDS TREATMENT

Settore scientifico-disciplinare: BIO/10 - BIOCHIMICA

DOTTORANDO
PASQUALE SACCO

COORDINATORE
PROF. LUCIA PASQUATO
SUPERVISORE DI TESI
DR. ELEONORA MARSICH
TUTORE
DR. MASSIMILIANO BORGOGNA

ANNO ACCADEMICO 2014 / 2015

UNIVERSITÀ DEGLI STUDI DI TRIESTE

XXVIII CICLO DEL DOTTORATO DI RICERCA IN NANOTECNOLOGIE

NOVEL BIOMATERIALS FOR INNOVATIVE THERAPIES IN THE SEVERE WOUNDS TREATMENT

Settore scientifico-disciplinare: BIO/10 - BIOCHIMICA

DOTTORANDO
PASQUALE SACCO

COORDINATORE
PROF. LUCIA PASQUATO
SUPERVISORE DI TESI
DR. ELEONORA MARSICH
TUTORE
DR. MASSIMILIANO BORGOGNA

ANNO ACCADEMICO 2014 / 2015

I'd like to thank all the people who have fostered me along the whole Ph.D. First of all I'd like to thank Prof. Sergio Paoletti for giving me the possibility to pursue the doctoral degree in the Biomaterials Lab. I'd like to thank my supervisor Dr. Eleonora Marsich and Dr. Ivan Donati for the incredible support in the experimental activity and scientific discussions in these years: you opened my mind to different views. I'd like to thank Dr. Massimiliano Borgogna and Dr. Andrea Travan for their precious suggestions during my scientific growth. I'd like to thank my colleagues, Davide, Francesca, Michela, Lorena and Federica for sharing hours and hours in the Lab. and several funny adventures in a perfect peacefulness atmosphere. I owe a lot to all of Biomat people for making me feel part of this beautiful group.

I'd like to thank my supervisor at NTNU (Trondheim) Prof. Kjell Morten Vårum for hosting me at the Department of Biotechnology and for taking care of me as a son; he is thanked also for the precious suggestions about science and life, I'll never forget it. I'd like to thank even my colleagues at NTNU, Georg, Olha, Kåre, Yiming, Olav, Pavla, Annalucia and Gaston for shearing beautiful moments during my period abroad in Norway.

I'd like to thank my bachelor/master students, Franco, Greta, Fabio and Franco again for helping me in the experimental activity and for debating on different scientific topics. I'd like to thank Dr. Gianluca Turco, Dr. Eva Decleva, Dr. Renzo Menegazzi, Dr. Luca Stucchi, Dr. Alessandra Sechi, Dr. Marco Bosco and everyone I worked with during these years.

Finally I'd like to thank my family and Ilaria, I couldn't have done it without your constant support and love.

Preface

This thesis is submitted in fulfillment to the requirements of the Graduate School of Nanotechnology for the academic title of Ph.D. in Nanotechnology at the University of Trieste. The work has been carried out mainly at the Department of Life Sciences at the University of Trieste under the supervision of Dr. Eleonora Marsich and co-supervised by Dr. Massimiliano Borgogna, and at the Department of Biotechnology at the Norwegian University of Science and Technology (NTNU), Trondheim, Norway, under the supervision of Prof. Kjell Morten Vårum. Part of the activity was performed in collaboration with Sigea Srl, Padriciano (TS), Italy. This work was supported by the Friuli-Venezia Giulia Regional Government (Project: "Nuovi biomateriali per terapie innovative nel trattamento delle ferite difficili"-LR 47/78) and by the Italian Ministry of University and Research MIUR (PRIN 2012, Project "Spinal Injury: Towards the Development of Cell-Instructive Scaffolds for Nerve Tissue Repair"). European Social Fund (S.H.A.R.M. Project-Supporting human assets in research and mobility) and European Cooperation in Science and Technology (COST) are also gratefully acknowledged.

The thesis consists of a general introduction, aim of the study and a detailed discussion of results divided into five chapters.

Summary

Treatment of non-healing wounds represents hitherto a severe dilemma for the healthcare worldwide because of wound failure to recover. The physiological wound healing is in fact a critical process requiring lack of both bacterial contamination and persistent inflammatory events in the damaged site. Despite a broad range of both antimicrobial and anti-inflammatory agents is commercially available, a successful tackling of bacterial infections and chronic inflammation is particularly challenging due to the increase of microbial resistance and remarkable side effects caused by an abuse of drugs. To this end, the development of innovative biomaterials used in combination with alternative agents is very challenging. The goals for the present thesis were to fabricate and characterize in terms of physical, chemical and biological properties, nanoengineered biomaterials to be used in the treatment of severe wounds. The potential use of two polysaccharides, namely chitosan and hyaluronan, and of their derivatives has been investigated.

In the Chapter I is described an innovative method for the production of tridimensional hydrogels based on chitosan and on the cross-linker tripolyphosphate (TPP). The possibility to obtain hydrogels with chitosans with different acetylation degree (Fa) and molecular weight (M_w) was tackled. Resulting hydrogels were studied in terms of mechanical properties. Finally, soft-pliable and biocompatible membranes were obtained by freeze-drying.

Further analyses are accounted in the Chapter II aiming at deeply investigating on hydrogel-forming process. More in detail, the different affinity of cross-linkers TPP and pyrophosphate (PPi) towards chitosan was explored in diluted solutions. The mechanical behavior of resulting hydrogels was further investigated whereas the polymer distribution within matrices has been assessed by both qualitative and quantitative methods.

In the Chapter III the preparation of soft pliable chitosan-based membranes prepared from hydrogels containing antimicrobial silver nanoparticles (AgNPs) stabilized by a lactose-modified chitosan (chitlac) is tackled. A thorough investigation on bactericidal properties of the material revealed the synergistic activity of chitosan and AgNPs to reduce the growth of different bacteria strains and to break apart mature biofilms. Finally, biocompatibility assays on keratinocytes and fibroblasts did not prove any harmful effect on mammalian cells.

The anti-inflammatory behavior of the short chain fatty acid butyrate is discussed in the first part of Chapter IV. Such feature was proved to be time- and dose-dependent. To extend on time and to modulate the biological activity of butyrate, chitosan/hyaluronan-based nanoparticles (complexes) were developed. These *carriers* showed the ability to encapsulate butyrate as payload, an intrinsic scavenging activity, the ability to quickly interact with neutrophils, muco-adhesive properties and lack of cytotoxicity.

In the Chapter V it has been reported the biological investigation of a complex between hyaluronan-lipoate and silver ions (named SHLS12). Biological studies showed the ability of SHLS12 to exert a straightforward bactericidal activity against different bacterial strains grown both in sessile and planktonic state. The lack of toxicity was proved towards mammalian cells. By considering its ability to preserve antibacterial properties when exposed to serum proteins, this complex may be considered as a promising biomaterial for the treatment of non-healing wounds.

Sommario

Il trattamento delle ferite difficili rappresenta ad oggi un grave problema per la sanità a livello mondiale a causa della difficoltà di queste ferite a guarire. La fisiologica guarigione delle ferite è un processo altamente regolato che richiede assenza sia di contaminazione batterica che di una persistente risposta infiammatoria. Nonostante sia disponibile sul mercato un'ampia varietà di agenti antimicrobici e antiinfiammatori, il trattamento delle ferite difficili risulta estremamente difficoltoso a causa dell'aumentata resistenza batterica agli antibiotici e dei numerosi effetti indesiderati dovuti ad un abuso di questi farmaci. A questo scopo, lo sviluppo di biomateriali innovativi preparati in combinazione con agenti alternativi rappresenta un campo di ricerca in espansione. Gli obiettivi per questo lavoro di tesi sono stati di conseguenza quelli di sviluppare e caratterizzare a livello chimico-fisico-biologico biomateriali nano-ingegnerizzati da usare nel trattamento delle ferite difficili. In particolare sono stati presi in considerazione due polisaccaridi, rispettivamente il chitosano e l'acido ialuronico, e loro derivati ingegnerizzati.

Nel Capitolo I viene descritto un metodo innovativo per la preparazione di idrogeli a base di chitosano e del reticolante tripolifosfato (TPP). È stata considerata la possibilità di sviluppare idrogeli utilizzando chitosani con un diverso grado di acetilazione (Fa) e peso molecolare (M_w). Gli idrogeli risultanti sono stati studiati in termini di proprietà meccaniche. In ultimo, sono state sviluppate membrane flessibili e biocompatibili attraverso congelamento e liofilizzazione degli idrogeli.

Ulteriori analisi per elucidare il processo di formazione degli idrogeli sono riportate nel Capitolo II. Nel dettaglio, è stata valutata la differente affinità nei confronti del chitosano dei reticolanti TPP e pirofosfato (PPi) in sistemi diluiti. In seguito è stato studiato il comportamento meccanico degli idrogeli risultanti mentre la distribuzione del polimero all'interno delle matrici è stata valutata tramite metodi sia qualitativi sia quantitativi.

Nel Capitolo III viene riportata la preparazione di membrane flessibili a base di chitosano a partire da idrogeli che includono nanoparticelle di argento (AgNPs) stabilizzate da un derivato del chitosano (chitlac). Uno studio approfondito sulle proprietà antibatteriche del materiale ha rivelato un'attività sinergica tra il chitosano e le AgNPs nel ridurre la crescita batterica di diversi ceppi e nel disgregare biofilm maturi. In ultimo, saggi di citotossicità non hanno dimostrato alcun effetto negativo sulla vitalità delle cellule eucariotiche.

Nella prima parte del Capitolo IV è riportata l'attività antiinfiammatoria dell'acido grasso a corta catena butirrato. Questa proprietà si è dimostrata sia tempo che dose dipendente. Con l'obiettivo di prolungare e modulare il rilascio e quindi l'effetto biologico del butirrato, sono state sviluppate nanoparticelle (complessi) a base di chitosano e acido ialuronico. Tali *carriers* hanno mostrato l'abilità di incapsulare il butirrato, una intrinseca attività antiossidante, l'abilità di interagire velocemente con i neutrofili, proprietà mucoadesive ed assenza di citotossicità.

Nel Capitolo V è riportato lo studio sulle proprietà biologiche di un complesso tra argento ionico e un derivato lipoato dell'acido ialuronico, definito SHLS12. Gli studi biologici hanno mostrato l'abilità di SHLS12 di esercitare un'importante attività battericida nei confronti di diversi ceppi batterici cresciuti sia in stato sessile che planctonico. L'assenza di citotossicità è stata dimostrata con cellule eucariotiche. Considerando la sua caratteristica di mantenere proprietà antibatteriche quando è in contatto con proteine del siero, questo complesso di argento può essere considerato come un biomateriale promettente per il trattamento delle ferite difficili.

List of Papers

1. **Pasquale Sacco**, Massimiliano Borgogna, Andrea Travan, Eleonora Marsich, Sergio Paoletti, Fioretta Asaro, Mario Grassi and Ivan Donati. "Polysaccharide-Based Networks from Homogeneous Chitosan-Tripolyphosphate Hydrogels: Synthesis and Characterization". Biomacromolecules, 2014; 15:3396–405.

2. **Pasquale Sacco**, Andrea Travan, Massimiliano Borgogna, Sergio Paoletti and Eleonora Marsich. "Silver-containing antimicrobial membrane based on chitosan-TPP hydrogel for the treatment of wounds". Journal of Materials Science: Materials in Medicine, 2015; 26 (3):128.

3. **Pasquale Sacco**, Alessandra Sechi, Antonia Trevisan, Fabrizio Picotti, Rita Gianni, Luca Stucchi, Matteo Fabbian, Marco Bosco, Sergio Paoletti and Eleonora Marsich. "A silver complex of hyaluronan-lipoate (SHLS12): synthesis, characterization and biological properties". Carbohydrate Polymers, 2016; 136:418-426.

4. **Pasquale Sacco**, Sergio Paoletti, Michela Cok, Fioretta Asaro, Michela Abrami, Mario Grassi and Ivan Donati. "Insight into the Ionotropic Gelation of Chitosan. Interaction with Tripolyphosphate and Pyrophosphate in Dilute Solution and formation of Tridimensional Hydrogels ". Submitted manuscript to Biomacromolecules.

5. **Pasquale Sacco**, Eva Decleva, Fabio Tentor, Massimiliano Borgogna, Renzo Menegazzi, Sergio Paoletti, Kjell Morten Vårum and Eleonora Marsich. "Chitosan-hyaluronan nanoparticles can control the leakage of butyrate as an anti-inflammatory molecule". Manuscript in preparation.

Contributions to other publications not included in the thesis:

1. Ruggero Angelico, Andrea Ceglie, **Pasquale Sacco**, Giuseppe Colafemmina, Maria Ripoli and Alessandra Mangia. "Phyto-liposomes as nanoshuttles for water-insoluble silybin-phospholipid complex". International Journal of Pharmaceutics, 2014; 471:173–81.

2. Maria Ripoli, Ruggero Angelico, **Pasquale Sacco**, Andrea Ceglie and Alessandra Mangia. "Phytoliposome-based silibinin delivery system as a promising strategy to prevent Hepatitis C virus infection". Journal of Biomedical Nanotechnology. Accepted manuscript.

Symbols and abbreviations

PDGF	Platelet-derived growth factor
TGF-β	Transforming growth factor-beta
FGFs	Fibroblast growth factors
IL-1	Interleukin-1
IL-6	Interleukin-6
TNF-α	Tumor necrosis factor-alpha
VEGF	Vascular endothelial growth factor
MMP	Matrix metalloproteinase
IgG	Immunoglobulin-G
EPS	Extracellular polymeric substance
PMIC	Minimum inhibitor concentration
MRSA	Methicillin-resistant *Staphylococcus aureus*
AgNPs	Silver nanoparticles
PMN	Neutrophilic polymorphonuclear leukocytes
ROS	Reactive oxygen species
SCFA	Short chain fatty acid
Fa	Fraction of N-acetylglucosamine units
M_n	Number average molecular mass
M_w	Weight average molecular mass
[η]	Intrinsic viscosity
PI	Polidispersity index
TPP	Tripolyphosphate
PPi	Pyrophosphate
B-NPs	Butyrate loaded chitosan/hyaluronan nanoparticles
SHLS12	Silver complex of hyaluronan-lipoate
SEC-MALLS	Size exclusion chromatography with multi-angle laser light scattering
NMR	Nuclear magnetic resonance spectroscopy
DLS	Dynamic light scattering
FTIR-ATR	Attenuated total reflectance fourier transform infrared spectroscopy
CD	Circular dichroism
TEM	Transmission electron microscopy
SEM	Scanning electron microscopy
LSCM	Confocal laser scanning microscopy
UPLC-MS	Ultra Performance Liquid Cromatography-Mass Spectrometry

Table of contents

1. INTRODUCTION

1.1. Wound healing process.

Wound healing is a critical physiological process requiring step-by-step dynamic phases and involving different cells and tissues. Upon tissue damage occurs, sequential time-dependent events are triggered as well as (*a*) hemostasis, (*b*) inflammation, (*c*) proliferation and (*d*) wound remodeling (Figure 1).(*1*)

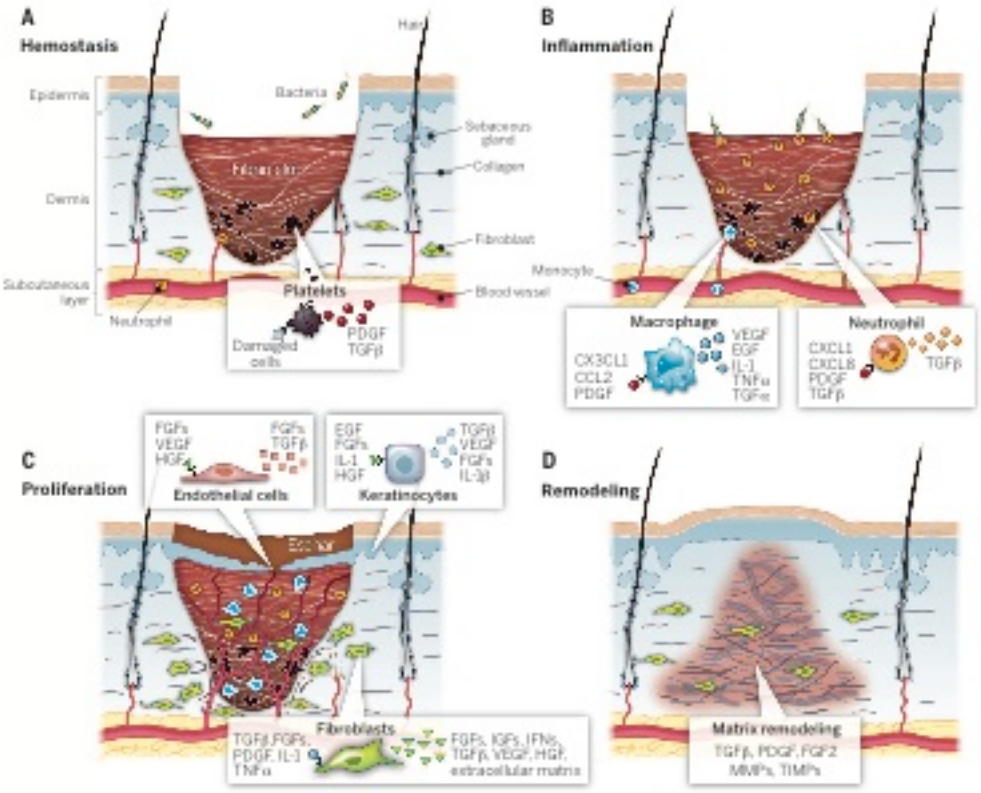

Figure 1. Stages of wound healing. Wound healing is classically divided into four stages: (A) hemostasis, (B) inflammation, (C) proliferation, and (D) remodeling. Each stage involves a plethora of both molecular and cellular events and is finely balanced by secreted factors that are recognized and released by the cells of the wounding response. A representative subset of major factors involved are pointed out. PDGF, platelet-derived growth factor; TGF, transforming growth factor; FGFs, fibroblast growth factors; IL-1, interleukin-1; TNF, tumor necrosis factor; KGF, keratinocyte growth factor; IGF, insulin-like growth factor; IFN, interferon; VEGF, vascular endothelial growth factor; HGF, hepatocyte growth factor; MMP, matrix metalloproteinase; TIMP, tissue inhibitor of metalloproteinase. From (*1*). Reprinted with permission from AAAS.

1.1.1. Hemostasis

Hemostasis represents the early phase of wound healing occurring immediately after the lesion. The main purpose is to dampen bleedings in order to protect other organs. The second aim deals with the production of an extracellular matrix able to host different cell types which will take over in the later phases of healing.(*2*),(*3*),(*4*) The hemostasis and the amount of fibrin settled to the lesion site are strictly governed by different cells and processes as well as endothelial cells, thrombocytes, coagulation, and fibrinolysis so as to modulate the final healing of wound. Different insults may induce micro vascular injury and bleeding throughout the wound. Damaged vessels quickly constrict because of the contraction of vascular smooth muscle cells in the circular muscle layer. This event is sufficiently intense to prevent blood extravasation from a thin artery. In spite of this, hemostasis works efficiently only in transversally interrupted vessels where may contribute to completely impair bleeding. At variance, if vessels are cut longitudinally, the system may not work properly by increasing the breach.(*2*) In any case, vasoconstriction can block, or at least dampen, the extravasation provisionally. Indeed, the vascular smooth muscles are advantageous to allow vasoconstriction only for few minutes. Afterwards, hypoxia and acidosis elicit their relaxation thereby extravasation restarts. As a consequence, vasoconstriction is ineffective to stop bleeding when the insult is persistent or unsolved.

Coagulation cascade is activated together with hemostatic events by both extrinsic and intrinsic pathways, causing the aggregation of blood platelet and the clot formation so as limiting the leakage of blood from vessels.(*4*),(*3*) More in detail, blood components and platelets interplay with the extracellular matrix at the wound level thereby inducing the release of clotting factors and the consequent formation of blood clot composed by fibronectin, fibrin, vitronectin, and thrombospondin.(*5*) Resulting clot is suitable not only for the hemostasis process but even for the migration of cells by behaving as support in the later inflammatory phase. The wound healing cascade is triggered by growth factors and cytokines present in the α-granules of platelet cytoplasm: these molecules are platelet derived growth factor (PDGF), transforming growth factor-β (TGF-β), epidermal growth factor and insulin-like growth factors.(*5*) Such molecules stimulate and attract different cells as neutrophils, macrophages, endothelial cells and fibroblasts. For instance PDGF boosts the chemotaxis of neutrophils, macrophages, smooth muscle cells and fibroblasts. Moreover, it even elicits the mitogenesis of the fibroblasts and smooth muscle cells. On the

other hand, TGF-β attracts macrophages and stimulates them to secrete additional cytokines including FGF (fibroblast growth factor), PDGF, TNF-α (tumor necrosis alpha) and IL-1 (interleukin-1). TGF-β further enhances fibroblast and smooth muscle cell chemotaxis and modulates collagen and collagenase expression. At the same time vasoactive amines, such as serotonin, are released from the dense bodies of platelet thus favoring vasodilation and increased vascular permeability. Finally, cell membrane-derived products as well as eicosanoids are leaked after the lesion contributing to subsequent inflammatory phase.(*6*)

1.1.2. Inflammation

The main aim of the inflammation is to guarantee an immune barrier against pathogens and it may be temporarily divided into the early and the late response.(*7*)

Early inflammatory phase begins during the last stages of coagulation and it was found to afford different functions. This response elicits the complement cascade and favors the infiltration of neutrophils as shown in Figure 2 throughout the lesion by preventing or eradicating pathogen infections.(*8*)

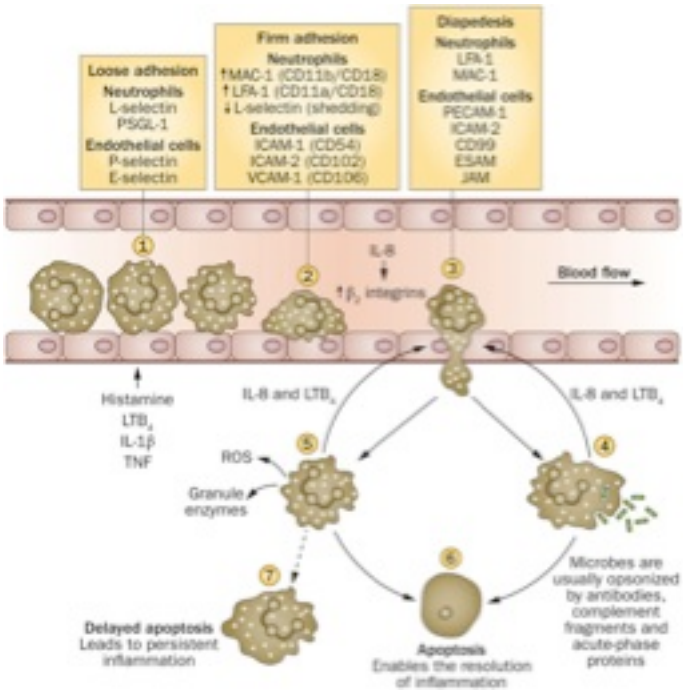

Figure 2. Migration of circulating neutrophils to sites of inflammation or infection. Reprinted by permission from Macmillan Publishers Ltd: *Nature Reviews Rheumatology* (*9*), copyright 2014. Nature Publishing Group is acknowledged. 10.1038/nrrheum.2014.80

Neutrophils are recruited to the wound site within 24-36 hours of injury by several chemoattractive agents as TGF-β, complement components as well as C3a and C5a, and formylmethionyl peptides produced by bacteria and platelet debris.(*6*) The pivotal role for such cells is to eliminate foreign material, bacteria and non-functional host cells and damaged matrix components.(*7*),(*10*) The weapons that neutrophils exploit to perform their role are the phagocytosis activity and the production of ROS. Upon wound occurs, neutrophils start to adhere to the endothelial cells in post-capillary vessels surrounding the lesion through a phase named margination. Later, cells roll along the endothelium moved by the blood stream. Both adhesion and rolling phenomena are due to selectin-dependent interactions between the cells and the endothelium.(*7*),(*11*) Chemical signal derived from endothelial cells immediately stimulate the adhesion of neutrophils mediated by integrins. At this point cells stop to roll and infiltrate throughout endothelium by a phenomenon termed diapedesis.(*7*) Once in the lesion environment, neutrophils may be further stimulated by bacterial signals as the tripeptide called f-Met-Leu-Phe.(*12*) Consequently neutrophils can either swallow pathogens or attack the same releasing proteolytic enzymes and oxygen-derived free radical species. At the end of their activity, neutrophils undergo apoptosis in order to not affect the complete recover of the wound and to dampen the strong pro-inflammatory condition at the lesion site. Apoptotic bodies are finally eliminated by macrophages.(*6*) Mast cells are also involved in wound healing. Mast cells leak granules containing enzymes, histamine and other active amines that contribute to determine the typical signs of inflammation *rubor* (redness), *calor* (heat), *tumor* (swelling) and *dolor* (pain).

By 48 hours after injury, late inflammatory phase starts with the recruitment of monocytes that differentiate into macrophages upon fixed to the inflamed tissue. More in detail, monocytes undergo phenotypic changes until to transform macrophages. The latter are attracted by a plethora of molecules as clotting factors, complement components, PDGF, TGF-β, leukotriene B_4, platelet factor IV and elastin/collagen debris. At variance with neutrophils, macrophages undergo a lower cellular turnover and their biological activity is still efficient for low value of pH.(*13*),(*14*) Once activated, macrophages release tissue growth factors as TGF-β and mediators as well as TGF-α, heparin binding epidermal growth factor, fibroblast growth factor (FGF) and collagenase boosting the stimulation of keratinocytes, fibroblasts and endothelial cells.(*5*) Macrophages are also responsible for eliminating nonfunctional host cells, bacteria filled neutrophils, damaged matrix, and any

residual bacteria at the wound level. If the activity of macrophages decreases at this stage of inflammation, the physiological wound healing might be compromise causing delayed fibroblast proliferation and maturation, lag angiogenesis implying on altered fibrosis.(*15*) At the end of late inflammatory phase, lymphocytes are recruited about 72 h after the damage by molecules as interleukin-1 (IL-1), complement components and immunoglobulin G (IgG).(*16*) IL-1 modulates even the activation of the collagenase, a pivotal step in the remodeling of collagen, and the regulation of synthesis/degradation of novel extracellular matrix.(*17*)

1.1.3. Proliferation

The proliferative phase represents perhaps the most complicated event in the recovery of wounds because of different events occurring in a very large timeframe. Generally, proliferative phase begins after 72 hours post injury and lasts for about two weeks later. The migration of fibroblasts and the temporary sediment of fibronectin and fibrin as extracellular matrix, together with the formation of the granulation tissue, represent the main processes happening in such phase.

Concerning fibroblast activity, proliferation occurs at the beginning in the wound surrounding tissues during the first 72 hours after injury. Subsequently, TGF-β and PDGF released from inflammatory cells and platelets foster fibroblasts to migrate into the lesion.(*18*) Upon arrived, they start to proliferate and to produce matrix components as hyaluronan, fibronectin, proteoglycans and type 1 and 3 procollagen which are accumulated extracellularly.(*14*) Subsequently, extracellular components are continuously synthetized and accumulated allowing the migration of cells. In the same timeframe, fibroblasts modify their phenotype to myofibroblasts characterized by extend pseudopodia able to interact with the fibronectin and collagen of the extracellular matrix. Once cells reach a notable number, wound contraction takes place due to cell retraction upon extracellular matrix and the lesion tends gradually to narrow. Ended their work, myofibroblasts are eliminated by apoptosis.(*5*)

Another pivotal step belonging to the proliferation phase regards the angiogenesis and the formation of granulation tissue. With respect to the former, angiogenesis is a physiological event involving angiogenic factors secreted from surrounding tissues during the hemostatic phase able either to stimulate endothelial cells (as FGF, vascular endothelial growth factor VEGF, PDGF, angiogenin, TGF-α and TGF-β) or inhibit them (angiostatin and steroids) in a refined balance.(*19*),(*20*) The biological activity played by angiogenic factors deals with

the activation of mitosis, movement and the stimulation of host cells to leak endothelial growth factors and may be recapped into four steps: production of proteases enzymes by endothelial cells thereby damaging the basal lamina of vessels and proceeding throughout the extracellular matrix, chemotaxis, proliferation, remodeling and proliferation.(*5*) At the beginning of wound healing, the lesion site is not provided by vascular supplies; as a consequence, the progression of novel capillaries proceeds by diffusion of unaltered vessels present at the edge of wound and, within few days, the formation of micro-capillaries occurred.(*16*) Such activity is prompted by the ability of cells to follow a chemical gradient of chemotactic agents (endothelial cell growth factor, TGF-α, VEGF, angiopoietin-1, fibrin and lipid growth factors) that stimulate cells to migrate, growth and proliferate.(*21*) Endothelial cells quickly migrate after injury until reaching a slower migration rate afterwards. On the other hand, granulation tissue starts to be evident when macrophages, fibroblasts and vascularized stroma, together with collagen matrix, fibrinogen, fibronectin and hyaluronic acid substitute the fibrin clot above discussed. Granulation tissue converts into scar after collagen accumulation. The proliferation phase ends with the epithelialization involving epithelial cells. By starting from wound margins, a single layer of cells begins to proliferate and consequently to migrate towards the center of the lesion until they are sufficiently close to fully cover the underlying extracellular matrix.

1.1.4. Remodelling

The remodeling phase is considered the last event of the physiological wound healing and its main target concerns the formation of new epithelium and final scar formation. The remodeling of a lesion is strictly governed by fine mechanisms maintaining the correct equilibrium between degradation and synthesis of tissues. Some changes happen mainly at the extracellular matrix level, where the increasing of collagen bundles and the degradation of hyaluronic acid and fibronectin are the pivotal events(*22*) that imply on the rising of the wound tensile strength. In spite of this, the regain of original resistance is never reached and it is variable considering the localization of lesion and its time-recovery. The correct balance among synthesis and degradation lasts up to three weeks(*23*) and it is chiefly due to the metalloproteinase enzymes activity. They are produced by neutrophils, macrophages and fibroblasts at the wound level and are responsible of the collagen degradation. The biological activity of such enzymes is inhibited by inhibitor factors when new matrix deposition occurs.(*24*) New formed collagen bundles are initially disorganized but become

progressively more organized later. On the other hand, fibroblasts interact with extracellular matrix by favoring the wound margins closure. This process is tightly modulated by several factors as well as PDGF, TGF-β, FGF, etc.(*23*) As final steps of physiological wound healing, the density of fibroblasts and macrophages reduces,(*24*) the growth of new vessels stops, blood stream dampens and the metabolic activity at lesion site weakens. The final outcome is a mature scar with increased tensile strength.

1.2. Acute and chronic wounds: an overview

Based on their nature and time-healing process, wounds can be classified as either acute or chronic. The former are considered lesions that fully recover with an expected period spanning from eight to twelve weeks.(*25*) Acute lesions concern to different types of trauma at skin level including mechanical injuries as well as abrasions, wounds due to blades, shootings and surgical incisions. Furthermore, chemical injuries, burns and radiations may be classified as acute wounds as well. Generally, acute wounds heal by either primary or secondary intention. Healing by primary intention may be defined as the recovery of a clean wound without loss of tissue and lack of contamination by pathogens. At variance, healing for second intention is characterized by loss of a limited number of epithelial and connective cells. Such process requires a large amount of granulation tissue and an extended time healing. Conversely, chronic wounds, also known as non-healing wounds, are lesions that do not undergo the normal healing process with an expected partial recovery (and often relapse) beyond twelve weeks.(*26*)

1.3. Non-healing wounds

Non-healing wounds gather a number of pathologies in which topical lesions can be related to a defect or a break in the skin, resulting from physical or thermal damage and pathological conditions. Furthermore, several pathophysiological and metabolic factors might affect the physiological wound healing thereby resulting in a poor recovery. The most common factors that contribute to make the lesion worse include edema, ischemia, tissue hypoxia, infection, necrosis, growth factors imbalance, metabolic diseases and pre-existing illness. In this context, all phases occurring during the wound healing (ranging from inflammatory phase to extracellular matrix deposition) are hindered. Alterations derived from one or more aforementioned pathologies affecting the wound repair by impairing the recovery and turning an acute lesion into a chronic one. This pathological

condition is worldwide diffused, with an incidence of the 0.78% of the population, mostly affected elders over the age of sixty.(*27*) As the life expectancy tends to increase, the number of chronic wounds are expected to rise by negatively implying on the costs for the healthcare.(*28*) For instance, the cost related to non-healing ulcers has been estimated at 25 billion dollars annually in the United States.(*29*) Chronic wounds may be classified as pressure sores, diabetic ulcers, venous ulcers, burns and ulcers secondary to ischemia. Moreover, these lesions can even categorized considering either the number or the amount of area of skin strata involved.(*30*),(*31*) Non-healing wounds do not recover because of mainly three aspects: the excessive production of exudates, the presence of bacteria and the persistent inflammatory response. The excessive production of exudates leads to the progressively damage of healthy tissues surrounding the wound thus impairing the correct healing.(*32*) Specifically, chronic wounds exudates are characterized by the presence of proteinase enzymes which contribute to make the lesion worse following to their corrosive activity.(*33*) Nevertheless, the colonization of bacteria both in planktonic and sessile state together with the lengthen inflammation are the pivotal factors causing the worsening of chronic wounds.

1.4. Bacterial infection

Chronic wounds represent a fertile ground for bacteria attachment and consequent proliferation.(*34*),(*35*) Damaged skin exposes underlying tissues to microbial contamination and colonization. As a result, resident or opportunistic bacteria present at the wound level colonize injured sites and enhance their proliferation thereby forming complex surface-attached polymicrobial communities termed biofilm. In fact, chronic wounds represent a suitable site for biofilm formation: the necrotic tissue and debris favor bacteria attachment (*e.g. Staphylococcus aureus* and *Pseudomonas aeruginosa*). The presence of such polymicrobial community often produces severe infections involving both anaerobic and aerobic strains. James *et al*. demonstrated the presence of densely aggregated bacteria colonies surrounded by an extracellular matrix in human wounds: particularly, 60% of chronic wound specimens have proven hosting biofilm.(*36*)

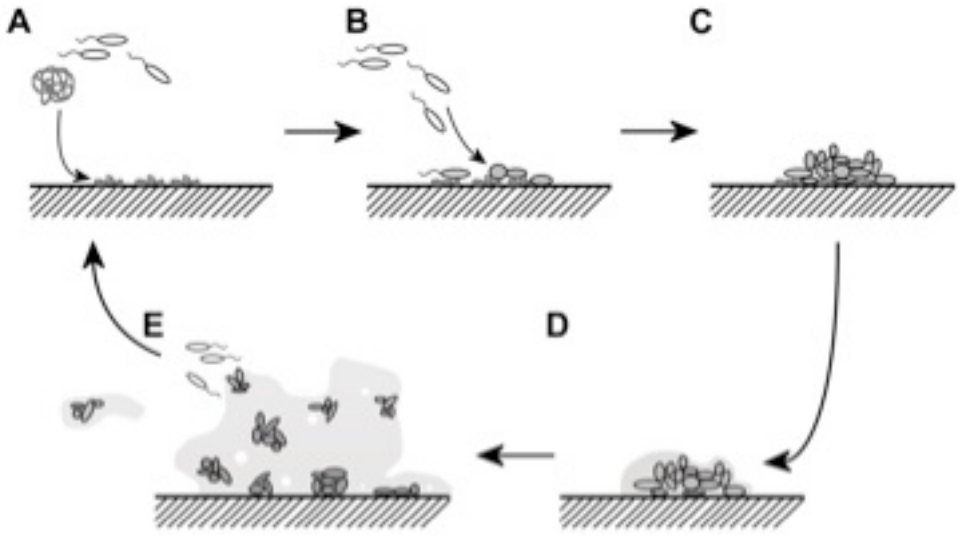

Figure 3. Schematic representation of biofilm formation. (A) Necrotic tissues and debris form a good substrate for planktonic, free-swimming bacteria to adhere to. (B) The sessile bacteria will recruit additional bacteria from the direct environment and also proliferate on the surface. (C) The adhered bacteria change gene expression patterns and start producing the extracellular polymeric substance, the main component of the biofilm. (D) The biofilm slowly grows by forming microcolonies of mono-poly microbial bacteria. (E) Finally, pieces of the biofilm can break off and planktonic bacteria escape from the biofilm and can invade close tissues. Reprinted from (*37*) with permission. Dr. Knetsch is acknowledged.

From a structural point of view, biofilms are composed by an extracellular polymeric substance (EPS) surrounding the bacterial cells making them one thousand times more resistant to antibiotics and drugs than planktonic ones.(*38*) The thickness of biofilms may span from microns to few millimeters. Mature biofilms are less susceptible than less organized ones to antibiotics treatment. Bacteria in sessile state (biofilm) differ from planktonic ones also in terms of gene expression and interaction with the injured site. Planktonic bacteria engage necrotic tissues and increase in number forming colonies (Figure 3). Afterwards they spread throughout the surface either as single layer or microcolonies detached from the main biofilm.(*39*),(*40*) Generally, biofilms are made up of a single bacterial strain or in some cases by different ones as anticipated above.(*41*) This condition affects negatively the physiological healing process by delaying it. Some phenomena can contribute to the worsening of chronic lesions as well as poor perfusion, presence of a foreign body, pressure, repetitive trauma, hyperglycemia and white blood

dysfunction. About the latter aspect, a compromised immune system clearly does not help biofilm elimination.(*41*),(*42*)

1.5. Antibiotics and antiseptics

Generally, treatment of non-healing wounds requires antibiotics administered either systemically or topically. The most common systemic antibiotics are betalactams, aminoglycosides, macrolides, quinolones, lincosamides, nitrimidazoles and sulfonamides whereas topical ones include mupirocin, fusidic agents, neomycin, polymyxin and bacitracin.(*43*) Antibiotics represent the paramount tool to treat non-healing wounds but the optimal choice of drugs and the duration of therapy is not often well defined.(*44*) Usually, antibiotics have to be used in case of increased bioburden, cellulitis, lymphangitis and lymphadenopathy, osteomyelitis, bacteraemia, systemic inflammatory response syndrome, life-threatening sepsis and multiple organ dysfunction syndrome, immunosuppression and diabetes.(*45*),(*44*) Three main recommendations may be taking into account when antibiotics are chosen in the therapy of chronic lesions: systemic antibiotics should be employed only for clinically infected wounds; antibiotics must to be chosen based on the current microbial epidemiology by avoiding the use of wide-spectrum ones; topical drugs should be employed only to dampen the critical colonization at the wound site. O'Meara *et al*. claimed that there is not any evidence to support the continuous use of systemic antibiotics in specific chronic wounds.(*46*) Different factors may influence the final outcome of antibiotic therapy: the concentration of pathogens at the lesion site as well as ischemia phenomena which hinder drug distribution favoring antimicrobial resistance against antibiotics. For instance, it was already demonstrated in several cases that antibiotics did not reach the minimum inhibitor concentration (MIC) to eradicate, or at least dampen, pathogens at wound level.(*47*) Furthermore, the presence of mature biofilms impairs the penetration of antibiotics towards underlying tissues. Methicillin-resistant *Staphylococcus aureus* (MRSA), vancomycin-resistant enterocci and pseudomonads are the typical strains residing in the chronic wounds.(*44*) Colsky *et al.* reported that up to 50% of chronic leg ulcers in hospitalized patients are infected with MRSA, whilst more than one-third of *Pseudomona aeruginosa* isolates are resistant to ciprofloxacin.(*48*) Given these premises, it is evident that pathogens present in the harsh environment of chronic wounds could not respond to antibiotic therapy thereby producing onset of resistance. The increasing of antibiotic resistance towards a wide range of bacteria strains represents

hitherto a serious problem to be solved. Nevertheless, therapeutic indications about the correct treatment of chronic wounds are not completely figured out and the inappropriate use of systemic antibiotics (together with topical wide-spectrum ones) may lead to the antibiotic resistance onset. Vancomycin is the straightforward example to these considerations: albeit it is the drug of choice for MRSA and other device-related staphylococcal infections, the poor penetrance within staphylococcal biofilms limits its use.(*49*)

Antiseptics are antimicrobial substances used for the treatment of non-healing wounds because of their ability to reduce the possibility of infection and sepsis. Antiseptic agents differ from antibiotics for three aspects: they can be used only topically, they have more than one of mechanism of action and their biological activity is quicker than antibiotics. Ideally, the typical antiseptic should possess some features as well as to guarantee a broad antimicrobial spectrum, to provide a constant supply to the wound site, to be not inactivated by proteins, to be biocompatible and to exhibit low allergenicity. Antiseptics do not cause bacterial resistance, albeit risks about the selection of resistant bacteria exist. In spite of this, no antiseptic-resistant human pathogens have registered hitherto. Conversely, antibiotics display selective bactericidal activity and their abuse evokes transmissible resistance. Mechanisms of action regarding about antiseptics biological activity are addressed to impair bacteria metabolism: disruption of efflux pumps, damage to cell walls and cytoplasmic processes and nuclear alterations.(*50*) Actually, a large number of antiseptics is available in biomedical field including phenolics, hydrogen peroxide, hexachlorophene, cetrimide, benzalkonium salts, potassium permanganate, dilute hypochlorite preparations, povidone iodine, chlorhexidine gluconate, triclosan and silver-releasing agents.(*45*),(*43*),(*51*) For instance, povidone iodine is commonly employed as agent to limit bacterial infections prior to surgery. More in detail, it is a valid antiseptic endowing with a broad-spectrum activity which may be considerably diminished by interaction with proteins. Moreover, *in vitro* and *in vivo* studies reviewed by Kramer demonstrated conflicting results about bactericidal effects and the safety of povidone iodine.(*52*) Concerning such substances, silver represents a good example of antiseptic and it is one of the most studied agents to prevent, control and eradicate bacterial infections at the wound site.

1.6. Silver: benefits and hazards

From centuries silver is well known to exert antibacterial properties towards a wide range of bacteria strains. It is already employed in medical dressings in its ion (Ag^+) or reduced (Ag^0 or AgNPs) nanoparticle-state to face bacterial infections.(*53*) AgNPs span from 1 to 100 nm in size and their physical, chemical, biological features considerably vary based on dimensions because of different surface/volume ratio. Silver nanoparticles are currently used in biomedical field in diagnosis, drug delivery, coatings, medical textiles and wound dressings.(*54*),(*55*),(*56*),(*57*) With the advancement of nanotechnology, nanocrystalline forms of silver can be prepared with variable size and shape by means of reliable methods.(*58*) AgNPs are obtained by physical, chemical and biological methods. Evaporation/condensation and laser ablation are the principal physical techniques to form AgNPs. The former exploits a furnace tube under atmospheric pressure but high-energy usage and long-time working are the main drawbacks for such method. As a matter of fact, laser ablation works by ablating metals in solution without chemical reagents thus producing nano-silver colloids.(*59*) Chemical reduction of silver ions is probably the most common technique to obtain AgNPs. Three components are fundamental to such a purpose: silver salts (for instance silver nitrate), reductants (borohydride, citrate, ascorbate(*60*),(*61*),(*62*)) and capping agents. Capping or stabilize agents are surfactans or polymers containing functional groups as well as polyvinylpyrrolidone, poly(ethylene glycol), poly(methacrylic acid), poly(methyl methacrylate) and biopolymers (chitosan, alginate and chitlac) able to avoid aggregation phenomena. Biosynthesis of AgNPs (green synthesis) is recently gaining appeal due to the growing need of environmentally friendly synthesis methods using mild agents as peptides, carbohydrates, bacteria, fungi, yeast, algae and plants.(*63*),(*64*),(*65*)

Silver-based derivatives are of interest in the biomedical field following to the increasing of bacterial resistance towards many antibiotics as discussed above. The work of Xiu *et al.* identified Ag^+ as the molecular toxicant for bacteria with respect to AgNPs.(*66*) In this context, silver nanoparticles are supposed to be made by a reduced core surrounded by an ion corona. Physical contact of bacteria with such Ag^+ ions, dissolved and released in the environment surrounding the nanoparticles, is at the root of their toxicity toward prokaryotic cells. The antimicrobial mechanisms of action of silver are numerous (Figure 4). For instance, some studies demonstrated that silver proved its toxicity by interaction with bacterial membranes,(*62*),(*67*) likely in correspondence to specific molecular targets

as thiol groups (-SH) of proteins, causing membrane damage.(*68*) Feng *et al.* demonstrated the presence of many small electron-dense granules either surrounding the cell wall or depositing inside the cells, likely deriving from the silver-proteins combination.(*69*) This might impair electron transport throughout the membrane due to its altered permeability. Finally, silver is supposed to bind phosphorus atoms containing DNA and to attack the bacterial respiratory chain.(*69*),(*70*),(*67*)

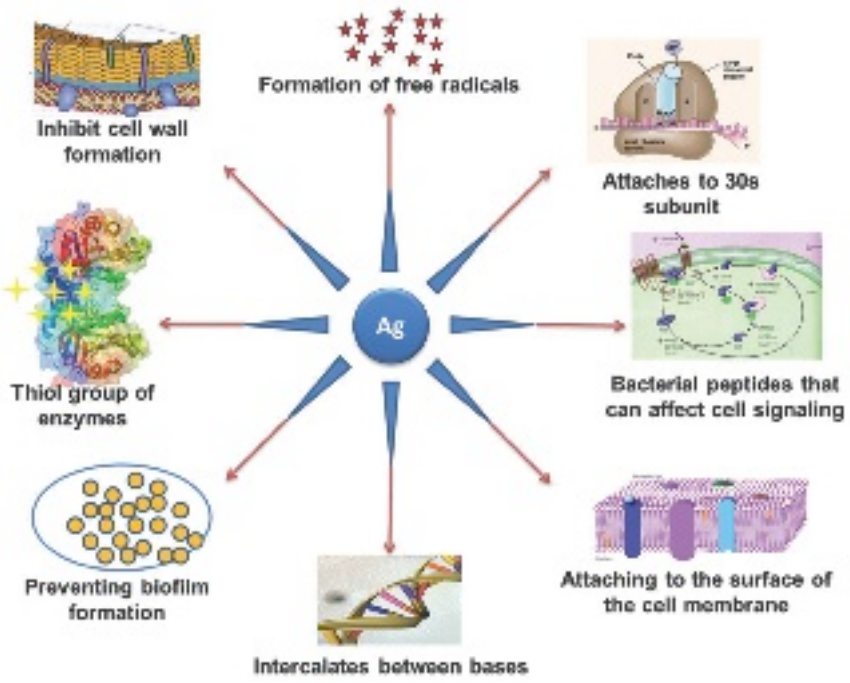

Figure 4. Antimicrobial mechanisms of action of silver. Reproduced from (*71*) with permission of The Royal Society of Chemistry.

The potential toxicity upon mammalian cells represents the major concern for the scientific community in the use of silver in medical dressings. Firstly, it should be claimed that silver becomes cytotoxic beyond threshold concentrations when internalized within cells. This can occur when silver is present in the surrounding milieu of mammalian cells and consequently it is able to penetrate the cell membrane as well. A recent study proved that the exposure of eukaryotic cells to AgNPs led to oxidative stress by inducing the production of ROS, the up-regulation of HO-1 expression, apoptosis and autophagy.(*72*) Furthermore, the cytotoxicity of metal was found to be dose-dependent. ROS are able to interact with DNA thus causing the damage of double helix, the modification of nucleobases and the formation of coupling phenomena.(*73*) Silver even proved to enter

into the nuclei of cells (by diffusive phenomena or through nuclear pores) thereby inducing protein aggregation and block of transcription, replication and cellular proliferation.(*74*) Given these premises, it is noteworthy consider to entrap silver ions or AgNPs in tridimensional matrices thus avoiding, or at least limiting, from being available to the eukaryotic cell uptake but preserving its antibacterial properties at the same time. For instance, the ability of a 1-deoxylactit-1-yl chitosan, (shortly named chitlac) in combination with other polysaccharides is reported for the *in situ* preparation of stable suspensions of evenly sized AgNPs,(*62*) allowing to obtain an antimicrobial and biocompatible system for various biomedical applications.(*75*),(*76*),(*77*)

1.7. Inflammation treatment

As described above, persistent inflammatory response at lesion site represents one of the main critical aspects for the correct recovery of chronic wounds. For instance, the activation of neutrophils and other neutrophilic polymorphonuclear leukocytes (PMN) recruited to the inflamed site leads to the release of ROS and other pro-inflammatory mediators which, on one end, contribute to the PMN antimicrobial activity and, on the other, are involved in the pathogenesis of tissue damage. It is therefore plausible that, in the attempt to mask the negative side of inflammation, an increasing number of studies are continuously performed worldwide with the aim of finding drugs that can eliminate, or at least dampen, inflammation-derived tissue injury.

The review paper of Karukonda *et al.*(*78*) discusses the principal anti-inflammatory drugs employed for the wound healing (Table 1).

Drug	Mechanism of action	Wound healing positive effects	Wound healing negative effects
Corticosteroids	Inhibition of gene expression	Dampening of immune-mediate damage	Worsening of infections Decreased of inflammatory mediators, platelet adhesion and phagocytosis Decreased synthesis of collagen due to reduced protein synthesis Decreased tissue remodelling
Colchicine	Inhibition of microtubule formation	Improvement in the early inflammatory phase	Decreased granulocytes migration and cytokine release Decreased fibroblast synthetic activity Increased collagenolysis
Dapsone	Inhibition of PMN integrins	Limitation of PMN-mediated damage and inflammation	Not active towards macrophages and lymphocytes
Ibuprofen	Inhibition of cyclooxygenase	Limitation of inflammation	Reduction of the tensile strength of wound
Aspirin	Inhibition of arachidonic and metabolites	Limitation of inflammation	Impairing of hemostatic phase by inhibiting platelet aggregation

Table 1. Anti-inflammatory drugs employed in wound healing. Adapted from (*78*).

Table 1 points out that common drugs can provide both benefits and drawbacks for the correct wound healing. This situation might dramatically worsen when chronic lesions are considered (compared to acute ones) and drugs are administered improperly. Besides to the mechanism of action, other points having to take into account as dosage and route of administration with respect to specific phases of wound healing. For instance, while oral doses of the corticosteroid prednisone (above 10 mg per day) negatively influence wound healing in the first three days, higher dosage (at or above 40 mg per day) is requested afterwards to favor collagen remodeling. However, administration of corticosteroid inhibits wound closure regardless of the inflammation phases.(*78*) As mentioned above, the route of administration is also important to the final outcome. As an example, topical

hydrocortisone shows poor benefits for wound healing, in any case lower if compared to other corticosteroids administered orally.

To date, several studies claimed the possibility to employ "natural drugs" derived from both plants and animals to face chronic wounds. A recent review paper screened hundreds of studies where combined herbal preparations and their phytochemical constituents have been used for wound management.(*79*) For example, single herbal preparations of *Achillea millefolium* proved to decrease inflammation and showed angiogenic, debridement, granulation and antimicrobial functions. Gels of *Aloe vera* demonstrated wound healing potential by anti-inflammatory effects and increasing re-epithelialization and microcirculation. Moreover, the production of pro-inflammatory cytokines TNF-α, IL-6 and leukocyte adhesion have been found to diminish in a rat model of burn wound treated with such gels. Combined herbal preparations as *Ampucare* (a topical oil-based preparation containing *Azadirachta indica*, *Berberis aristata*, *Curcuma longa*, *Glycyrrhiza glabra*, *Jasminum officinale*, *Pongamia pinnata*, *Rubia cordifolia*, *Terminalia chebula*, *Trichosanthes dioica*, *Symplocos racemosa*, *Ichnocarpus frutescens*, *Capsicum abbreviata*, *Nymphaea lotus*) showed burn healing effect with enhancement of antioxidant function, NO levels, as well as increase in protein level and vitamin C in rats.(*79*)

Another review paper collected several works dealing with the possibility to use honey as anti-inflammatory agent.(*80*) Honey proved potent multiple anti-inflammatory effects. For instance, the reduction of inflammation was observed in the clinic following the application of honey as well as supported by histological evidences. Clinically, numerous observations reported that honey is able to reduce edema and exudates. The anti-inflammatory effect of honey may be explained by several mechanisms of action as inhibition of the complement pathway, of ROS production, of leukocyte infiltration and of COX-2 and inducible NO synthase expression. Lastly, the inhibition of matrix metalloproteinase 9 (MMP-9) is considered a further anti-inflammatory mechanism of honey action. While honey components (including phenolic compounds and flavonoids) responsible for the anti-inflammatory activity *in vitro* have been partially identified, it is not completely obvious whether such components elicit anti-inflammatory activities *in vivo*.(*80*) Many other natural products as yoghurt, tea tree oil and potato peeling have been used to face chronic wounds but controlled studies are lacking.

1.8. Butyrate

Among natural drugs, butyrate represents one the most studied as anti-inflammatory molecule. Butyrate belongs to the short chain fatty acids (SCFAs) family, together with propionate and acetate. Butyrate is physiologically present in the healthy intestine of human body and together with propionate and acetate is the major metabolic products of the anaerobic fermentation of indigestible dietary fibers carried out by microbiota colonizing the large intestine. More in detail, such molecule is produced by some *Firmicutes* using either the Butyryl-CoA:acetate CoA-transferase enzyme or, less commonly, the phosphotransbutyrylase and the butyrate kinase.(*81*) The former pathway is the one exploited by most of the healthy gut microbiota. The concentration of acetate, propionate and butyrate was found to be around 50-150 mM in the colon with a ratio of 3:1:1. Immediately after its production, butyrate is quickly absorbed by epithelial cells at lumen level and used as an energy source. This implies that the concentration in the systemic circulation is very low.

Besides being the preferred energy source for the cells that lines the colon, SCFAs have been shown to possess interestingly biological properties, including anti-inflammatory and anti-tumorigenic activities.(*82*),(*83*) The role of SCFAs exerted in modulating the inflammatory response is mainly related to their effects on endothelial cells and leukocyte pathophysiology. In this respect, most of the studies deal with the capability of butyrate to influence several functional responses of PMN that play a crucial role during the early inflammatory phase. It has been reported, for instance, that butyrate influences PMN adhesion, chemotaxis, degranulation, phagocytosis, microbial killing and release of pro-inflammatory mediators.(*84*),(*85*),(*86*)(*87*) Concerning the production or ROS, the effect of SCFAs on PMN respiratory burst remains under debate. Indeed, either stimulatory(*88*) or inhibitory(*89*) activities have been reported where ROS release was assessed almost exclusively from PMN maintained in suspension, a situation that is closer to the condition of circulating leukocytes than of granulocytes in inflamed tissues. The anti-inflammatory properties of butyrate derives from the interaction *via* GPR41 and GPR43 receptors (G-coupled protein)(*82*) expressed on PMN and on the cells of the mucosa. Moreover, butyrate plays also the role of histone deacetylase (HDAC) inhibitor in colonocytes and in cells of the immune system so promoting hyperacetylation.(*90*)

In spite of this, the activity of butyrate results transient because of many factors and many authors have already investigated this aspect.(*91*),(*92*),(*93*) Given these premises, the need

to develop smart systems able to provide the right amount of butyrate over time to the cells should be a promising strategy to face chronic inflammation at wound site.

1.9. Wound dressings

Historically, the main role of wound dressings was to contribute palely in the healing cascade by assuming only protective functions. Nevertheless, so far it is common opinion to consider wound dressings as dynamic systems positively enhancing the recovery of lesions. Overall, wounds may be treated by either passive or active dressings.(*94*) The former are generally employed in the treatment of acute wounds, ensuring high absorption of exudates and adequate protection, whereas the latter are commonly used in chronic lesions considering their ability to adapt to wounds and to guarantee a moist environment so as to enhance the recovery.(*95*) An important parameter to take into account in the wound dressing production is the environment that characterizes chronic wounds: indeed, the moist milieu is a paramount factor favoring the proliferation and migration of fibroblasts and keratinocytes, the collagen synthesis thereby leading to reduced scar formation.(*96*) At the same time, moist dressings are considered to aid lesion healing faster compared to dried ones.(*97*) Other features that wound dressings have to ensure are to provide thermal insulation, gaseous exchange and to help drainage and debris removal; they should not be cytotoxic or elicit any allergic or immune response; they should possess antimicrobial properties thereby facing primary infections and protecting from secondary ones; finally, ideal wound dressings should be easily removed without damaging healthy tissues.(*98*) Generally, wound dressings may be categorized as hydrocolloids, hydrogels, foams and films/membranes.

1.9.1. Hydrocolloids

Hydrocolloids concern moist wound dressing made of a support material and a layer with colloidal particles containing biocompatible either protein (collagen, gelatin) or polysaccharide (cellulose) gels.(*97*) These dressings swell when in contact with exudates because of absorption of wound fluids so as to create a moist environment. Nevertheless, potential use of hydrocolloids in the treatment of non-healing wounds is contradictory: the excessive moist environment may generate hypoxic conditions thus favoring the autolysis of necrotic tissue and increasing the risk of infection by pathogens.

1.9.2. Hydrogels

From a structural point of view, hydrogels are composed by a single or mixed hydrated polymers where at least the 20% of total weight is water.(*99*) When the total content of water reaches more than 95% of the total weight these constructs may be classified as superabsorbents. Hydrogels are simply fabricated by covalent or ionic gelation by means of small molecules named cross-linkers. Usually, covalent cross-linkers allow the formation of hydrogels with a permanent network structure, since irreversible chemical links are formed. This system enables absorption of water and/or bioactive compounds without disgregation and permits drug release by diffusion. On the other hand, ionic cross-linkers are generally considered more biocompatible towards mammalians and they allow the fabrication of less stable networks formed by reversible links. For instance, ionically cross-linked chitosan hydrogels exhibit a higher swelling behavior to pH changes with respect to covalently ones.(*100*) To conclude, the type of gelation strongly influences the physical-chemical behavior of such systems. Similarly to hydrocolloids, hydrogels foster the autolytic debridement of necrotic tissues and are chiefly more efficient to dry wounds with few exudates. On the other hand, if applied in lesions with higher content of wound fluids, they may foster maceration phenomena. The main advantage in the use of hydrogels as wound dressing resides in their easy usage without impairing with the physiological healing.(*45*)

1.9.3. Foams

Such constructs were fabricated as alternatives to hydrocolloids for draining lesions with higher content of wound fluids. The ability of foams to absorb exudates depends on which polymer has been employed for the fabrication and by the thickness or resulting material.(*45*) Foams are easy to manipulate by adapting to different lesions, highly absorbent, protective and comfortable.

1.9.4. Films/membranes

These wound dressings range from micrometers to millimeters in thickness and are fabricated by different techniques by using one or more polymers. These constructs are usually durable, comfortable, easy to manipulate, adhesive, cheap, semi-permeable to oxygen and water vapor and often impermeable to liquid and to bacterial contamination.(*45*) On the other hand, the main drawback for such systems is that they should be employed only in the case of low amount of exudates lesions and in applications

that last up to five days in superficial wounds. However, films might be used in association with other dressings thereby improving their absorption properties. In any case, drugs, growth factors or silver may be embedded within active polymeric dressing in order to improve the healing process.

1.10. Natural and synthetic polymers for wound healing

Several polymers with peculiar chemical, physical and biological properties are currently used for the fabrication of wound dressings with different shape, morphology and dimensions.(*101*) Based on their origin, polymers may be easily classified as natural or synthetic. Engineered polymers as well as mixtures of two or more ones can even considered as further types. Table 2 summarizes the majority of polymers employed in the treatment of non-healing wounds as active constructs.

Polymer	Type	System	Embedded substances
Protein	Collagen - gelatin	Gelatin microsphere (*102*)	bFGF
		Collagen matrix (*103*)	Glucose oxidase
		Collagen-gelatin foam (*104*)	bFGF
	Fibrin	Scaffold (*105*)	AdeNOS
		Gel (*106*)	$CD34^+$ cells
	Silk fibroin	Film (*107*)	*Aloe vera* extract
	Elastin	Peptides gel (*108*)	KGF
Polysaccharide	Chitosan	Chitosan-crosslinked collagen (*109*)	Recombinant human aFGF
	Hyaluronan and derivatives	Benzyl esters films (*110*)	Autologous human keratinocytes
		High molecular weight (*111*)	Iodine complex
		Foam (*112*)	Arginine and EGF
		Gel (*113*)	Amino acids
	Cellulose and derivatives	Dressing (*114*)	Silver nanoparticles
		Carboxymethyl cellulose hydrogel (*115*)	Chestnut honey
	Alginate	Hydrogel (*116*)	Phenytoin
Synthetic	PVA	Aminophenyl boronic acid with PVA (*117*)	Ciprofloxacin
	PEG	PEG-PCL nanofibers (*118*)	EGF / bFGF
	PVP	PVMMA and PVP (*119*)	NO
	Poly(α-esters)	PLGA microspheres (*120*)	rhEGF
		PCL nanofibers (*121*)	Curcumin
		PLA fibers (*122*)	bFGF

Table 2. Polymers employed in the treatment of non-healing wounds as active materials. Adapted from (*123*).

Among them, natural polymers are used in regenerative medicine field, and consequently in skin regeneration, because of their lack of toxicity, biodegradability and the capacity to resemble the extracellular matrix.(*124*) Natural polymers can even easily engineered or

surface modified in order to improve their physical, chemical and biological features. The use of such materials is favored with respect to synthetic ones, because of the lack of cell recognition signals. However, some concerns may be cited for natural polymer as their low mechanical properties and the inability to finely control the degradability *in vivo*. To date, natural polymers can be obtained by fermentation of microorganisms or produced *in vitro* by enzymatic processes. In spite of this, the largest amount is still extracted from plants, animals or algae. Below are described natural polymers employed during the experimental activity carried out during the PhD experimental activity.

1.10.1. Chitosan

Chitosans are considered as a family of polysaccharides made of linear binary copolymers of β-(1→4)-linked D-glucosamine (D unit) and *N*-acetyl-D-glucosamine (A unit) as pointed out in Figure 5.

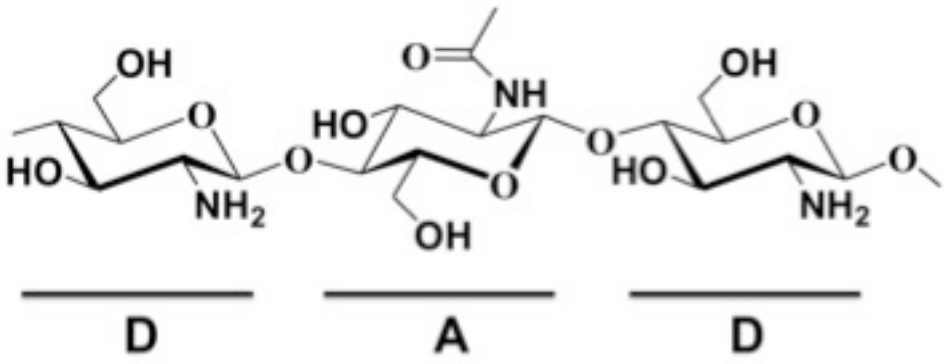

Figure 5. Structure of chitosan.

From a chemical point of view, chitosans show a different distribution of A and D units, where the latter are generally higher in number and the former are random distributed in the polymer backbone. Chitosans stem from chitin, one of the most abundant polysaccharides on the earth, from the exoskeletons of arthropods, or from certain fungi and it is possible to prepare chitosans with different fractions of A units (Fa) by means of either deacetylation of chitin (under acidic or alkaline conditions) or reacetylation of highly deacetylated chitosans.(*125*) While acidic conditions cause drastic degradation rates of polysaccharide, alkaline ones are well tolerated by acetomido groups of chitin. Indeed, only limited degradation occurs during drastic alkaline conditions.(*125*) As soon as deacetylation (or reacetylation) reaction ends, Fa can be easily determined by means of

different techniques as IR, UV, gel permeation chromatography, colloid titration, elemental analysis, dye adsorption and acid-base titration,(*126*) although ^{1}H-NMR may be assumed the "golden standard" method for such purpose.(*127*) Chitosans are also considered the water-soluble form of chitin containing from ~ 100 to ~ 40% of D units: a typical assumption to discriminate them is their solubility in 0.1 M acetic acid where chitosans are soluble whilst chitin is not.(*126*) Chitosans behave as amphiphilic polymers in solutions because of the hydrophobic nature of *N*-acetylated aminogroups and the hydrophilic character of D-units aminogroups to take up a proton and become positively charged.

Chitosans, as well as other polysaccharides, are polydispersed with respect to molecular weight. The molecular mass is therefore an average of the whole distribution of molecular masses. The most commonly used are the number M_n, which weights the polymer molecules according to the number of molecules having a specific molecular weight, and the weight-average (M_w), which weights the polymer molecules according to the weight of molecules having a specific molecular weight. They are defined as:

$$\overline{M}_n = \frac{\sum_i n_i M_i}{\sum_i n_i}$$

$$\overline{M}_w = \frac{\sum_i n_i M_i^2}{\sum_i n_i M_i}$$

where n_i is the number of molecules and M_i is the molecular weight. A useful parameter is the polydispersity index (PI), defined as the ratio between $\overline{M}_w$ and $\overline{M}_n$ that indicates how the polymer distribution is polydispersed with respect to molecular weight. A PI = 1 refers to a monodispersed sample whereas a PI less than 2 refers to a heterogeneous population of molecular weights. PI > 2 indicated a very broad distribution, suggesting either a mixing of polymer with different molecular weights or a non-random degradation occurred during the production process.(*125*)

Commercial chitosans generally show Fa values spanning from 0 and ~ 0.2 and are characterized to be soluble only in aqueous solutions in acidic conditions whereas are considered insoluble for neutral or basic pH values.(*128*) All chitosans are in fact soluble at pH values below 6 and the solubility tends to decrease by increasing pH. Beyond such pH value commercial chitosans begin to precipitate. Other effects may contribute to the solubility of chitosans as well as the ionic strength (due to salting-out effects), the

molecular weight and the presence of ions (*i.e.* copper) in the solvent. However, soluble chitosans for neutral pH values can be fabricated by modulating the Fa. For instance, Sannan *et al.* obtained fully soluble polymers with Fa values ranging from 0.4 to 0.6.(*129*) Similarly, Vårum *et al.* demonstrated that the solubility of hydrochloride chitosans increases with increasing Fa.(*128*) About charge density, it depends by the degree of protonization (determined in turn by chemical composition, *i.e* Fa) and should be vary by tuning the molecular weight of polymers, the pH and the ionic strength.(*125*) Overall, different chitosans have shown similar values of the dissociation constant (pKa) ranging from 6.2 to 7 depending even on experimental conditions used.(*130*),(*131*),(*132*),(*133*)

Many chitosan-based matrices reported in the literature and proposed for biomedical applications, are fabricated by three-dimensional hydrogels starting from chitosan solutions where the use of specific cross-linkers to form covalent or ionic bonds is a mandatory step.(*134*),(*135*),(*136*),(*137*) In addition, chitosan may form hydrogels without any cross-linker only by changing the pH or using hydroalcoholic media.(*138*),(*139*) Chitosan hydrogels can be further processed by employing several technologies (*i.e.* freeze-drying and air drying) in order to obtain matrices as well as scaffolds and membranes.(*140*) The properties of cross-linked hydrogels depend mainly on their cross-linking density, that is, the ratio of moles of cross-linker to moles of polymer repeating units. Moreover, a critical number of cross-links per chain are required to allow the formation of a uniform polymeric network throughout the hydrogel defined as a "wall-to-wall" system. The most common cross-linkers used to promote a covalent reticulation of chitosan are dialdehydes such as glyoxal and glutaraldehyde.(*141*),(*142*) The use of genipin represents an alternative solution.(*143*) Nevertheless, most of the cross-linkers used to perform covalent cross-linking are toxic and then incompatible with the biological environment. In order to overcome this drawback, ionic cross-linkers can be exploited because of their higher biocompatibility and milder conditions of use. The typical ionic cross-linker for chitosans is tripolyphosphate (TPP), which is an ionic cross-linker already used to reticulate chitosan to obtain fibers, nanoparticles, and micro/nano-gels.(*144*),(*145*)

About wound healing properties, chitosan was found favoring wound recovery by stimulating the proliferation of cells and deposition of organized connective tissue. This behavior was ascribed to the ability of chitosan to elicit macrophages to release TGF-β and PDGF cytokines.(*146*) Furthermore, another study claimed that chitosan may boost the biological activity of growth factors present in serum by interacting with them.(*147*) Last but not the least, chitosan is well known to possess antibacterial properties (mainly

bacteriostatic activity), a pivotal feature for an ideal wound dressing, because of its electrostatic, hydrophobic and chelating effects.(*148*)

Different formulations based on chitosan were obtained in the past for the treatment of non-healing wounds: mesh membranes,(*149*) films endowed with nanosilver,(*150*) films/gels containing fucoidan as a wound dressing for dermal burn healing,(*151*) membranes containing *Aloe vera*,(*152*) ciprofloxacin-loaded chitosan-gelatin composite films,(*153*) chitosan-fibrin-alginate composites(*154*) and microporous chitosan hydrogel-nanofibrin composite bandages.(*155*)

1.10.2. Hyaluronic acid

Hyaluronic acid, or hyaluronan in its dissociated form, is a linear polysaccharide composed of alternating (1→4)-β linked D-glucuronic acid and (1→3)-β linked *N*-acetyl-D-glucosamine dimers (Figure 6) and belongs to a group of macromolecules known as glycosaminoglycans (GAG).

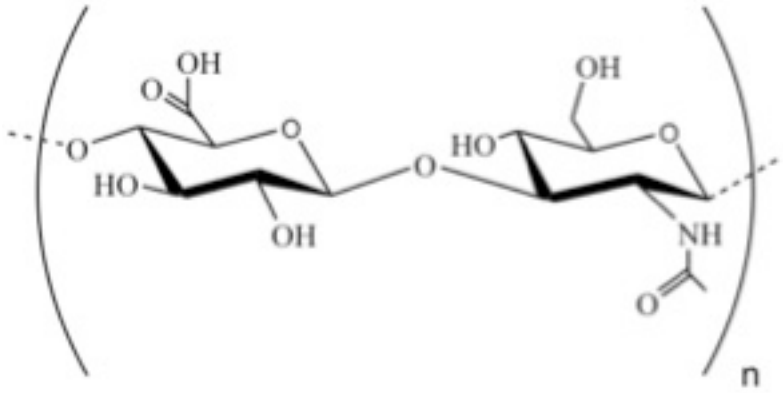

Figure 6. Structure of hyaluronic acid.

It is the most structurally simple one and it is not covalently associated to proteins, not synthesized in the Golgi apparatus and not sulphonated.(*156*) Hyaluronic acid is physiologically present in human body, for instance in the synovial fluid where it is at both high concentration and molecular weight in order to provide lubrication for the joints, by reducing the friction, and to serve as a shock absorber. It is a fundamental component of the extracellular matrix but it can be also found in the capsules of some bacteria. Such polysaccharide plays even a pivotal role in embryogenesis, signal transduction and cell motility.(*156*) Hyaluronic acid is an active biopolymer interacting with cells *via* CD44,

RHAMM and LYVE-1 receptors.(*157*) Generally, this polysaccharide shows high molecular weights but in some cases, as well as inflammatory pathologies, it can be degraded by the activity of radicals thereby forming low molecular weight fragments, which can accumulate during tissue injury. Due to its high biocompatibility, this polysaccharide is often employed in the biomedical field and it has used in several clinical applications as viscosurgery, viscoaugmentation, viscoseparation, viscosupplementation and viscoprotetion.(*158*)

Hyaluronic acid has been extensively studied for the treatment of non-healing wounds. For instance, silver sulfadiazine-impregnated polyurethane foams were developed and used as wound dressing: the lesion size was found to decrease around 77% without any inflammatory response in a rat skin experimental model after one week of foam application.(*159*) Biomimetic hydrogels for wound healing applications containing hyaluronic acid were functionalized with thiol cross-linking sites,(*160*) or cross-linked with DNA.(*161*)

2. AIMS

The main objectives for this thesis deal with the fabrication and characterization of innovative polysaccharide-based biomaterials in the form of membranes, gels and nanostructures, to be used as potential tools for the treatment of non-healing wounds.

The specific aims were:

- Establish a method to develop tridimensional matrices in the form of hydrogels and dried membranes using the biopolymer chitosan and tripolyphosphate (TPP) as ionic cross-linker.
- Provide further insights with respect to literature on the ionotropic gelation of chitosan with either TPP or pyrophosphate (PPi) as cross-linkers in dilute solutions and in tridimensional hydrogels.
- Enhance the antimicrobial properties of the chitosan membranes by using colloidal suspensions of chitlac-AgNPs without affecting the viability of mammalian cells.
- Study the anti-inflammatory properties of the short chain fatty acid butyrate as potential molecule to load within chitosan membranes.
- Fabricate and characterize chitosan/hyaluronan nanoparticles (complexes) able to host butyrate and to control its leakage.
- Evaluate biological properties of a silver hyaluronan-lipoate derivative in gel state.

3. EXPERIMENTAL SECTION

CHAPTER I

Fabrication of chitosan-TPP hydrogels and membranes

3.1.1. Aim of work

In this section is presented the work aiming at (*i*) developing a slow diffusion-based technique to prepare homogeneous bulk chitosan-TPP hydrogels, (*ii*) investigating their physical-chemical and mechanical properties, (*iii*) preparing prototypes of membranes for biomedical applications by a freeze-drying technology and (*iv*) evaluating the biocompatibility of the resulting membranes on eukaryotic cells.

3.1.2. Materials and methods

3.1.2.1. Materials. Highly deacetylated chitosan (fraction of *N*-acetyl-glucosamine units - Fa - of 0.16 as determined by means of ^{1}H-NMR), was purchased from Sigma-Aldrich (Chemical Co. USA) and purified by precipitation with isopropanol, followed by a dialysis against deionized water.(*162*) The relative molar mass ("molecular weight", M_w) of chitosan determined by intrinsic viscosity measurements was found to be around 690 kDa.(*162*) Other chitosans used in this study were kindly gifted by Prof. Kjell Morten Vårum (NTNU, Trondheim, Norway) and their features are shown in Table 4. Pentasodium tripolyphosphate (TPP) (MW 367.86 g mol^{-1}; technical grade 85% wt), sodium chloride (NaCl), glycerol (*ReagentPlus*® ≥ 99.0%) and Phosphate Buffered Saline PBS (0.01 M phosphate buffer, 0.0027 M KCl and 0.137 M NaCl) were purchased from Sigma-Aldrich (Chemical Co. USA). Ammonium vanadate and ammonium molybdate were purchased from Honeywell Specialty Chemicals Seelze GmbH (Germany) and Carlo Erba (Italy), respectively. LDH (lactate dehydrogenase)-based TOX-7 kit was purchased from Sigma Aldrich (Chemical Co. USA). All other chemicals and reagents were of the highest purity grade commercially available.

3.1.2.2. Chitosan-TPP hydrogel preparation. Chitosan-TPP hydrogels were fabricated

by exploiting an ion diffusion technique (Figure 7). Chitosan solution (3.5% w/v) was prepared as a stock solution by dissolving chitosan (0.35 g) in 10 mL of 0.2 M acetic acid solution and diluted to reach the desired concentration. Glycerol (5% v/v) was used as plasticizer. Chitosan solutions were casted in a mold (diameter = 22 mm, height = 2.5 mm) closed by two dialysis membranes (average flat width 33 mm, Sigma Aldrich, Chemical Co.) and fixed by double circular stainless iron rings. The system was hermetically sealed and immersed into a TPP-NaCl-glycerol solution (gelling bath). The concentrations of both TPP and NaCl in the gelling bath have been varied over the range 1-3% w/v and 0-500 mM, respectively, in order to obtain a broad range of formulations. Conversely, glycerol was kept constant both for the inner chitosan solution and the outer TPP-NaCl solution for all experiments. Ion diffusion proceeded for 24 h under moderate stirring at room temperature.

3.1.2.3. Membrane preparation. Resulting hydrogels were washed twice at the end of dialysis (1 h for each washing) with 150 mM NaCl solution first and finally with deionized water in order to remove all residual traces of unbound tripolyphosphate. Hydrogels were thereafter cooled by immersion in a liquid cryostat (circulating bath 28L, VWR, Radnor, PA, USA). Ethylene Glycol in water (3:1) was used as refrigerant fluid. Temperature was decreased from 20 to -20 °C by 5 °C steps with 20 minutes intervals. Samples were then freeze-dried for 24 h.

3.1.2.4. Morphological analyses. Morphological analyses of hydrogels and membranes were performed by Scanning Electron Microscopy (Quanta250 SEM, FEI, Oregon, USA). In environmental conditions, hydrated specimens were mounted on aluminium stubs covered with double-sided conductive carbon adhesive tape. In the case of cross-section evaluation, samples were cut in parallel to the cylinder axis and then prepared as described above. The samples were then analysed in secondary electron detection mode. The working distance was adjusted in order to obtain the suitable magnification. Freeze-dried membranes were sectioned and directly visualized after sputter-coating with an ultrathin layer of gold and analysed as to both material surface and cross sections. The accelerating voltage was varied from 20 to 30 kV.

3.1.2.5. Mechanical spectroscopy. Rheological characterization of cylindrical chitosan hydrogels was performed by means of a controlled stress rheometer Haake Rheo-Stress

RS150 operating at 25 °C using, as measuring device, a shagreened plate apparatus (HPP20 profiliert: diameter = 20 mm). To avoid water evaporation from the hydrogel, the measurements were led in a water-saturated environment formed by using a glass bell (solvent trap) containing a wet cloth. In addition, to prevent both wall-slippage(*163*) and excessive gel squeezing (which could reflect in the alteration of polymeric network properties), the gap between plates was adjusted, for each sample, by executing a series of short stress sweep tests (f = 1 Hz; stress range 1 - 5 Pa; maximum deformation < 0.1%) characterized by a reducing gap.(*164*) The selected gap was that maximizing the value of the elastic modulus G' (used gaps ranged between 2.5 and 2.0 mm). For each hydrogel, the linear viscoelastic range was determined by means of a stress sweep test consisting in measuring elastic (G') and viscous (G") moduli variation with increasing shear stress (1 Pa < τ < 10^3 Pa) at a frequency ν = 1 Hz (hence with $\omega = 2\pi\nu$ = 6.28 rad s^{-1}). Mechanical spectrum of the hydrogel was determined by measuring the dependence of the elastic (G') and viscous (G") moduli from the pulsation ω at constant shear stress τ = 3 Pa (well within the linear viscoelastic range which, for all samples, spans up to at least 30 Pa).

3.1.2.6. Uniaxial compression. Compressive properties of hydrogels were evaluated with a universal testing machine (Mecmesin Multitest 2.5-i) equipped with a 100 N load cell in controlled conditions (T = 25 °C, relative humidity = 50%). A compression speed of 6 mm min^{-1} was used. Toughness was calculated by measuring the area under the stress-strain curve at 70% of strain. All measurements were performed in triplicate. An unpaired Student's t-test was used to determine statistically significant differences for the toughness calculation.

3.1.2.7. Attenuated total reflectance fourier transform infrared spectroscopy (FTIR-ATR). Fourier transform infrared spectra of chitosan, membranes and TPP powder were obtained using Spectrometer Nicolet 6700 (Thermo Electron Corporation, Madison WI, USA) with DTGS KBr detector. The following setup was used throughout the measurements: number of sample scans 16, resolution 6 cm^{-1} from 500 to 2 000 cm^{-1}.

3.1.2.8. ^{31}P-Nuclear Magnetic Resonance (^{31}P-NMR). All ^{31}P-NMR spectra were recorded, at 25 °C, on a JEOL Eclipse 400 (9.4 T) NMR spectrometer operating at 399.78 MHz for ^{1}H and 161.83 MHz for ^{31}P. 512 scans were accumulated with a spectral width of 5.66 kHz over 8192 complex data points. The employed pulse width was 45° and the total

recycle time 2.5 s. The data were multiplied by a decaying exponential function (broadening factor 0.5 Hz) and zero filled twice prior to Fourier transform (FT). A coaxial insert filled with a solution of Triphenylphosphine (PPh_3) in $CDCl_3$ containing Tetramethylsilane (TMS), was employed for lock and reference purposes. The ^{31}P chemical shifts are referred to H_3PO_4 85%, considering it resonating at 40.5 (Ξ) at a field at which TMS protons resonate at exactly 100 MHz.(*165*),(*166*) Chitosan (3.6 g L^{-1}) and TPP (0.3% w/v) solutions in 0.2 M acetic acid-150 mM NaCl were used to record NMR spectra. Moreover, NMR analyses were performed to assess the amount of TPP and other phosphates diffusing into chitosan solution during the dialysis. The gelling bath used in hydrogel preparation was collected at different time intervals (t = 0, 2, 4, 6, 8, 24 h) and subsequently analyzed. The decrease of the signals corresponding to phosphates was determined by normalizing the integrals with respect to the reference PPh_3.

3.1.2.9. Phosphate quantification. The amount of TPP present in the hydrogels was quantified by means of a protocol described elsewhere with slight modification.(*144*) Briefly, standard (TPP) or hydrogels were dissolved in hydrochloric acid 37% (Sigma Aldrich, Chemical Co. USA) at room temperature. 0.1 mL of the latter solution was added to 0.9 mL of deionized water. Finally, 0.2 mL of a solution containing ammonium molybdate (2.5% w/v) and ammonium vanadate (0.125% w/v) were added and mixed by shaking. After five minutes, the absorbance of the yellowish solution was measured at 420 nm using Infinite M200 PRO NanoQuant, Tecan spectrophotometer. A blank solution was prepared with 1 mL of deionized water and 0.2 mL of the vanadium-molybdenum solution. A standard calibration curve for TPP was obtained with $R^2 > 0.99$. All measurements were performed in triplicate.

3.1.2.10. Swelling studies. Swelling studies of hydrogels were carried out in PBS at room temperature. Samples disks (diameter = 22 mm, surface/volume ratio 4 cm^{-1}) were placed in 10 mL of PBS under moderate stirring. After blotting the excess of water using filter paper, the hydrogels were weighed at different time intervals (t = 0, 1, 2, 3, 4, 5, 6, 7 and 24 h). The swelling ratio was calculated as the percentage of water loss with respect to the initial weight in agreement with the formula

$$Hydrogel\ deswelling\ (\%) = \frac{W_t - W_0}{W_0} \times 100$$

where W_t is the weight of samples at different time intervals and W_0 the dry weight of hydrogels at t = 0. All measurements were performed in triplicate.

3.1.2.11. Cell culture. Mouse fibroblast-like (NIH-3T3) cell line (ATCC® CRL-1658™) was used for the *in vitro* experiments. Cells were cultured in Dulbecco's Modified Eagle's Medium high glucose (EuroClone, Italy), 10% heat-inactivated fetal bovine serum (Sigma Aldrich, Chemical Co. USA), 100 U mL^{-1} penicillin, 100 µg mL^{-1} streptomycin and 2 mM L-glutamine in a humidified atmosphere of 5% CO_2 at 37 °C.

3.1.2.12. Lactate dehydrogenase (LDH) assay. *In vitro* cytotoxicity of membranes was evaluated by using the lactate dehydrogenase assay on NIH-3T3 cells. UV-sterilized freeze-dried samples (30 minutes of irradiation for each side of sample) of approximately 6 mm in length and 2 mm in width were placed in Dulbecco's modified Eagle's medium, inactivated fetal bovine serum 10%, penicillin 100 U mL^{-1}, streptomycin 100 µg mL^{-1} and L-glutamine 2 mM for 72 h at 37 °C and 5% pCO_2 (extraction medium). After 72 h of incubation, the cytotoxicity test was performed by direct contact of the cells with the swollen membranes and by using the extraction medium. In the case of the direct contact test, 25 000 cells were plated on 24-well plates and, after complete adhesion, culture medium was changed with 300 µL of fresh medium. Tested materials were directly deposited on the cell layer. After 24 and 72 h, medium was collected and the LDH assay was performed according to the manufacture's protocol. In the extraction test, extraction medium was added on cells seeded on 24-well plates (25 000 cells/well). The LDH assays were performed after 24 and 72 h as described above. As a positive control material, poly(urethane) films (PU) containing 0.25% zinc dibuthyldithiocarbamate (ZDBC) (6 mm disks) were used. As negative control material, plastic poly(styrene) sheets (PS) (6 mm disks) were used. Triton X-100 0.1% v/v was used as a positive control for extraction test. Each material test was performed in triplicate. Evaluation of cytotoxicity was calculated according to the formula

$$LDH\ released\ (\%) = \frac{A - B}{C - B} \times 100$$

with A: LDH activity in the culture medium of membrane-treated or extraction medium-

treated cells; *B*: LDH activity of culture medium from untreated cells and *C*: LDH activity after total cell lysis at 24 and 72 h.

3.1.3. Results and discussion

The present section describes the preparation of chitosan-based hydrogels and dried membranes using TPP as cross-linker. Typically, when TPP is added to diluted chitosan solutions, the anions quickly cross-link cationic chitosan chains leading to the formation of nanoparticles or aggregates.(*167*) In accordance with literature, we observed that when chitosan concentration was increased up to 3% and TPP added in solution, a very fast reticulation took place causing the formation of polydisperse micro-aggregates. This leads to a highly inhomogeneous system with an unreacted liquid core and a highly cross-linked surface. Using this experimental approach, it was not possible to obtain homogeneous macroscopic hydrogels with well define shape and regular structure. Therefore, it was necessary to control the reaction rate and the cross-linking density to tune the properties of the polymeric network. To this end, an ion diffusion-based approach that enables TPP to diffuse slowly and gradually into the confined polymer solution from an external cross-linking bulk, aiming at a uniform reticulation throughout the chitosan matrix, was devised. The experimental setup is depicted in Figure 7.

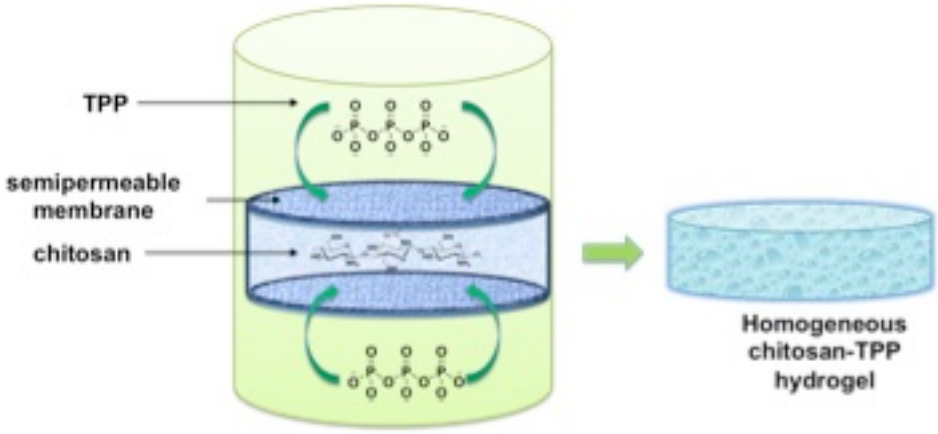

Figure 7. Experimental set up to develop chitosan-TPP hydrogels by exploiting dialysis technique. Enclosed viscous chitosan solution is placed into an outer TPP solution under stirring condition. During the dialysis TPP ions diffuse through semipermeable membranes and after 24 h the viscous solution has turned into a homogeneous hydrogel by ionotropic gelation. Adapted with permission from (*168*). Copyright 2014, American Chemical Society.

First attempts with a chitosan (Fa 0.16, M_w 690 kDa) concentration of 1.5% w/v led to the formation of systems characterized by highly reticulated surfaces and liquid cores. This can be traced back to the fact that when the dialysis starts, TPP ions bind to chitosan charge groups at the boundary of the polymer-gelling bath, and polymer chain diffusion takes place towards the gelling zone causing the formation of a concentration gradient. Hence, chitosan progressively accumulates within the gelling zone, resulting into an inhomogeneous hydrogel with the highest concentration of polymer at the TPP-hydrogel interface. At higher chitosan concentrations, homogeneous hydrogels were obtained for different TPP concentrations explored. This phenomenon can be explained by taking into account the very high viscosity of the chitosan solution that hampered the diffusion of the polymer towards the gelling zone preventing the formation of the gradient. These experimental evidences are in line with what is known for alginate-Ca^{+2} systems.(*169*) The addition of non-gelling ions (*i.e.* Na^{+}) in the gelling bath is expected to slow down the gelation process by screening the strong electrostatic interactions between polymer and cross-linker. Huang *et al.* demonstrated that small amounts of NaCl affect the binding mechanism of chitosan and TPP by decreasing the fast kinetics of their self-assembly and by weakening the binding of TPP to the polysaccharide.(*170*) Along this line, NaCl was added at two different concentrations (150 and 500 mM) into the gelling bath containing TPP. The presence of NaCl enabled to improve the homogeneity of the hydrogel for both NaCl concentrations. The outcome in the case of NaCl 150 mM was the hydrogel shown in Figure 8, which appears as a homogenous wall-to-wall system, albeit not transparent. Environmental scanning electron microscopy (E-SEM) in the wet state revealed the presence of a uniform polymeric structure both on the hydrogel surface and in the inner core (Figure 8, B-C).

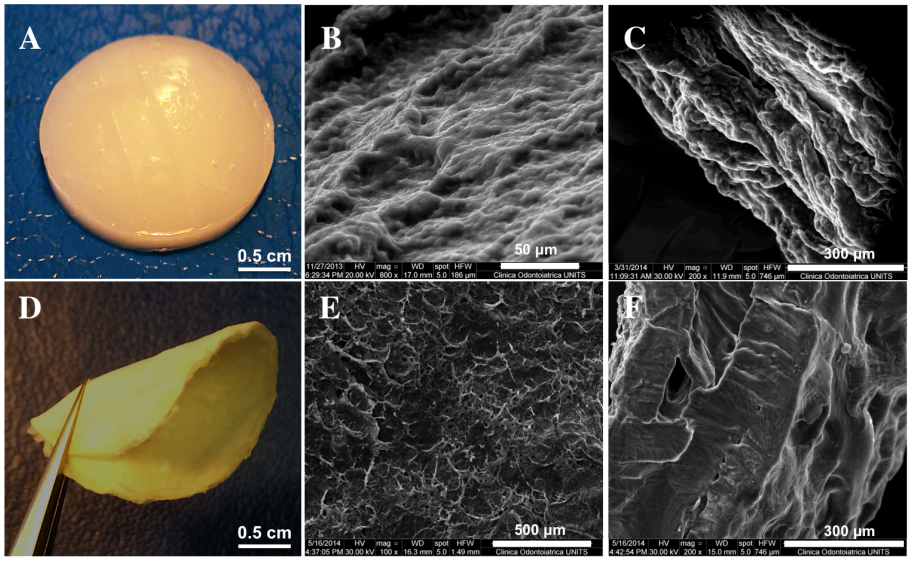

Figure 8. Chitosan-TPP hydrogels: (A) top view, (B) E-SEM micrograph of the hydrogel surface, (C) E-SEM micrograph of the hydrogel cross-section. Chitosan-TPP membrane derived from the hydrogel depicted in (A): (D) top view, (E) SEM micrograph of the membrane surface, (F) SEM micrograph of the membrane cross-section. Reprinted with permission from (*168*). Copyright 2014, American Chemical Society.

No evidences of irregular gelling zones were found even at high magnifications. Table 3 summarizes the overall conditions used to fabricate the hydrogels. A temperature-controlled freeze-drying procedure was applied to them to obtain soft pliable membranes as depicted in Figure 8. SEM images of the membrane (Figure 8, E-F) revealed a homogeneous polymeric mesh with a compact structure, which demonstrates the uniform reticulation occurred within the hydrogel phase.

	NaCl 0 mM			NaCl 150 mM			NaCl 500 mM		
	TPP 1%	TPP 1.5%	TPP 3%	TPP 1%	TPP 1.5%	TPP 3%	TPP 1%	TPP 1.5%	TPP 3%
Chitosan 1.5%	✖	✖	✖	▲	▲	▲	▲	▲	▲
Chitosan 2.5%	▲	▲	▲	▲	▲	▲	▲	▲	▲
Chitosan 3%	▲	▲	▲	▲	▲	▲	▲	▲	▲

Table 3. Experimental parameters investigated to fabricate chitosan-TPP hydrogels. ✖: Non-continuous networks (inhomogeneous); ▲: Continuous networks (homogeneous). Both chitosan and tripolyphosphate are expressed as % w/v. Chitosan with Fa 0.16 and M_w 690 kDa. Adapted with permission from (*168*). Copyright 2014, American Chemical Society.

The possibility to fabricate hydrogels with chitosans with different Fa and M_w was considered afterwards and the outcomes are pointed out in Table 4.

Chitosan (Fa)	$[\eta]$ mL g^{-1}	M_w (kDa)	Hydrogel formation
0.16	110	30	No
	660	210	Yes
	1026	340	Yes
0.46	340	100	No
	650	205	No
	920	300	No
0.63	300	88	No
	550	170	No
	950	310	No

Table 4. Experimental parameters investigated to fabricate chitosan-TPP hydrogels by means of hydrochloride chitosans with different acetylation degree (Fa) and molecular weight (M_w). Fa was determined by ^{1}H-NMR whereas M_w was determined by using intrinsic viscosity $[\eta]$ in agreement to the Mark-Houwink equation reported in Berth *et al.*(*171*) Chitosan, TPP and NaCl concentrations were 2.5% w/v, 1.5% w/v and 150 mM, respectively.

The formation of a continuous network (cylindrical hydrogel) was observed only for chitosan samples with Fa of 0.16 and M_w of 210 and 340 kDa. Chitosans with different acetylation degree were not able to favor the complete ionotropic gelation when dialyzed

against TPP. More in detail, chitosan solutions became opaque after 24 h of dialysis, thus indicating the formation of microgels (coacervates), without turning into a macroscopic hydrogel. These results indicate that the positive charges of chitosan play a pivotal role for the formation of the hydrogel: the higher is the Fa, the lower is the ability of chitosan to interact with TPP. However, chitosan with Fa of 0.16 and M_w of 30 kDa did not foster a complete gelation. In this case the role of molecular weight should be considered. Indeed, a macroscopic network was obtained with the same experimental conditions by increasing the M_w. In conclusion, macroscopic hydrogels are supposed being obtained only with chitosans with low Fa and medium/high M_w (≥ 210 kDa).

Mechanical characterization of hydrogels was carried out only on homogenous systems screened according to Table 3. Hydrogels are systems exhibiting viscoelastic behavior when undergoing deformation depending on the frequency of the deformation. In order to investigate mechanical properties of hydrogels, rheological and uniaxial compression studies were performed. In detail, rheological analyses were carried out by measuring the mechanical spectrum of hydrogels in oscillatory shear conditions. In all cases considered, the storage (G') modulus was about ten times higher than the loss modulus (G") and basically independent on the stress frequency, thus describing the systems under consideration as a strong gel. Mechanical spectrum of the samples was interpreted in terms of the generalized Maxwell model.(*172*) The storage and loss modulus can be modeled as function of oscillation frequency according to the following equations

$$G' = G_e + \sum_{i=1}^{n} G_i \frac{(\lambda_i \omega)^2}{1 + (\lambda_i \omega)^2} \; ; \; G_i = \frac{\eta_i}{\lambda_i} \quad (1)$$

$$G'' = \sum_{i=1}^{n} G_i \frac{\lambda_i \omega}{1 + (\lambda_i \omega)^2} \; ; \; G_i = \frac{\eta_i}{\lambda_i} \quad (2)$$

where n is the number of Maxwell elements considered, G_i, η_i, and λ_i represent the spring constant, the dashpot viscosity, and the relaxation time of the ith Maxwell element, respectively. G_e is the spring constant of the last Maxwell element which is supposed to be purely elastic.(*163*) The influence of chitosan concentration on shear stress response was investigated first.

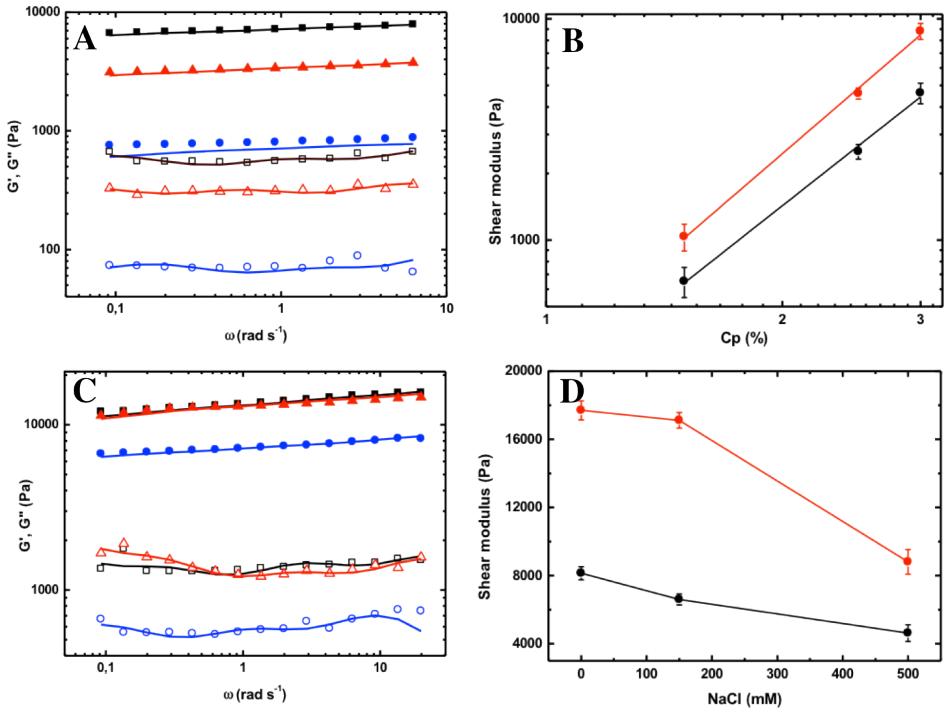

Figure 9. (A) G' (full symbols) and G" (open symbols) for chitosan-TPP hydrogels at a total polymer concentration of 3% (black squares), 2.5% (red triangles) and 1.5% (blue circles). (B) Dependence of the shear modulus - red solid line - (± SD) and G_e - black solid line - (± SD) *versus* C_p. (C) G' (full symbols) and G" (open symbols) for hydrogels versus NaCl concentration of 0 mM (black squares), 150 mM (red triangles) and 500 mM (blue circles). (D) Dependence of the shear modulus - red solid line - (± SD) and G_e - black solid line - (± SD) *versus* NaCl concentration. Reprinted with permission from (*168*). Copyright 2014, American Chemical Society.

Figure 9A compares the relaxation spectra of chitosan hydrogels with different chitosan concentration, TPP and NaCl concentrations of 1.5% and 500 mM, respectively. Lines represent the fitting of the experimental data according to equations (1) and (2). Experimental data were efficiently fitted by the generalized Maxwell model. Samples with a polymer concentration of 1.5% were fitted adequately by means of three Maxwell elements whereas hydrogels with concentrations of 2.5 and 3% required four spring-dashpot elements. The use of the generalized Maxwell model to describe chitosan systems enables the shear modulus, G, to be calculated as

$$G = G_e + \sum_{i=1}^{n} G_i \quad (3)$$

By fitting data shown in Figure 9A according to equation (3), this modulus was found to scale ($R^2 > 0.99$) with the total polymer concentration (C_p) according to the following power law $G \propto 296.6\ C_p^{3.1}$ (Figure 9B). Herein, red solid line represents the best fit of the experimental results. These findings are in agreement with those of Kong *et al.*, who described a non-linear dependence of shear modulus *versus* polymer concentration for high molecular weight alginate hydrogels in the range 2 to 4.5% w/v.(*173*) As expected, these results indicate that mechanical performance of hydrogels *versus* shear stress is influenced by the increase of polymer concentration. A similar trend was identified for the purely elastic spring G_e who was found to scale in an analogue manner ($G_e \propto 206.5\ C_p^{2.8}$, $R^2 > 0.99$). The effect of NaCl on mechanical behavior of hydrogels was then investigated. Figure 9C shows the mechanical spectra of chitosan hydrogels at different NaCl concentrations and constant chitosan and TPP concentrations (3 and 1.5%, respectively). Lines represent the fitting of the experimental data according to equations (1) and (2). In this case, shear modulus was not influenced significantly when NaCl (150 mM) was added to the system with respect to the salt free hydrogel (Figure 9D). However, shear modulus decreased when the sodium chloride concentration was increased further to 500 mM. A similar behavior was demonstrated for the G_e parameter that was found to progressively diminish by augmenting NaCl concentration. This result is in a very good agreement with those of Huang *et al.* who demonstrated that at high concentration of NaCl (500 mM) the chitosan-TPP binding is weakened.(*170*) This suggests that NaCl evokes screening effects. Similar experimental results were observed upon varying TPP concentration at constant polymer and NaCl concentrations (3% and 150 mM, respectively). By increasing cross-linking ion concentration (1, 1.5 and 3%) shear modulus was found to be 12.0 ± 0.5, 17.0 ± 0.5 and 9.3 ± 0.3 kPa, respectively. At the lowest concentration of tripolyphosphate (*i.e.* 1%), hydrogels showed the shear modulus higher than hydrogels with 3% of TPP. This might be due to the very fast binding of the anion by the polysaccharide in the latter case that, despite the macroscopic continuous network formed (Table 3), induces anisotropy in polysaccharide distribution with the formation of a more liquid-like core. On the other hand, the best mechanical response was observed in hydrogels with 1.5% of TPP. Rheological data clearly suggested that the best mechanical behavior was observed only for a very narrow range of chemical concentrations explored, compared with those indicated in Table 3. To summarize, from rheological analyses we identified two optimum conditions for hydrogel formation: chitosan 3%, TPP 1.5%, NaCl 150 mM, glycerol 5% (*a*) and chitosan 3%, TPP 1.5%, glycerol 5% (*b*). Since rheological tests did not point out

significant differences between formulation *a* and *b*, the mechanical behavior of both formulations was evaluated considering a different stress condition, *i.e.* uniaxial compression. These measurements were performed by applying a very slow compression stress to the material, which induces an elastic deformation of the polymeric network. The toughness at 70% of total strain was used as a parameter to compare the two formulations (Figure 10).

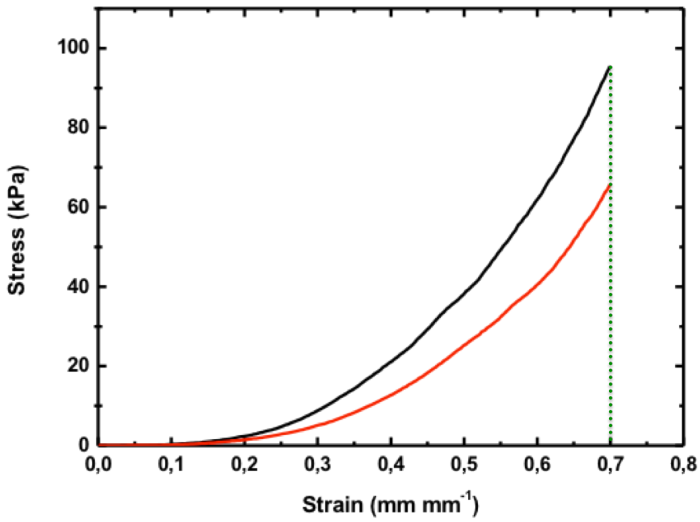

Figure 10. Representative stress-strain curves of the hydrogels under uniaxial compression. Black line: *a* (with supporting salt NaCl); red line: *b* (without supporting salt NaCl). Dashed green line represents the 70% of total strain. Reprinted with permission from (*168*). Copyright 2014, American Chemical Society.

By integrating the areas under stress-strain curves, the toughness values were 20.5 ± 5.0 and 9.6 ± 1.5 kJ m^{-3} for *a* and *b*, respectively. These data point out that, in the presence of supporting salt (*a*) the hydrogels are able to accumulate significantly ($p < 0.05$, $n = 3$) more energy than hydrogels without NaCl (*b*). These results clearly indicated that the former showed a better mechanical performance in compression compared to the latter. The interpretation of these results is somewhat unclear but it can be speculated that, although a continuous network is formed in both cases (Table 3), an anisotropic distribution of the polysaccharide component takes place which results in a stiffer structure. Given these results, formulation *a* was selected as the best candidate for further characterization studies and to optimize the preparation of dried membranes.

In order to investigate the interaction between chitosan and TPP, FTIR-ATR analyses were

performed. Figure 11 shows the spectra of freeze-dried chitosan, membrane and TPP powder.

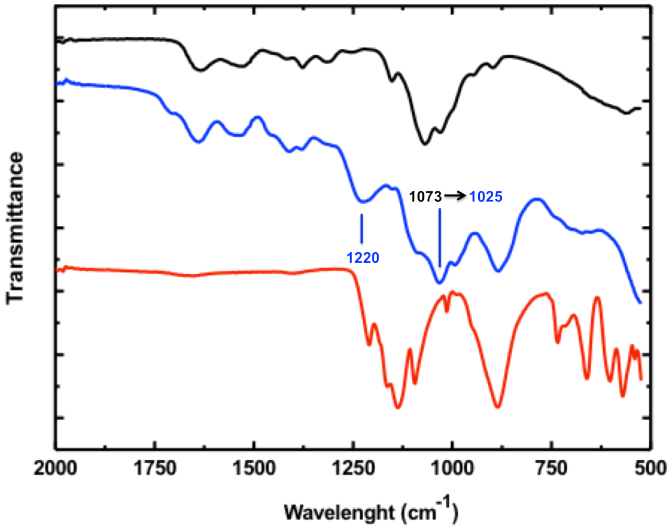

Figure 11. FTIR-ATR spectra of freeze-dried chitosan (black line), *a* membrane (blue line) and TPP powder (red line). Reprinted with permission from (*168*). Copyright 2014, American Chemical Society.

Chitosan-TPP membrane was developed starting from the best candidate hydrogel *a*. FTIR spectrum of freeze-dried chitosan (black line) showed two characteristic peaks at about 1645 and 1550 cm^{-1} which were attributed to C=O stretching in amide group (amide I vibration) and N-H bending in amide group (amide II vibration), respectively. The peak at 1375 cm^{-1} was attributed to the distorting vibration of C–CH_3 bond.(*174*) Absorption bands at 1150 (anti-symmetric stretching of the C-O-C bridge), 1070 and 1025 cm^{-1} (skeletal vibrations involving the CO stretching) are characteristic peaks of the chitosan structure.(*175*) TPP spectrum shows peaks at 1210 (P=O stretching), 1140 (symmetric and anti-symmetric stretching vibrations in PO_2 group) and 1093 cm^{-1} (symmetric and anti-symmetric stretching vibrations in PO_3 group).(*176*) Spectrum referring to membrane showed the appearance of the novel band at 1220 cm^{-1}, corresponding to anti-symmetric stretching vibrations of PO_2 groups and the significant shift of the peak at 1073 in dried chitosan to 1025 cm^{-1} in membrane. These peaks confirm the formation of ionic cross-links between NH_3^+ groups of chitosan and tripolyphosphate anions in agreement with the literature. Chitosan-TPP interactions were also investigated in diluted 0.2 M acetic acid-150 mM NaCl solutions by exploiting ^{31}P-NMR. The latter analyses (Figure 12) showed

the presence of characteristic peaks in TPP spectrum referring to orthophosphate (0.266 ppm), pyrophosphate (-10.398 ppm) and triphosphate (-10.284 ppm: α terminal phosphorus; -22.679 ppm: β middle phosphorus atoms. JP, P = 19.5 Hz) species according to the literature.(*177*),(*178*)

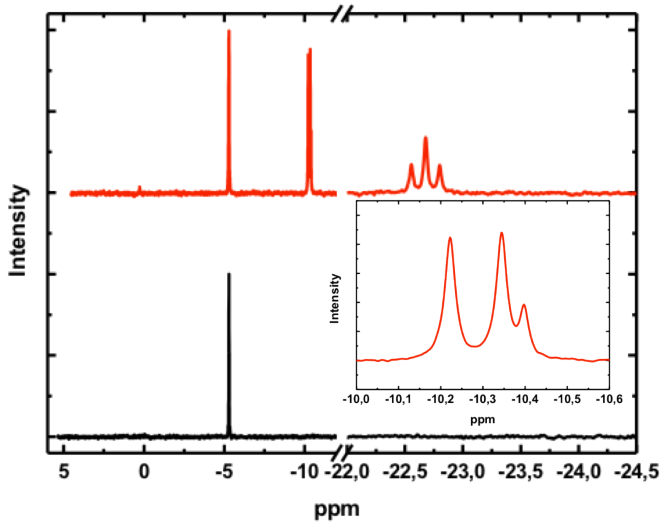

Figure 12. ^{31}P-NMR spectrum of TPP (0.3% w/v) solution (red spectrum). The peak at -5.288 ppm refers to PPh_3. Inset: magnification of the signal referring to PPi and α terminal phosphorus of TPP. Black spectrum: ^{31}P-NMR of diluted solution composed by TPP (0.3% w/v), NaCl (150 mM) and chitosan (3.6 g L^{-1}). Reprinted with permission from (*168*). Copyright 2014, American Chemical Society.

By integrating the area under peaks, it was revealed that the percentage of orthophosphate and pyrophosphate was 1 and 17% w/w, respectively, and that of TPP was 82% w/w. This is in line with the 85% w/w purity of tripolyphosphate reported by the producer. The pKa values reported in the literature are: orthophosphoric acid pKa_1 2.17, pKa_2 7.31, pKa_3 12.36; pyrophosphoric acid pKa_1 very small, pKa_2 2.64, pKa_3 6.76, pKa_4 9.42; tripolyphosphoric acid pKa_1 and pKa_2 very small, pKa_3 2.30, pKa_4 6.50, pKa_5 9.24.(*179*) Thus, in the present medium (containing 0.2 M acetic acid) the most abundant species should bear one negative charge in the case of orthophosphate, two charges in the case of the pyrophosphate, and three charges in the case of tripolyphosphate, one on each monophosphate unit in the latter two cases. When chitosan was added to the cross-linking ion solution, the signals of TPP and pyrophosphate disappear, being broadened beyond detection limit by the strong interaction with the polymeric chain, extremely slowly

reorienting. Also the orthophosphate signal seems to disappear likely indicating that it binds to chitosan, although the very low signal prevents a clear interpretation.

To assess the amount of tripolyphosphate embedded within the best candidate hydrogel, a spectrophotometric method was exploited based on an acid hydrolysis of TPP by means of hydrochloric acid followed by a colorimetric reaction with a mixture of vanadium-molybdenum salts. The reaction rate of TPP hydrolysis is equal for all samples analysed, provided pH and time treatment are equal. Thus, the comparison of the absorbance of the sample and those of solutions containing known amounts of tripolyphosphate provides a direct evaluation on the TPP concentration. Considering that the concentration of TPP in the gelling bath is equal to 1.5% w/v, the TPP concentration entered in the hydrogel was equal to 0.2% w/v, calculated on the basis of the amount of TPP measured in hydrogel by the spectrophotometric method. Thus, only a limited amount of TPP (estimated to be about 13%) was uptaken. To better understand how the concentration of TPP and other phosphates present in the gelling bath decreased upon time, ^{31}P-NMR spectra were performed on the gelling solution. The chemical shifts of the ^{31}P-signals did not change with time, at variance with their integrated intensities that allowed calculating the concentration that results 1.3% w/v (about 13.3%) after 24 h in agreement with the spectrophotometric method. In addition, NMR spectroscopy enables to distinguish the signals of the phosphate species. The P, PPi and TPP concentrations slowly decreased over time as depicted in Figure 13, in accordance with an anion uptake by the chitosan solution.

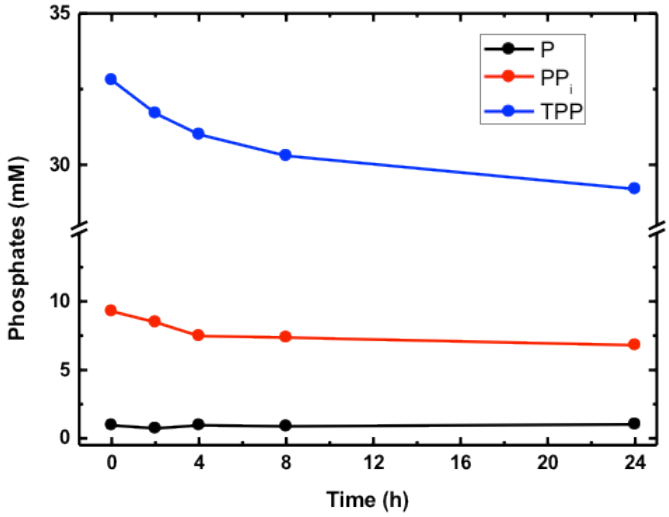

Figure 13. Concentration decrease of P (black line), PPi (red line) and TPP (blue line) species (mM) with time (h) in the gelling solution as calculated from the integrals of ^{31}P-NMR spectra. Reprinted with permission from (*168*). Copyright 2014, American Chemical Society.

The orthophosphate concentration was very small and did not significantly vary, whereas the TPP and PPi concentrations (mM) decreased appreciably in 24 hours (from 32.80 at t = 0 h to 29.20 at t = 24 h and from 9.28 at t = 0 h to 6.79 at t = 24 h, respectively). PPi present as minor component in the commercial TPP sample used did not hamper the hydrogel formation. Indeed, it was reported that it is able to ionically cross-link polyelectrolytes, chitosan included.(*180*),(*181*) The molar ratio of the latter two species (TPP/PPi) increased from 3.53 (t = 0 h) to 4.30 (t = 24 h). The decrease of TPP and PPi concentrations due to diffusion into chitosan solution during the dialysis was 3.6 and 2.4 mM, respectively. Therefore, the contribution of PPi to the gelation process cannot to be ruled out. Indeed, the spectrum of chitosan-TPP mixture depicted in Figure 12 showed the disappearance of peaks at -10.398, -10.284 and -22.679 ppm, respectively, indicating that both TPP and PPi are implicated in binding with the polymer.

The swelling capacity of ionically cross-linked hydrogels plays an important role to evaluate their potential use as biomaterials for biomedical applications. Swelling is mainly influenced by ionic interactions between chitosan chains, depending in turn on the cross-linking density.(*182*),(*183*) With the aim of investigating the swelling behavior of *a* hydrogels in physiological pH conditions, the water loss kinetics of samples was followed in PBS buffer at room temperature for 24 h and the results are reported in Figure 14. Samples were characterized by a fast de-swelling that took place during the first 7 hours.

Further, the loss of solvent was basically stable up to 24 h (from -19.32 ± 4.97 to -20.28 ± 5.89%). To explain the loss of solvent experienced by the hydrogels, it should be noted that during the hydrogel formation the dialysis took place at a pH of ~ 4.3 for *a*. In this case, chitosan amino groups are almost completely protonated. When hydrogels are placed in PBS with pH of ~ 7.4, chitosan amino groups are mostly in the form of $-NH_2$, which makes it insoluble and leads to a shrinkage of the network with a loss of solvent. The same effect was observed by Lopez-Leon and co-workers who demonstrated that the diameter of chitosan-TPP nanoparticles diminished appreciably when pH was varied from 4 to 7.(*184*)

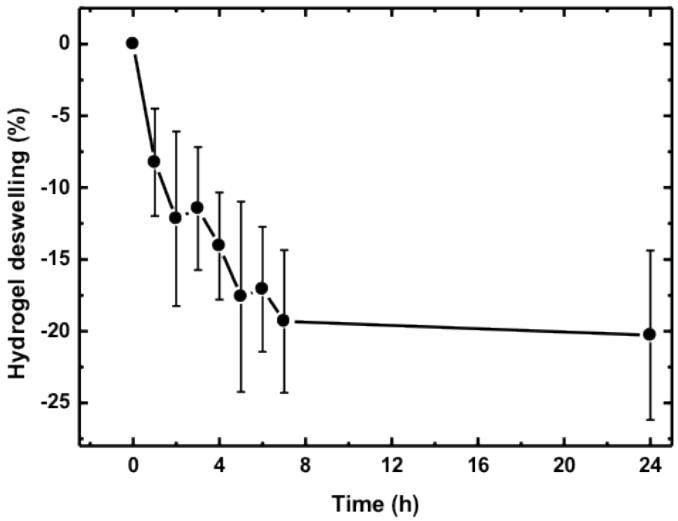

Figure 14. Hydrogel de-swelling (%) versus time (h) of *a* hydrogels. The data are expressed as mean (± SD) of three samples. Reprinted with permission from (*168*). Copyright 2014, American Chemical Society.

The cytotoxicity characterization has been carried out on the prototype membranes obtained by freeze-drying. LDH assay was performed on mouse fibroblasts using the freeze-dried sample *a*. As reported in Figure 15, membranes did not exert any cytotoxic effect both when the material was placed directly in contact with cells and when the extract medium was added on the cell layer. Indeed, there was no significant difference in the release of lactate dehydrogenase between sample-treated cells and negative control groups (indicated as Ps and Ad, respectively) after 24 and 72 h.

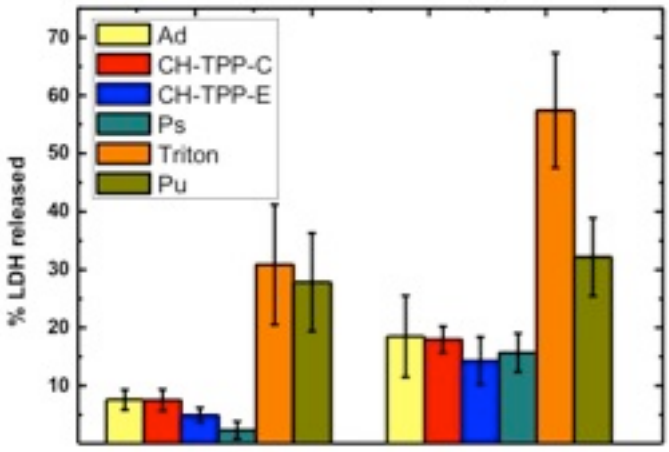

Figure 15. Effect of the freeze-dried sample *a* on NIH-3T3 cell line. The cytotoxicity test was performed both with the extract from the sample (CH-TPP-E) and with the sample in direct contact with cell layer (CH-TPP-C). Control cells cultured in adhesion in complete DMEM medium (Ad). Polyurethane sheets (Pu) were used as contact positive control, plastic poly(styrene) sheets (Ps) were used as contact negative control and Triton X-100 was used as extract positive control. Adapted with permission from (*168*). Copyright 2014, American Chemical Society.

3.1.4. Main conclusions

- Tridimensional hydrogels and dried membranes based on chitosan and TPP have been developed by exploiting a slow ion diffusion technique;
- Only a limited group of chitosans allowed the formation of matrices;
- Not only TPP but also PPi contribute to the gelation of chitosan;
- Dried membranes derived from best candidate hydrogel proved lack of cytotoxicity.

CHAPTER II

Investigation on the ionotropic gelation of chitosan in dilute solutions and tridimensional hydrogels

3.2.1. Aim of work

This section tackles the investigation upon the onset of TPP-PPi binding to chitosan in diluted solutions by using complementary techniques with respect to the common ones reported in literature and finally the study of the different contribution of both the polyions to the formation of hydrogels chitosan-based obtained by a slow ion diffusion technique reported in the previous chapter. In this section, the ability of the non-traditional cross-linker PPi giving rise to the formation of wall-to-wall networks is demonstrated.

3.2.2. Materials and methods

3.2.2.1. Materials. Medium molecular weight chitosan (Fa: 0.23 determined by ^{1}H-NMR; viscosity 200 - 800 cP declared by producer), was purchased from Sigma-Aldrich and purified by precipitation with isopropanol, followed by a dialysis against deionized water. Sodium tripolyphosphate pentabasic - $Na_5P_3O_{10}$ - (TPP ≥ 98.0%), sodium pyrophosphate tetrabasic - $Na_4P_2O_7$ - (PPi ≥ 95%), NaCl and glycerol (*ReagentPlus*® ≥ 99.0%) were all purchased from Sigma-Aldrich.

3.2.2.2 Light Scattering (Turbidimetry). A Perkin-Elmer LS50B spectrofluorimeter was used to record the intensity of the light scattered (90°) by diluted chitosan solutions (0.05% w/v and 2 mL as final volume), upon irradiation with a 550 nm incident light (T = 25 °C). Chitosan was solubilized in acidified deionized water (pH = 2.6) and resulting solutions were titrated using either TPP or PPi solutions (6 μL injections) to gradually increase the molar ratio (r) between the cross-linker and the monomeric unit of chitosan (r = [crosslinker] / $[\text{monomeric unit}]_{ru}$). Each injection increased r by 0.02 units. Before analysis, solutions were allowed to equilibrate for one minute. Considering the contribution of *N*-acetylglucosamine unite, the molecular mass of chitosan monomeric unit resulted 171 g mol^{-1}.

3.2.2.3 Circular dichroism (CD). CD spectra of dilute chitosan solutions (0.05% w/v) were recorded in acidified deionized water (pH = 2.6) with a Jasco J-700 spectropolarimeter. The chitosan solution was titrated using either TPP or PPi solutions (3 μL injections) to gradually increase *r*. Each injection increased *r* by 0.02 units. For all measurements, the volume of each injection was considered negligible with respect to that of chitosan solution (1 mL): in fact, the volume increase (*i.e.* chitosan dilution) was about 13% at *r* = 1, while *r* never exceeded 0.24, corresponding to a dilution of less than 4%. Before analysis, solutions were allowed to equilibrate for one minute. Ellipticity of titrated solutions (θ_r) was normalized by that of chitosan (θ), with no correction for dilution. Data are expressed as values of reduced specific ellipticity in agreement to the equation

$$\Delta\theta = -(\theta_r - \theta)/|\theta|$$

A quartz cell of 1 cm optical path length was used, always using the following setup: bandwidth 1 nm, time constant 2 s, scan rate 20 nm min^{-1}. Three spectra were averaged for each measurement.

3.2.2.4 Nuclear magnetic resonance (^{1}H-NMR). ^{1}H-NMR analyses were performed on chitosan solutions (0.2% w/v in 0.2 M acetic acid as a solvent, pH = 2.6), with addition of TPP or PPi with final value *r* = 0.16. The ^{1}H-NMR spectra were recorded at 25 °C, on a Varian VNMRS (11.74 T) NMR spectrometer operating at 499.65 MHz for proton. Water suppression was accomplished by means of WET.(*185*) A total of 512 scans were accumulated with a spectral width of 6 kHz over 16384 complex data points. The data were multiplied by a decaying exponential function (broadening factor 0.5 Hz) and zero filled twice prior to Fourier transform. The chemical shifts are referred to the chemical shift of the proton of HOD at 4.645 ppm.

3.2.2.5 Chitosan hydrogels preparation. Wall-to-wall hydrogels were obtained by the slow diffusion technique presented in the previous chapter. Chitosan (3% w/v) was hermetically sealed and immersed into a gelling solution (final volume 50 mL) containing anions (TPP or PPi) - NaCl (150 mM) - glycerol (5% v/v). TPP and PPi concentrations were varied so that *r* spanned in the range from 0.3 to 7. Ion diffusion proceeded for 24 h

under moderate stirring at room temperature allowing hydrogel formation.

3.2.2.6 Mechanical spectroscopy. Rheological characterization of TPP/PPi chitosan hydrogels was performed by means of a controlled stress rheometer Haake Rheo-Stress RS150 operating at 25 °C using a shagreened plate apparatus (HPP20 profiliert: diameter = 20 mm) as the measuring device. To avoid water evaporation from the hydrogel, measurements were performed in a water-saturated environment formed by using a glass bell (solvent trap) containing a wet cloth. In addition, to prevent both wall-slippage(*163*) and excessive gel squeezing, the gap between plates was adjusted, for each sample, by executing a series of short stress sweep tests (ν = 1 Hz; stress range 1 - 5 Pa) characterized by a reducing gap.(*164*) The selected gap was that maximizing the value of the elastic modulus G' (used gaps ranged between 2.5 and 2.0 mm). For each hydrogel, the linear viscoelastic range was determined by means of a stress sweep test consisting in measuring elastic (G') and viscous (G") moduli variation with increasing shear stress (1 Pa < τ < 5 Pa) at a frequency ν = 1 Hz (hence with $\omega = 2\pi\nu$ = 6.28 rad s^{-1}). The mechanical spectrum of hydrogels was determined by measuring the dependence of the elastic (G') and viscous (G") moduli from the pulsation ω at constant shear stress τ = 5 Pa (well within the linear viscoelastic range which, for all samples, spans up to at least 30 Pa).

3.2.2.7 Evaluation of homogeneity. The homogeneity of the TPP and PPi hydrogels was assessed by means of the method reported elsewhere.(*186*) Briefly, cylindrical hydrogels were cut perpendicular to the cylinder axis into five slices with roughly the same thickness (5 mm). Only for these studies, the controlled gelation of chitosan was reached by exploiting a dialysis tube (diameter 25 mm) flooded into the same gelling solution mixture described in paragraph 2.5. After measuring their wet weights by an analytical balance, the slices were dried at 40 °C for 24 h. Samples were weighed again after drying, and their dry/wet weight ratios (D_w / W_w) were calculated.

3.2.2.8 Image analyses. Image analyses were carried out on TPP and PPi hydrogels cross-sections. Hydrogel slices of approximately 1 mm of thickness were dried in ethanol 70% v/v and overnight contrasted using $UO_2(CH_3COO)_2$ 0.2% w/v. Subsequently slices were totally dried in ethanol 100% v/v and finally embedded in Epoxy resin after completely removing the alcohol. Ultrathin sections were cut by means of a microtome (equipped with a diamond blade) and gently deposited onto Nickel grids. Visual analysis and image record were performed using a PHILIPS EM Transmission Electron Microscope.

3.2.3. Results and discussion

TPP is by far the most employed cross-linker to ionically reticulate chitosan due to its high net negative charge (ranging from one to five based on pH) per monomeric unite. For instance, TPP was successfully exploited to obtain chitosan nanoparticles and nano/micro-gels.(*187*),(*145*),(*170*) In spite of this, the colloidal stability of these systems is deeply affected by many parameters as well as polymer and cross-linker concentrations, pH, ionic strength, temperature and so on.(*188*) In recent years, the group of Lapitsky shed light on molecular interactions and formation process regarding the chitosan-TPP system.(*170*),(*189*) Moreover, they also proved that not only TPP but also PPi was able to boost the ionotropic gelation of chitosan until to obtain stable suspensions of nanoparticles.(*180*),(*181*) Nevertheless, both nanoparticles and nano/micro-gels based on the common gelation of chitosan (by means of either TPP or PPi) represent inhomogeneous systems with uneven structure which can not be applied for the fabrication of tridimensional matrices, as well as hydrogels, characterized by specific shapes.

To study the interactions between chitosan and the cross-linker in dilute solutions, light scattering (turbidimetry), circular dichroism and ^{1}H-NMR techniques were considered.

About turbidimetry analyses, the relative intensity (90°) of chitosan solutions in water upon addition of TPP and of PPi was measured and reported in Figure 16 as a function of the molar ratio, *r*, between the cross-linker and monomeric unit of chitosan. In agreement with published data obtained by dynamic light scattering,(*180*) the addition of TPP is immediately accompanied by an increase of the scattering (up to the maximum measurable value), whereas in the case of PPi only a moderate, albeit non negligible, increase is observed up to about $r = 0.4$, followed by an abrupt increase of the observed scattering up to the (experimental limiting) value of about $r = 0.5$. For both TPP and PPi, at the highest accessible *r* value the solution becomes clearly turbid.

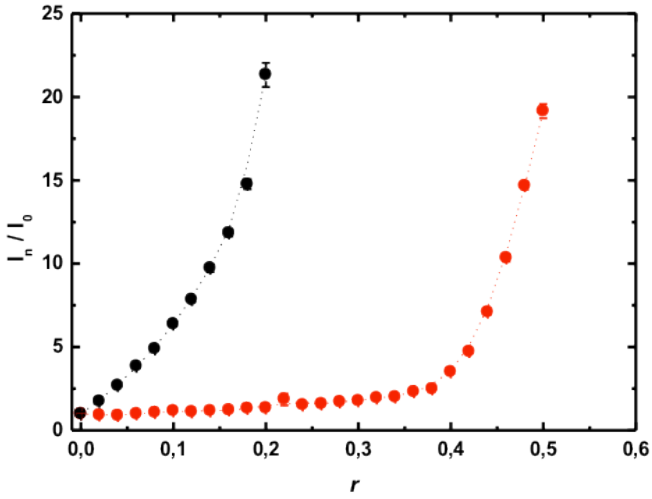

Figure 16. 90° scattered light for chitosan solutions titrated either with TPP (black dots) or PPi (red dots). The total polymer concentration was 0.05% w/v in all of the cases analyzed. Data are expressed as the ratio between the intensity of titrated solutions (I_n) and the intensity of that of chitosan alone (I_0) *vs*. the molar ratio between cross-linker and monomeric unit of chitosan (*r*). Values are reported as mean (±SD, $n = 8$). Dotted curves are drawn to guide the eye.

Circular dichroism is a versatile technique already employed in the study of polysaccharides and their mixtures.(*190*),(*191*) Since chitosan is a chiral molecule presenting the *N*-acetylglucosamine chromophore group which absorbs radiation in the range of 200 - 250 nm, it is possible to record its CD spectrum. Figure 17A reports the CD spectrum of a 0.05% w/v chitosan solution showing the presence of a negative minimum at ~ 210 nm referring to the UV-absorption (stemming from the $n \rightarrow \pi^*$ transition) of the *N*-acetilglucosamine unit.(*192*) Titration of the chitosan solution by means of either TPP or PPi solutions was performed by gradually increasing the molar ratio *r* between cross-linker and the repeating unit of chitosan. Figure 17B shows the variation of chitosan ellipticity following titration with both cross-linkers. The experimental CD data have been reported as the ratio of the (relative) difference of ellipticity between the solution - at a cross-linker-to-polymer ratio of *r* - and the cross-linker-free polymer solution, over the (absolute value of) the ellipticity of the polymer, $\Delta\theta$.

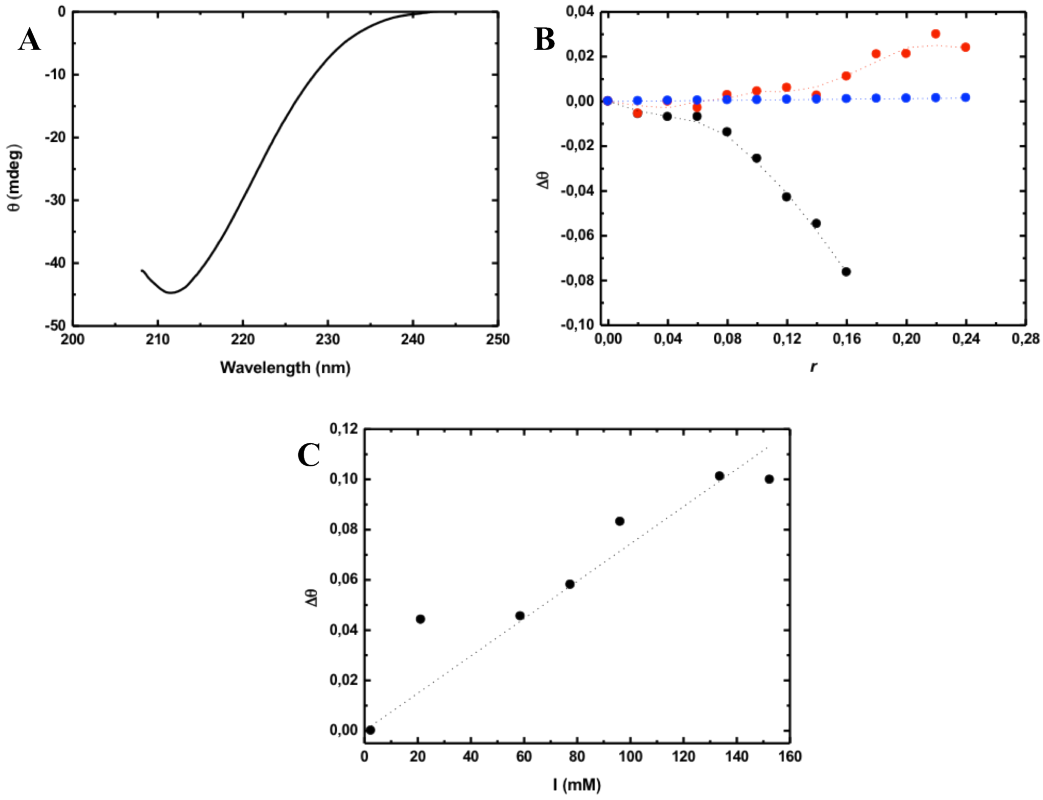

Figure 17. (A) CD curve of the chitosan solution (0.05% w/v) in acidified deionized water (pH = 2.6). (B) Variation of reduced ellipticity by consecutively titrating previous polymer solution by means of either TPP (black dots) or PPi (red dots); blue dots represent the variation of reduced ellipticity due to the ionic strength determined by the PPi anions; dotted curves are drawn to guide the eye. (C) Variation of reduced ellipticity for chitosan solutions with constant polymer concentration (0.05% w/v and different ionic strength, I, due to the presence of $NaClO_4$, pH = 2.6; dotted line represents the best linear fitting among experimental points ($\Delta\theta \; \alpha \; 7 \cdot 10^{-4} \; I$).

In the case of TPP, all observed variations are negative, and the shape of the CD curve *versus*. *r* closely parallels that of the scattering intensity (cfr. Figure 16), suggesting that the two processes are simultaneous. To ensure that the small, albeit well detectable, relative CD change (at most 8% of the original value) does not stem from artifacts deriving from the formation of chiral aggregates,(*193*) the position of the cuvette along the optical path was varied with respect to the detector. Even at the highest *r* value investigated no change in the measured ellipticity was observed, thus confirming the molecular origin of the observed change. To ascertain whether the observed $\Delta\theta$ stems from a specific TPP/chitosan interaction or from a non-specific electrostatic effect caused by the notable change in the solution ionic strength (I) brought about by the multivalent anion, $\Delta\theta$ was

measured for chitosan solutions (at constant polymer concentration = 0.05% w/v) increasing I from zero to 150 mM by $NaClO_4$. The results are reported in Figure 17C: they indicate that a positive $\Delta\theta$ is brought about by an increase of I. However, the calculated effect due to change of ionic strength in the *r* domain of the significant variations induced by TPP is totally negligible, thus pointing to a specific effect of the multivalent species on the chitosan chain. On the other hand, when using PPi as anion for the titration of chitosan solution, the relative increase of the CD change was much lower than in the case of TPP, but opposite in sign (at least for $r > 0.15$), where the $\Delta\theta$ became slightly larger than experimental uncertainty (Figure 17B). Also in this case, the observed $\Delta\theta$ effect in the higher range of *r* is by far larger than that induced by I alone. Circular dichroism clearly demonstrated the higher binding affinity of TPP with respect to PPi for the chitosan chains. This may be ascribed to the presence of an extra negative charge in the case of TPP. Indeed, at the pH values here investigated, TPP and PPi should bear almost three and two negative charges, respectively, one on each monophosphate unit.

To get further insights into the behavior of chitosan upon binding with both anions, ^{1}H-NMR measurements were performed. A molar ratio (*r*) of 0.184 was chosen for comparison purposes.

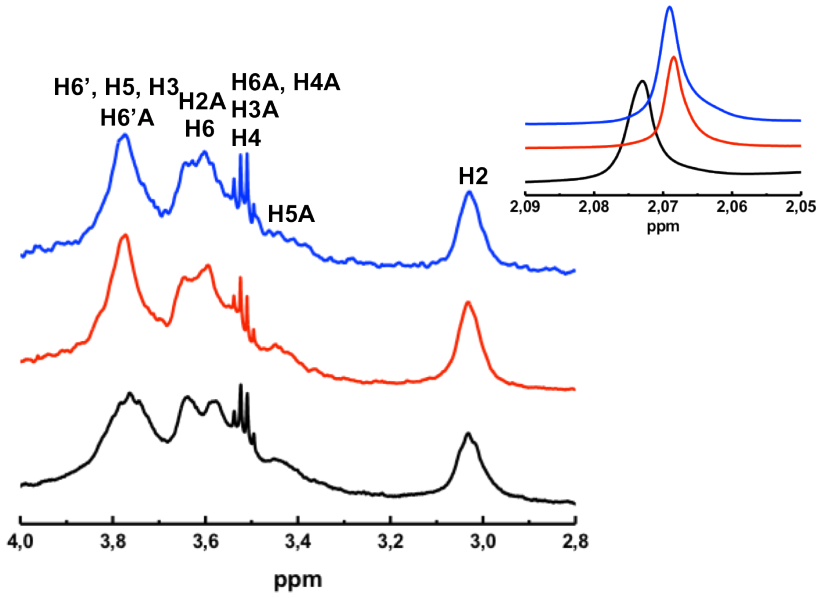

Figure 18. ^{1}H resonances in the 4 - 2.8 ppm spectrum region for chitosan (black solid line), chitosan + PPi (red solid line) and chitosan + TPP (blue solid line) with cross-linker/chitosan monomeric unit ratio (*r*) of 0.16 in 0.2 M CH_3COOH solution (pH = 2.6). The assignments for glucosamine and *N*-acetylglucosamine protons (labelled as A) according to literature are reported.(*194*) Inset: the low field ^{13}C satellite of AcOH-Ac in the same order as the main figure.

In the presence of either TPP or PPi, the signal of the methyl group of acetate-acetic acid experienced a slight shift (by about 0.005 ppm) to lower frequencies owing to the increase of the amount of acetate caused by the base addition. In the inset of Figure 18 was reported the low field carbon satellite of the acetate-acetic acid pair. On the contrary, glucosamine H2 proton, which is sensitive to pH changes,(*132*) is unaffected by the small base addition in line with the lower acidity of chitosan with respect to acetic acid. These results rule out deprotonation as origin of the conformational changes detected by CD, which therefore should be attributed to chitosan interaction with multivalent anions. Rather, the presence of TPP and PPi affects the pattern of the envelope of the overlapped resonances of most protons of chitosan monomeric units, between 3.9 and 3.5 ppm (Figure 18), in agreement with the occurrence of conformational changes. Hence, a probable explanation to light scattering, CD and ^{1}H-NMR observations seemed to point to a gradual neutralization of chitosan charge when strong interactions with polyphosphate anions occurred, as already demonstrated by means of Z-potential measurements,(*170*) bringing about a conformational reconfiguration.

In the previous chapter it was already demonstrated to fine control the ionotropic gelation

of confined chitosan by tuning polymer, TPP and NaCl concentrations to obtain macroscopic hydrogels. The work presented in this section aimed at exploring on the ability of PPi to form tridimensional matrices by exploiting slow ion diffusion technique and, consequently, to study the different mechanical behavior or resulting matrices. In order to achieve this purpose, chitosan concentration was kept constant (3% w/v) in the vessel and different cross-linker concentrations were selected so as to vary *r*. It is noteworthy that the aforementioned molar ratio was calculated taking into account the concentration of cross-linker at the beginning of the dialysis so as to exclude diffusion phenomena. For both anions, no hydrogel formation occurred for $r < 3.1$. Upon exceeding this limit, the formation of wall-to-wall systems by both cross-linkers took place. These results represent a very interesting finding in the case of PPi as a promising strategy to develop tridimensional matrices by the use of this anion.

When the dialysis starts, TPP or PPi migrate through the semipermeable membrane and bind to positive chitosan: the ionotropic gelation takes place and the confined viscous chitosan solution tends to gradually become opaque. This phenomenon is due to the cooperative self-assembly process between chitosan and cross-linkers, as already discussed above, which proceeds through a two-step process: (*i*) the formation of small primary nanoparticles and (*ii*) their aggregation into larger, higher-order colloids.(*195*),(*189*) Nevertheless, in this system an additional step has to be considered, the aggregation of higher-order colloids, so simply named microgels, until to obtain a macroscopic network (Figure 19). The slow diffusion of both TPP and PPi through dialysis membranes, assisted by the screening effect of the supporting salt NaCl and by hydrophobic interactions between polymer's chains, enables to fine control the self-assembling of microgels until an opaque wall-to-wall system was obtained.

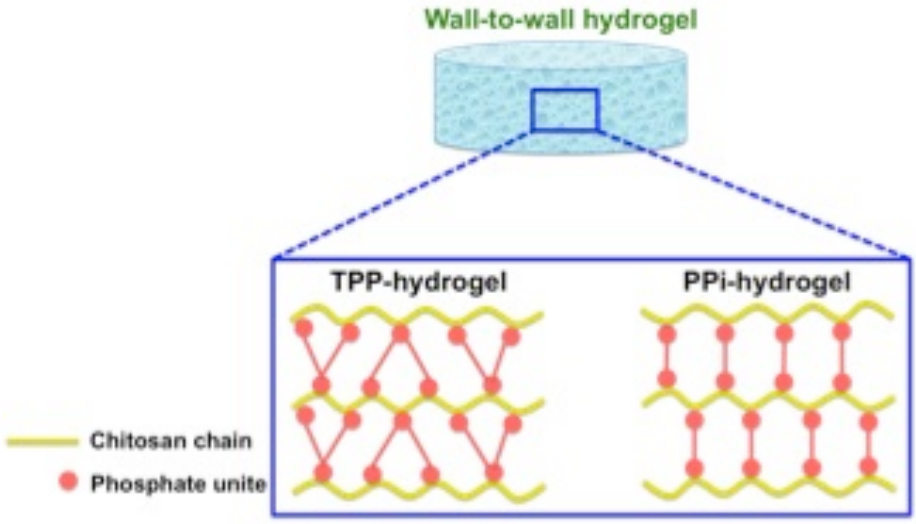

Figure 19. Wall-to-wall hydrogel chitosan-based obtained by slow ion diffusion technique. The inset represents the hypothetical disposition of junctions within the hydrogel where polymer chains (yellow ribbons) bind either TPP or PPi by electrostatic interactions. Cross-linkers are represented as reddish dots where each one may be considered as a single phosphate unite or a single negative charge.

In order to investigate the different mechanical behavior of resulting hydrogels, rheological measurements were performed. Frequency sweep analyses were carried out to record mechanical spectra of hydrogels undergone to a constant shear stress (Figure 20).

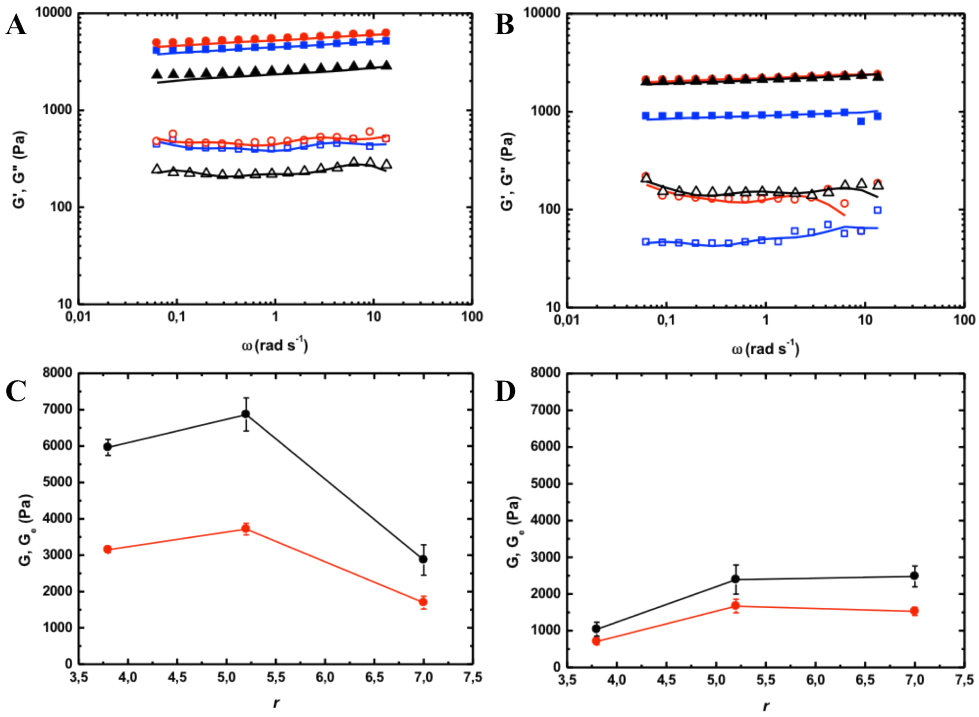

Figure 20. G' (full symbols) and G'' (open symbols) for chitosan-TPP (A) and chitosan-PPi (B) hydrogels at different cross-linker/glucosamine unite molar ratios (*r*) of 3.8 (blue squares), 5.2 (red circles) and 7.0 (black triangles); solid lines represent the best fitting by means of Maxwell model. Dependence of the shear modulus (±SD), black solid line, and Ge (±SD), red solid line, *versus* different *r* for chitosan-TPP (C) and chitosan-PPi (D) hydrogels.

Experimental measurements were fitted by means of Maxwell model described elsewhere.(*172*) The number of Maxwell elements (sketched by a sequence of elastic springs, of constant G_i, and viscous dashpot elements) was selected through a statistical procedure to minimize the product $\chi^2\, n$, where χ^2 is the sum of the squared errors between experimental and model fitting values while n is the number of fitting parameters. Mechanical spectra in Figure 20A-B point out that both storage (G') and loss moduli (G'') differ of approximately one order of magnitude for almost two decades of frequency, thus indicating the strong nature of TPP-PPi hydrogels. By means of Maxwell model the shear modulus (G) can be easily calculated according to equation (3) reported in previous chapter.

Shear modulus is a pivotal parameter to assess the stiffness of a material. In general terms, it has been found that shear moduli of TPP-containing hydrogels were higher than those prepared using PPi. Specifically, in the case of TPP hydrogels the shear modulus at r = 3.8

was higher than those with r = 7.0 (Figure 20C). The best mechanical response to the shear stress was observed for hydrogels with r = 5.2. The shear modulus trend for present TPP hydrogels was in line with that already demonstrated for systems obtained with a different TPP powder (technical grade 85%) as described in the previous chapter. Moreover, a similar behavior was identified for the purely elastic constant G_e. In the case of PPi hydrogels, shear modulus was found to increase with the increasing of (r) as pointed out in Figure 20D. Furthermore, the higher experimental error for PPi hydrogels (due to a less fitting by Maxwell model) suggests a partial inhomogeneity of such networks, albeit wall-to-wall matrices were obtained. In any case, shear moduli of TPP hydrogels (except for r = 7.0) were higher than those of PPi hydrogels, thus indicating higher stiffness for the first.
Moles of point-like junctions (polymeric network crosslink density, ρ) between chitosan chains per hydrogel unit volume can be calculated by exploiting the Flory's theory in agreement to the equation

$$\rho = \frac{G}{RT} \quad (4)$$

where R is the universal gas constant, T is the temperature and G is the shear modulus.(*172*) By assuming the parameter ξ as the diameter of the collection of spheres that composes an ideal network with a regular mesh, cross-link density enables to easily calculate the average network mesh size as

$$\xi = \sqrt[3]{\frac{6}{\pi \rho N_a}} \quad (5)$$

where N_a is the Avogadro number.(*172*) Outcomes for both TPP and PPi hydrogels with different amount of cross-linker are reported in Table 5. The average network mesh size was found to be smaller for TPP systems with respect to PPi ones, except for r = 7.0. For instance, the average network mesh size was assessed to be ~ 11 nm for TPP systems and ~ 22 nm for PPi ones in the case of r = 3.8. These results indicate the better reticulation of meshes for TPP hydrogels, as confirmed by the higher moles of point-like junctions for different molar ratios explored. This is consistent with those observed in CD measurements previously described. In fact, the different affinity of both cross-linkers, due to the diverse net charge contribution, affects the gelation rate so as to provide hydrogels with variable

homogeneity which responding in a different manner under a constant stress.

	PPi			TPP		
r	3.8	5.2	7.0	3.8	5.2	7.0
G (kPa)	1.04 ± 0.19	2.39 ± 0.40	2.48 ± 0.28	5.95 ± 0.22	6.87 ± 0.45	2.87 ± 0.42
ρ x 10^{-6} (mol cm^{-3})	0.29 ± 0.03	0.97 ± 0.16	1.00 ± 0.11	2.40 ± 0.09	2.77 ± 0.18	1.16 ± 0.17
ξ (nm)	22.3 ± 0.9	14.9 ± 0.8	14.7 ± 0.8	11.0 ± 0.1	10.5 ± 0.2	14.0 ± 0.7

Table 5. Physical-chemical parameters for TPP/PPi-containing hydrogels. *r* represents the molar ratio between the cross-linker and the glucosamine unite of chitosan. Shear modulus (G), polymeric network crosslink density (ρ) and average network mesh size (ξ) were calculated by means of Maxwell model and Flory's theory.

Intriguing information about the polymer meshes distribution within hydrogels may be also pointed out by means of TEM analyses. By comparing TPP-hydrogels to PPi-ones (Figure 21A and B, respectively) the different cross-linking density is shown. At a glance, networks composed of entangled polymer (dark ribbons) and not-contrasted zones (grey spaces) random distributed were observed. TEM image of TPP-hydrogels (Figure 21A) displays a homogeneous distribution of chitosan both with a wide range of pore sizes and with generally lack of aggregates. Conversely to the latter, PPi-hydrogels looked with a heterogeneous network characterized by a reduction of point-by-point connectivity. The outcomes clearly demonstrated that, albeit no discrepancies at the macroscopic level may be identified, the different reticulation throughout the network strictly affects the mechanical behavior of hydrogels.

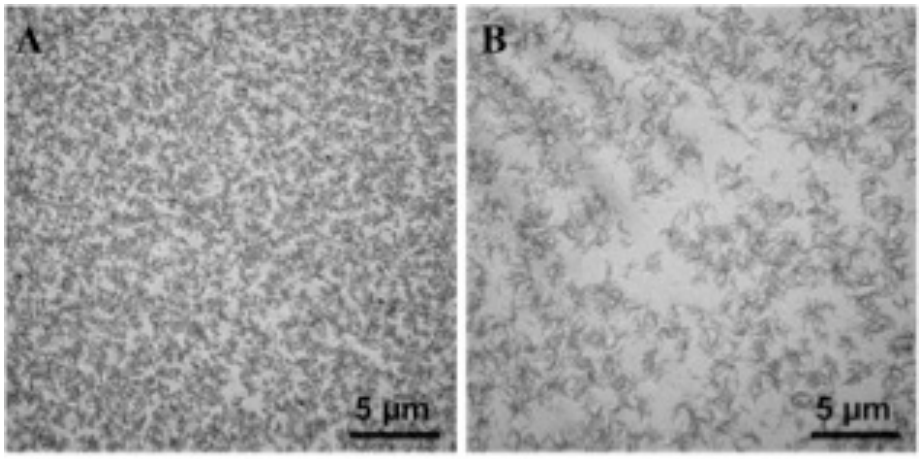

Figure 21. Chitosan meshes distribution in TPP (A) and PPi (B) hydrogel cross-sections with cross-linker/chitosan monomeric unit molar ratio of 3.8. The polymer was contrasted by means of $UO_2(CH_3COO)_2$ 0.2% w/v. TEM images were acquired at a constant accelerating voltage of 100 kV.

To get further insights about mechanical response by hydrogels, the distribution of chitosan within wall-to-wall systems was studied. By considering the very thin thickness of hydrogels fabricated with the standard method reported in the paragraph 3.2.2.5., a slight modification of protocol was thought in order to increase the cross-section surface. To this purpose, a dialysis tube of 25 mm as diameter was used for the gelation process and the same *r* of 3.8 was maintained. Resulting hydrogels were cut along the gelation axis and ratio between dry/wet weights of slices was calculated. Results are pointed out in Figure 22.

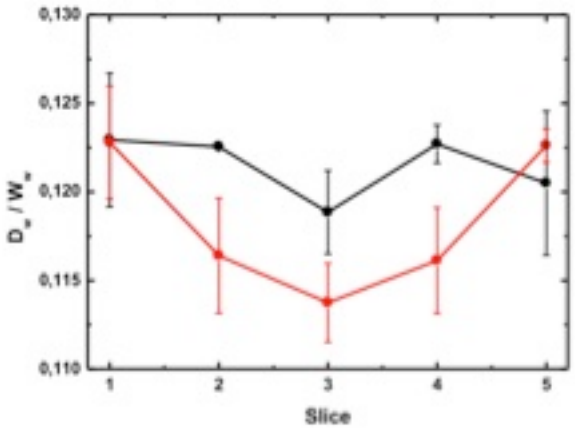

Figure 22. Polymer distribution profile along chitosan-TPP (black solid line) and chitosan-PPi (red solid line) hydrogel cross-section expressed as dry/wet weight ratios of slices (numbered 1-5). Cross-linker/chitosan monomeric unit molar ratio (*r*) was set to 3.8 with comparison purposes to TEM analyses. Data are expressed as mean (± SD) with $n = 2$ and $n = 3$ for TPP and PPi hydrogels, respectively.

Polymer distribution within TPP hydrogels demonstrated to be approximately constant along cylinder axis, albeit with higher experimental error to the boundary. At variance, PPi hydrogels showed a not homogeneous profile of chitosan concentration. More in detail, the concentration of polymer was higher at the boundary compared to that of the core, although continuous matrices were obtained at macroscopic scale. This condition can be ascribed to a partial inhomogeneity occurred during the ionotropic gelation, due to the milder ability of PPi to bind chitosan leading to the formation of a more liquid-like core. As a consequence, mechanical properties of hydrogels reticulated with the same amount of either TPP or PPi are essentially dissimilar as reported in Table 5 with higher shear moduli for the former.

3.2.4. Main conclusions

- Turbidimetry, circular dichroism and ^{1}H-NMR suggested the higher ability of TPP with respect to PPi to interact with chitosan thus inducing chain reconfiguration;
- The ability of PPi giving rise to the formation of wall-to-wall hydrogels with tunable mechanical properties was demonstrated;
- Different mechanical response of TPP/PPi-hydrogels is affected by the distribution of the polysaccharide network within hydrogels.

CHAPTER III

Fabrication and biological properties of chitosan/chitlac-AgNPs membranes for wound healing applications

3.3.1. Aim of work

This section is aimed at exploiting the slow ion diffusion technique discussed in the chapter I for the preparation of macroscopic chitosan hydrogels to obtain soft pliable membranes which include antimicrobial silver nanoparticles (AgNPs) stabilized by a lactose-modified chitosan (chitlac). The rationale of this approach is to enhance the antibacterial properties of chitosan membranes by means of silver nanoparticles without impairing the viability of eukaryotic cells.

3.3.2. Materials and methods

3.3.2.1. Materials. Highly deacetylated chitosan (fraction of *N*-acetyl-glucosamine units - Fa - of 0.16 as determined by means of ^{1}H-NMR), was purchased from Sigma-Aldrich (Chemical Co.). The relative molar mass ("molecular weight", M_w) of chitosan determined by intrinsic viscosity measurements was found to be around 690 kDa.(*162*) Chitlac (lactose-modified chitosan, CAS registry number 85941-43-1) was prepared according to the procedure reported elsewhere starting from highly deacetylated chitosan.(*162*) The composition of chitlac was determined by means of ^{1}H-NMR and resulted to be: glucosamine residue 20%, N-acetylglucosamine 18% and 2-(lactit-1-yl)-glucosamine 62%. The relative M_w of chitlac is around 1.5 x 10^6. Pentasodium tripolyphosphate (TPP), sodium chloride (NaCl), glycerol (ReagentPlus® ≥ 99.0%), silver nitrate ($AgNO_3$), ascorbic acid ($C_6H_8O_6$), MTT formazan powder [1-(4,5-Dimethylthiazol-2-yl)-3,5-diphenylformazan], phenazine methosulfate (PMS) powder and phosphate buffered saline (PBS) were all purchased from Sigma-Aldrich (Chemical Co.). Luria Bertani (LB) broth, LB Agar and Brain Heart Infusion (BHI) broth were from Sigma-Aldrich (Chemical Co.). All other chemicals and reagents were of the highest purity grade commercially available.

3.3.2.2. Chitlac-silver nanoparticles preparation (chitlac-nAg). Although chitlac is able to directly reduce silver ions,(*196*) it was resorted to obtain silver nanoparticles (AgNPs) by reducing Ag^+ ions by means of ascorbic acid in chitlac solution according to the

protocol described elsewhere.(*62*) Briefly, freeze-dried chitlac was dissolved in deionized water to obtain a solution with final concentration 4 g L^{-1}. Chitlac solution was then mixed with $AgNO_3$ solution to achieve a final silver nitrate concentration of 4 mM. Ascorbic acid (reducing agent) solution was added at final concentration of 2 mM. Resulting mixture was held for 4 h at room temperature in dark condition and subsequently stored at 4 °C.

3.3.2.3. Membrane preparation. Membranes were produced by exploiting a controlled freeze-dried process starting from wall-to-wall hydrogels obtained by a slow diffusion technique already described in paragraph 3.1.2.3 with slight modifications. Briefly, a solution composed by chitosan (2% w/v), chitlac-nAg (1.5 g L^{-1} and 1.5 mM as chitlac and silver final concentration, respectively) and glycerol (5% v/v) - "chitlac-nAg gelling solution" - was casted into the same mold described previously. Mixture composed of chitosan (2% w/v), chitlac (1.5 g L^{-1}) and glycerol (5% v/v) was employed for the preparation of membranes without AgNPs. The system was hermetically sealed and immersed into a TPP (1.5% w/v) - NaCl (150 mM) - glycerol (5% v/v) solution (Figure 24B). Ions diffusion proceeded for 24 h under moderate stirring at room temperature allowing hydrogel formation. At the end of dialysis, hydrogels were washed twice in deionized water (1 h for each washing) in order to remove all residual traces of unbound TPP. Thereafter hydrogels were cooled by immersion in a liquid cryostat (circulating bath 28L, VWR, Radnor, PA, U.S.A). Ethylene Glycol in water (3:1) was used as refrigerant fluid. Temperature was decreased from 20 to -20 °C by 5 °C steps with 20 minutes intervals. Samples were then freeze-dried for 24 h. For convenience, resulting membranes are named in overall chapter as M (without AgNPs) and M-Ag (with AgNPs).

3.3.2.4. UV-Vis Spectroscopy. UV-Visible spectroscopy measurements were performed on diluted (1:20) chitlac-nAg gelling solution by means of Cary 400 spectrophotometer. Acetic acid (0.2 M) was used as blank solution and subsequently subtracted to all spectra recorded. The following setup was used throughout the measurements: data interval 1 nm, scan speed 600 nm min^{-1}.

3.3.2.5. Transmission electron microscopy (TEM). TEM images were acquired by a PHILIPS EM 208 Microscope. Diluted (1:50) chitlac-nAg gelling solution was deposited onto Nickel grids coated with a carbon film and dried overnight. Images were recorded at different magnification. Statistical analysis was performed upon 140 silver nanoparticles

randomly selected at 89 kX magnification. The diameter of silver nanoparticles was calculated by ImageJ software.

3.3.2.6. Morphological analyses. Morphological analyses of hydrogels embedding silver nanoparticles and of M-Ag membranes were performed by scanning electron microscopy (Quanta250 SEM, FEI, Oregon, U.S.A) in the same experimental conditions already described in the paragraph 3.1.2.4. In this case the accelerating voltage was kept constant at 30 kV.

3.3.2.7. Swelling studies. Swelling studies of M-Ag membranes were carried out placing samples in 10 mL of PBS (pH 7.4) up to 3 days at 37 °C. At different time intervals (t = 0, 2, 4, 6, 8, 24, 48 and 72 h) membranes were removed from the medium and weighed after blotting the excess of water using filter paper. The swelling ratio was calculated as the percentage of water uptake with respect to the initial weight in agreement with the following formula:

$$Water\ uptake = \frac{W_t - W_0}{W_0} \times 100$$

where W_t is the weight of samples at different time intervals and W_0 the dry weight of membranes at t = 0. All measurements were performed in triplicate.

3.3.2.8. Antimicrobial tests. The antibacterial activity of both M and M-Ag membranes was evaluated using strains of *Escherichia coli* (ATCC® 25922™), *Staphylococcus epidermidis* (ATCC® 12228™), *Staphylococcus aureus* (ATCC® 25923™) and *Pseudomonas aeruginosa* (ATCC® 27853™).

3.3.2.8.1. Growth inhibition assay. Membranes were sterilized (30 minutes of UV-irradiation for each side of sample) and incubated in sterilized PBS for 72 h at 37 °C under shaking condition in order to re-swell the system. Bacterial suspensions were prepared by adding 20 µL of bacteria, preserved in glycerol, to 5 mL of LB broth. The obtained suspensions were incubated overnight at 37 °C. After 24 h, 500 µL of bacterial suspension was diluted in 10 mL of broth and grown up for 90 min at 37 °C in order to restore an exponential growth phase. Bacterial concentration was measured by means of optical

density (O.D.) at 600 nm. The bacterial suspension was then diluted in 10% (v/v) LB broth in PBS to obtain a final concentration of 5 x 10^6 bacteria mL^{-1}. After re-swelling, PBS was removed from membranes and 2 mL of bacterial suspension was added to each one. All bacteria strains were then incubated at 37 °C for 4 h. Tests were carried out in shaking condition (140 rpm) to optimize the contact between bacteria and membranes. At the end of incubation, bacterial suspension was collected and membranes were washed with 2 mL of PBS by vortexing for defined time so as to recover all bacteria. The washing solution was then added to the bacterial suspension previously transferred into a tube. The total collected bacterial solution was serially diluted in PBS (from 10^{-1} to 10^{-5}) and 25 µL of each suspension were plated on LB agar. After overnight incubation at 37 °C, the colony forming units (CFUs) were counted. Outcomes were compared with a suspension of bacteria grown in liquid medium as control. Data are pointed out as the mean of three independent determinations with comparable results.

3.3.2.8.2. Biofilm formation. Bacterial suspensions of *S. aureus* and *P. aeruginosa* were prepared by adding 20 µL of bacteria, preserved in glycerol, to 5 mL of BHI broth *plus* 3% w/v sucrose. The obtained suspensions were incubated overnight at 37 °C. After 24 h, bacteria were diluted 1:100 in the same broth and plated (300 µL/well) into 24-well plates. For confocal laser scanning microscopy analyses, bacteria were plated on sterile 13 mm tissue culture coverslips (Sarstedt, U.S.A.) previously laid down on the bottom of culture plate wells. Plates were incubated at 37 °C for 24 h allowing biofilm formation After 24 h, broth was removed and formed biofilm was carefully rinsed twice with 100 µL of sterile PBS in order to remove non-adherent cells. 300 µL of PBS were then added to each well and circular specimens of swollen membranes were deposited on the bacterial layer. Biofilms treated with membranes were then incubated at 37 °C and MTT assay was performed according to the following protocol after 4 and 24 h of incubation.

3.3.2.8.3. Viable biomass assessment. The test was performed according to the protocol described elsewhere.(*197*) Briefly, MTT stock solution was prepared by dissolving 5 mg mL^{-1} of MTT powder in sterile PBS. PMS stock solution was prepared by dissolving 0.3 mg mL^{-1} of relative powder in sterile PBS. Solutions were further filtered (0.22 µm filters, Biosigma, Italy) and stored at 2 °C in light-proof vials until the day of the experiment, when a fresh measurement solution (FMS) was prepared by mixing 0.5 mL of MTT stock solution, 0.5 mL of PMS stock solution, and 4 mL of sterile PBS. DMSO was used as

lysing solution (LS). After the biofilm incubation period, membranes and PBS were gently removed from the plates and each well was carefully rinsed three times with 100 µL of sterile PBS in order to remove non-adherent cells. 200 µL of FMS solution were placed into each well and the plates were incubated for 3 h under light-proof conditions at 37 °C. The FMS solution was then gently removed and formazan crystals were dissolved by adding 200 µL of LS to each well. Plates were stored for an additional 1 h under light-proof conditions at room temperature and then 80 µL of the solution were transferred into the wells of 96-well plates. The absorbance of the solution was measured using a spectrophotometer (Infinite M200 PRO NanoQuant, Tecan) at a wavelength of 550 nm. Outcomes were expressed as optical density (O.D.) units and are the mean of three independent experiments.

3.3.2.9. Confocal laser scanning microscopy (LSCM). LSCM studies were addressed at detecting viability/death of bacteria grown in the biofilm community. FilmTracer Live/Dead biofilm viability kit (Invitrogen™) was used. Dead cells were stained by propidium iodide, (red fluorescence - λ_{ex} 514 nm; λ_{em} 590 nm) whereas live cells by SYTO® 9 (green fluorescence - λ_{ex} 488 nm; λ_{em} 515 nm). Staining was performed on biofilms grown on coverslips as described above, according to the manufacture's protocol. Images were acquired on a Nikon Eclipse C1si confocal laser scanning microscope with a Nikon Plan Fluor 20X as objective. Resulting stacks of images were analyzed using ImageJ software.

3.3.2.10. Cell culture. Mouse fibroblast-like NIH-3T3 (ATCC® CRL1658) and immortalized human keratinocyte HaCaT (kindly gifted by Dr. Chiara Florio, University of Trieste) cell lines were used for the *in vitro* experiments. Both cell lines were cultured in Dulbecco's Modified Eagle's Medium high glucose (EuroClone, Italy), 10% heat-inactivated fetal bovine serum (Sigma Aldrich, Chemical Co. U.S.A), 100 U mL^{-1} penicillin, 100 µg mL^{-1} streptomycin and 2 mM L-glutamine in a humidified atmosphere of 5% CO_2 at 37 °C.

3.3.2.11. Cytotoxicity evaluation and fluorescence microscopy. *In vitro* cytotoxicity of membranes was evaluated by using MTT assay on both NIH-3T3 and HaCaT cells. UV-sterilized samples of approximately 20 mm in diameter and 1.5 mm in width were placed in Dulbecco's modified Eagle's medium, inactivated fetal bovine serum 10%, penicillin

100 U mL^{-1}, streptomycin 100 µg mL^{-1} and L-glutamine 2 mM for 72 h at 37 °C and 5% pCO_2. After 72 h of incubation, the cytotoxicity test was performed by direct contact of the cells with the swollen membranes. 200 000 cells were plated on 6-well plates and, after complete adhesion, culture medium was changed with 2 mL of fresh medium. Tested materials were directly deposited on the cell layer. After 24 and 72 h, MTT assay was performed according to the manufacture's protocol. As a positive control material, poly(urethane) films containing 0.25% zinc dibuthyldithiocarbamate (ZDBC) (20 mm disks) were used. As negative control material, plastic poly(styrene) sheets (20 mm disks) were used. Each material test was performed in triplicate. Cytotoxicity was expressed as percentage of viability by normalizing the $O.D._{570\ nm}$ of samples to the $O.D._{570\ nm}$ of the negative control. Data are pointed out as the mean of three independent determinations with comparable results.

For fluorescence microscopy analyses, cells were fixed by 4% paraformaldehyde in PBS, permeabilized with 0.1% v/v Triton X-100 and blocked with 1% BSA (15 min at 37 °C). Finally, cells were stained 1 h at 37 °C with Phalloidin-FITC 50 µg mL^{-1} and 1 min with DAPI 0.1 µg mL^{-1} (Sigma-Aldrich, Chemical Co. U.S.A). Photographs were taken with a Nikon Eclipse E600 microscope equipped with a Nikon Coolpix995 digital camera.

3.3.2.12. Statistical analyses. Data are expressed as means and standard deviations (SD). Statistical analyses were performed using Student's t test, and a p value of < 0.05 was considered statistically significant.

3.3.3. Results and discussion

The main goal of this work traced back to the idea of exploiting the ability of two polysaccharides, namely chitosan and chitlac, to form antibacterial and non-cytotoxic hydrophilic membranes to be used as dressing in the treatment of non-healing wounds. In another contribution, the higher ability of chitlac to coordinate and stabilize silver nanoparticles compared to chitosan was demonstrated.(*62*) In chapter I, the novel process that exploits the capability of chitosan to undergo ionotropic gelation in the presence of TPP anions was discussed. Given these premises, the main purpose was to create a chitosan-chitlac-nAg blend capable of gelling in the presence of TPP without affecting the stability and the antibacterial activity of silver nanoparticles.

UV-Vis spectroscopy and TEM investigations were performed to evaluate shape, distribution and dimensions of the nanoparticles. Figure 23A shows the UV-Vis spectra of a diluted chitosan-chitlac-nAg gelling solution pointing out the plasmon resonance band at about 400 nm due to the presence of the AgNPs. The symmetrical shape of this narrow band suggests that nanoparticles are well dispersed and stabilized in the mixture. No significant differences in the UV-Vis spectra were observed after five months of storage at room temperature, indicating a good stability over time.

In order to evaluate nanoparticles shape and dimensions, TEM analyses were carried out. Figures 23B and C display images of nanoparticles in diluted gelling solution at different magnifications, showing good dispersion, lack of aggregates and spherical shape morphology for the majority of nanoparticles. TEM images have been analyzed to evaluate the dimensional distribution of the nanoparticles. The histogram in Figure 23D points out a narrow size distribution scattered with maximum frequency at around 20 nm and a mean diameter of 20.1 ± 8.4 nm.

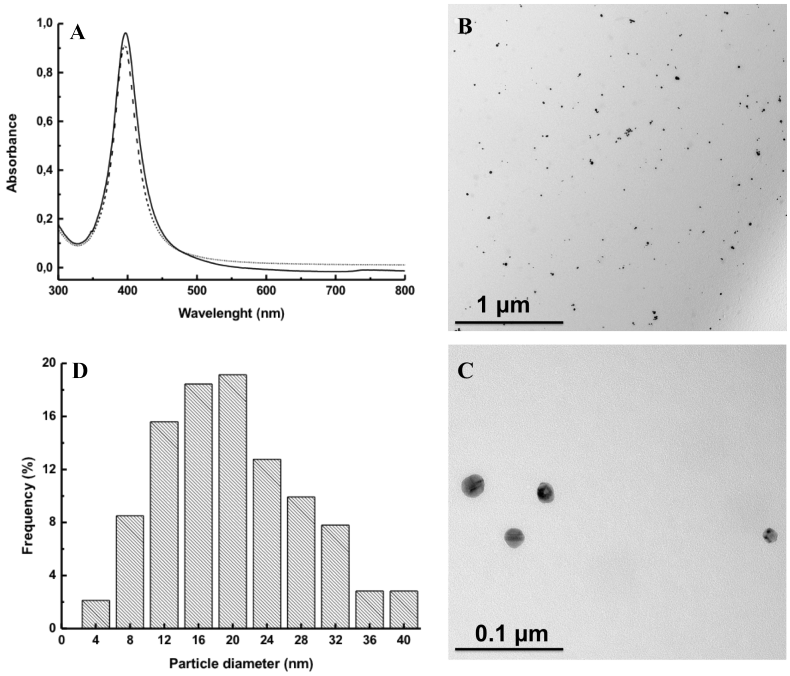

Figure 23. (A) UV-Vis spectra of silver nanoparticles in diluted 1:20 gelling solution (chitosan, chitlac-nAg, glycerol) after one day (solid line) and after five months storage (dashed line). (B-C) TEM images of silver nanoparticles dispersed in diluted 1:50 gelling solution at different magnifications. (D) Silver nanoparticles size distribution based on TEM images and calculated by means of ImageJ software.

Chitlac-nAg was mixed with chitosan (and glycerol) and a homogeneous solution was obtained. A sketch of the interpenetrated polymer network preparation is depicted in Figure 24A, where chitlac and chitosan are represented as worm-like structures whereas silver nanoparticles as red dots. When the chitlac-nAg colloidal dispersion and chitosan solution were mixed at investigated concentrations, no aggregates or precipitates were observed, thus suggesting the completely miscibility of the two polysaccharides. TEM analyses demonstrated the presence of small, round-shaped and mono-dispersed nanoparticles (Figures 23B, C). This result was supported by UV-Vis measurements where the presence of very narrow and symmetrical bands confirmed the good dispersion of nanoparticles. This finding clearly suggests that the presence of chitosan-glycerol did not negatively affect the stability of silver nanoparticles coordinated by chitlac.

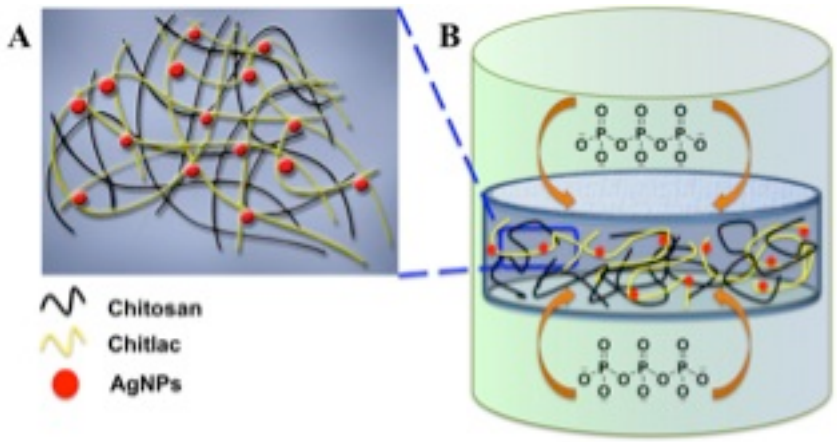

Figure 24. (A) Entangled distribution of chitosan (black ribbons), chitlac (yellow ribbons) and AgNPs (red dots) in gelling solution. (B) Slow ion diffusion technique: a vessel containing the viscous gelling solution is placed into an outer solution [TPP (1.5% w/v) - NaCl (150 mM) - glycerol (5% v/v)] under stirring. When the dialysis starts, TPP ions diffuse through the semipermeable walls (membranes) of the vessel so as to favor a controlled ionotropic gelation.

The mixture was then confined in dialysis membranes by means of a custom-made vessel immersed in a TPP solution (Figure 24B). This technique enabled to turn the chitlac-nAg gelling solution into a macroscopic homogenous hydrogel, exploiting the slow TPP diffusion through the dialysis membranes. Chitlac-nAg did not prove to hamper the ionotropic gelation of chitosan, which resulted in homogeneous hydrogels and membranes as confirmed by SEM investigation (Figures 25A-F). Indeed, E-SEM images pointed out the continuous polymeric network both at the surface and at the cross-section of the

hydrogel (Figure 25B,C). Since the primary purpose of the present work was to produce dried pliable membranes, nanocomposite hydrogels were freeze-dried according to a procedure previously described. Resulting membranes (Figure 25D) were analyzed by SEM analyses that revealed the compact polymeric mesh of the material (Figure 25E,F).

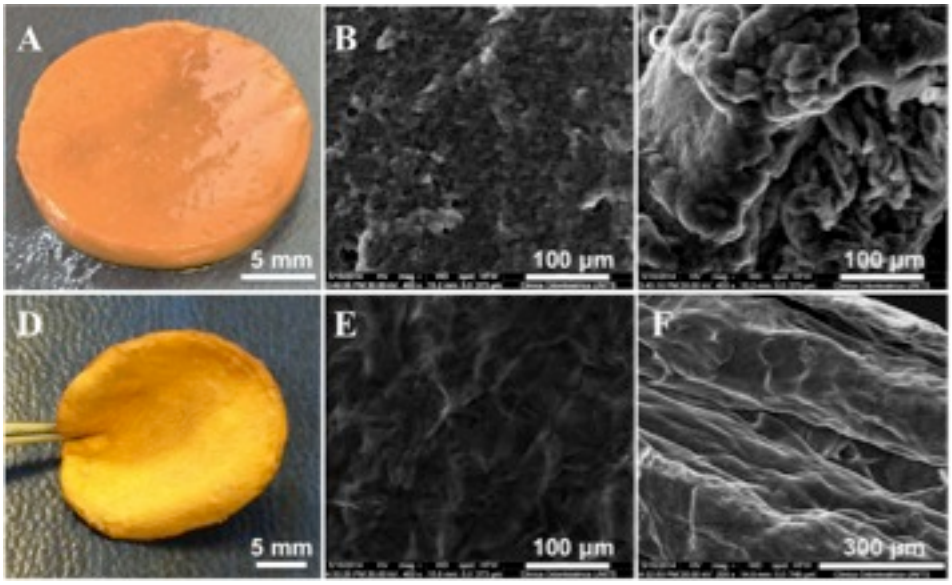

Figure 25. Upper row: hydrogel embedding AgNPs. (A) Top view, (B) E-SEM micrograph of the hydrogel surface, (C) E-SEM micrograph of the hydrogel cross-section. Lower row: dried membrane derived from the hydrogel depicted in (A) by freeze-drying. (D) Top view, (E) SEM micrograph of the membrane surface, (F) SEM micrograph of the membrane cross-section.

An ideal wound dressing should offer protection from infections, should remove wound exudates (maintaining at the same time a moist environment) and should demonstrate lack of cytotoxicity towards eukaryotic cells to not interfere with tissue regeneration.(*123*) According to these requirements, several studies were aimed at assessing the antibacterial properties of membranes, their swelling behavior and the biocompatibility towards eukaryotic cells. Antibacterial features of membranes were evaluated towards both $Gram^-$ and $Gram^+$ bacteria strains. Anti-bacterial tests were carried out on *E. coli*, a typical bacterium employed in laboratory to assess the efficacy of antimicrobial agents and antibiotics, *S. epidermidis* which belongs to microbiota of the skin and finally *P. aeruginosa* and *S. aureus* because of their ability to produce biofilm in chronic wounds.(*29*)

Experiments were addressed to assess the bacterial growth inhibition and biofilm eradication activities of the membranes with AgNPs (M-Ag) in comparison with the membranes without AgNPs (M). Figures 26A,B show the results obtained by a growth inhibition assay with *E. coli* and *S. aureus*. For both strains, a significant drop of CFU ($p < 0.001$) was identified for both M- and M-Ag-treated samples in comparison with control (suspension of bacteria grown in medium).

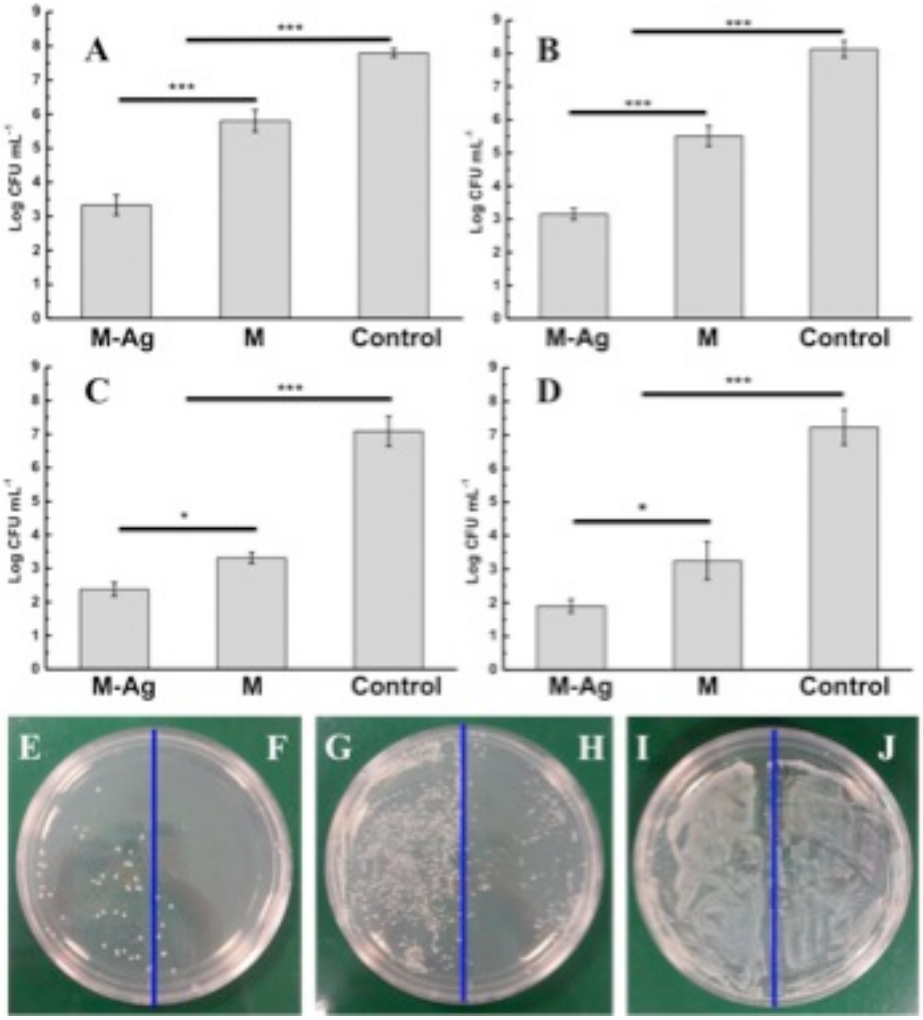

Figure 26. Growth inhibition rate expressed as Log CFU mL^{-1} of *E. coli* (A), *S. aureus* (B) and *P. aeruginosa* (C) following 4 h of treatment with M-Ag (with AgNPs) and M (without AgNPs) membranes. Growth inhibition rate of *S. epidermidis* (D) following 20 h of treatment with the same membranes. Statistical differences were determined by means of Student's t test. *$p < 0.05$; **$p < 0.01$; ***$p < 0.001$. *E. coli* colonies on LB agar: not diluted (E) and diluted 10^{-1} (F) M-Ag-treated sample; not diluted (G) and diluted 10^{-1} (H) M-treated sample; not diluted (I) and diluted 10^{-1} (J) control sample.

M membranes exert mainly a bacteriostatic effect which can be ascribed to the presence of chitosan. Indeed, the number of bacteria after four hours remains basically constant when compared with the amount of bacteria seeded at time zero (5 x 10^6 bacteria mL^{-1}). At variance, M-Ag membranes showed a marked antibacterial activity in comparison with M ones ($p < 0.001$) owing to the presence of embedded AgNPs. This finding is confirmed by visual observations as reported in Figures 26E-J that show the growth of *E. coli* colonies on LB agar for treated and untreated samples. A similar trend was observed for *P. aeruginosa* (Figure 26C) where a drop of around 5 Log was found for M-Ag-treated samples. Also in this case, the presence of AgNPs in M-Ag membranes enables to significantly increase ($p < 0.05$) the antibacterial properties of such membranes with respect to M ones. In the case of *S. epidermidis*, no significant differences were revealed between M and M-Ag after 4 h of treatment, although a marked antibacterial activity (3 Log CFU drop) was detected for both of them compared with the control (not shown). In order to spot significant differences between M and M-Ag membranes with this strain, time of incubation was increased up to 20 h so as to extend the exposure time of bacteria to membranes. In these conditions, the Log CFU mL^{-1} calculated for M-Ag and M membranes were 1.9 ± 0.2 and 3.3 ± 0.6, respectively ($p < 0.05$, $n = 3$), thus indicating an enhanced activity in the presence of AgNPs (Figure 26D).

After demonstrating that M-Ag membranes possess the capability to significantly impair the growth of different bacteria strains, the following step was to verify the activity of such membranes upon mature biofilms. Figures 27A,B pointed out the results obtained after 4 and 24 h of treatment for *S. aureus* and *P. aeruginosa* biofilms, respectively. In the case of the $Gram^+$ strain, it was revealed that M-Ag membranes were effective in breaking apart the biofilm, as revealed by MTT colorimetric assay where samples treated with membranes embedding AgNPs showed a reduction of ~ 75% of O.D. after only 4 h with respect to control (Figure 27A). Conversely, M membranes did not impair biofilm viability in the same timeframe. At longer time (24 h of treatment), M membranes displayed an antibacterial activity towards *S. aureus* biofilm, in any case milder than in the presence of AgNPs (M-Ag). These results were confirmed by analysis of the biofilms with confocal laser scanning microscopy (Figure 27C-E). In Figure 27E *S. aureus* biofilm appears as a green fluorescent layer, which indicates the good bacteria viability in the case of the growth control. Conversely, cells treated for 24 h with M-Ag membranes pointed out mainly red fluorescent bacteria and only a few green cells, thus suggesting cell membrane damage and the consequent entry of propidium iodide into dead cells (Figure 27D).

Moreover, the bacteria layer appeared non-homogeneous and broken apart. Biofilms treated with M membranes showed a partial disaggregation of the bacteria layer after 24 h of treatment, as pointed out by sagittal YZ projection, albeit a higher number of viable cells with respect to M-Ag-treated biofilm was detected (Figure 27C). These findings are in agreement with what measured in the viable biomass experiments above discussed. Viable biomass assessment was also carried out on *P. aeruginosa* as shown in Figure 27B. In this case, by comparing M and M-Ag membranes no statistical differences were observed at investigated times, even if a O.D. decrease was measured for both in comparison with the control group.

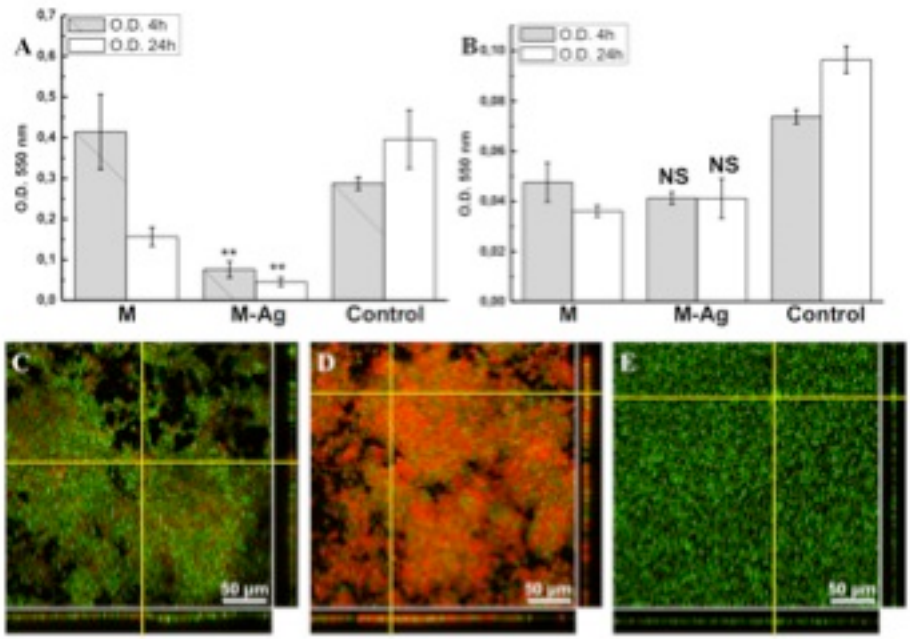

Figure 27. Viable biomass MTT assay expressed as O.D. at 550 nm of *S. aureus* (A) and *P. aeruginosa* (B) following 4 and 24 h of treatment with M-Ag (with AgNPs) and M (without AgNPs) membranes. Statistical differences were determined by means of Student's t test. NS: no statistical differences versus M; $^{**}p < 0.01$ *versus* M. LSCM images of *S. aureus* biofilm: M-treated sample after 24 h (C), M-Ag 24 h-treated sample (D) and control (E). For all images green fluorescence indicates live cells whereas red fluorescence refers to dead ones. Horizontal sagittal sections: XZ projections; vertical sagittal sections: YZ projections.

Considering that chitlac is devoid of antibacterial properties,(*56*) the synergistic effect on bacteria killing of AgNPs when combined with chitosan after already 4 h of contact was proved. In the case of *S. epidermidis*, statistical differences between M-Ag and M

membranes started to be evident only after longer times (20 h). The higher resistance of this strain in presence of silver nanoparticles is consistent with another work.(*77*) The studies on mature biofilms pointed out that both membranes are able to break apart *S. aureus* biofilm after 24 h of treatment, as demonstrated by LSCM analyses (Figures 27C,D). While M membranes are supposed to exert antibacterial activity owing to the properties of chitosan (electrostatic, hydrophobic and chelating effects(*148*)), M-Ag membranes also exploit the presence of silver nanoparticles to boost the bactericidal efficacy. This is confirmed by the rapid O.D. reduction already after 4 h of treatment in the case of *S. aureus* (Figure 27A). It is very important to notice that LSCM images were acquired after removing membranes from the bacteria biofilm. Indeed, given that AgNPs have previously proved to exert their antibacterial activity by interaction with bacterial membranes,(*62*),(*67*) in the present system AgNPs grafted on the surface of M-Ag membranes are supposed to interact with bacteria cells in correspondence to molecular target, *e.g.* thiol groups (-SH) of proteins, causing membrane damage.(*67*),(*68*) The bactericidal effect of silver in this system can be also ascribed to the small dimensions of the nanoparticles (20.1 ± 8.4 nm), which ensures a high surface area of contact with bacteria membranes.(*66*)

Tridimensional systems based on polysaccharide networks can prevent nanoparticles from being available for eukaryotic cellular uptake but, at the same time, preserve their antimicrobial activity allowing the direct interaction of the nanoparticles with the proteins localized on the bacterial surface.(*62*) In fact, in bacteria the thiol groups (-SH) of membrane proteins, main molecular targets of the silver antibacterial activity, are exposed to the extracellular portion of the membrane as discussed above. Conversely to prokaryotic cells, eukaryotic cells do not have exterior (-SH) groups at membrane level.(*56*) As a result, AgNPs are unable to interact with them except if internalized. Indeed, recently Lee *et al*. proved that AgNPs were potentially cytotoxic towards NIH-3T3 cells when they were taken up, thus favoring changes of morphology, oxidative stress, induction of reactive oxygen species, up-regulation of Heme oxygenase 1 expression, apoptosis and autophagy.(*72*)

In order to assess the biocompatibility of M-Ag membranes for dermatological applications, MTT assay was performed on keratinocytes (HaCaT) and fibroblasts (NIH-3T3) cell lines and results are pointed out in Figure 28. HaCaT and NIH-3T3 cell lines were chosen because they are cellular components of skin and because of their large use as model to evaluate the response of biological systems towards biopolymer networks.(*198*)

M membranes were tested as chitosan-based control without AgNPs. The plot in Figure 28A shows that the viability of treated HaCaT cells was not influenced when membranes are in direct contact with cells. No statistical differences were identified for M-Ag samples compared to the negative control at time investigated, thus suggesting lack of cytotoxicity of the material. This outcome is consistent with what observed by optical microscopy (Figure 28C), where cells showed a normal keratinocyte-like morphology, good spreading, and absence of suffering signals such as cytoplasmic vacuoles, chromatin aggregation, or formation of cellular debris. Fluorescence microscopy (Figure 28D) confirmed the viability of treated cells showing an optimal distribution of cytoskeleton (Phalloidin-FITC staining) and intact nuclei (DAPI staining). Similar results were obtained with NIH-3T3 cell line as shown in Figure 28B. Also in this case the MTT assay did not point out any significant difference between treated samples *versus* negative control and optical/fluorescence microscopy confirmed the viability of cells (Figures 28E,F).

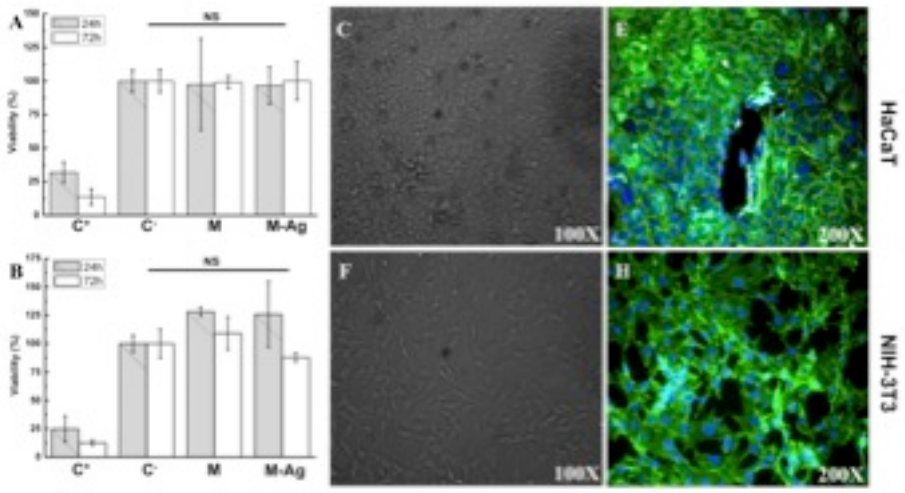

Figure 28. Percentage of viability of keratinocytes HaCaT (A) and fibroblast NIH-3T3 (B) cells measured using MTT assay. M-Ag (with AgNPs) and M (without AgNPs) membranes were kept in touch with cells and test was performed after 24 and 72 h of treatment. Poly(urethane) sheets containing 0.25% zinc dibuthyldithiocarbamate were used as contact positive control (C^+) whereas plastic poly(styrene) sheets were used as contact negative control (C^-). Statistical differences were determined by means of Student's t test NS: no statistical differences between C^- and M-Ag both at 24 and 72 h of treatment. Optical microscopy of HaCaT (C) and NIH-3T3 (E) cell lines after 72 h of treatment with M-Ag membrane. Fluorescence microscopy of HaCaT (D) and NIH-3T3 (F) cell lines: cytoskeleton was stained by means of Phalloidin-FITC (P-FITC) whereas nuclei by DAPI. Images were acquired after 72 h of contact with M-Ag membranes.

Thanks to lack of morphological alterations and cellular debris in this model, as pointed out by optical and fluorescence microscopy, a massive cellular uptake of silver nanoparticles may be excluded, thus concluding AgNPs are firmly grafted and immobilized in the chitlac/chitosan polymeric network and therefore do not diffuse into the surrounding environment.

Finally, water uptake is particularly important for an ideal wound dressing because it enables to eliminate exudates from an infected lesion thus hampering bacteria spread. To study the hydrophilicity of membranes, swelling studies were carried out and results are shown in Figure 29.

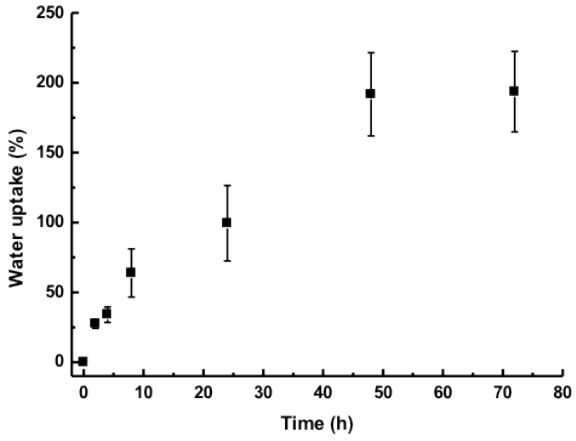

Figure 29. Water uptake (%) versus time (h) of M-Ag membranes immersed in PBS buffer (pH 7.4) at 37 °C. The data are expressed as mean (±SD, $n = 3$).

Membranes demonstrated a complete swelling state in PBS buffer at 37 °C after 72 h of soaking. The plot displays a slow, albeit constant, water uptake by membranes that took place in the first 4 h. Furthermore, the water uptake increased from 34.1 ± 5.6 to 191.7 ± 29.8% after 48 h of soaking because of diffusion of water molecules into the hydrophilic polymeric network. As a result, membranes reached the equilibrium and the swelling rate did not vary significantly after 72 h (193.6 ± 28.8% as final water uptake). What observed is in agreement with Silva *et al*. that demonstrated a similar water uptake in the case of tridimensional constructs based on chitosan.(*199*)

3.3.4. Main conclusions

- A silver-containing antimicrobial membrane was successfully fabricated;
- The stability of chitlac-coordinated AgNPs was not affected by mixture with chitosan and glycerol;
- This nanocomposite material was proved to possess antimicrobial activity towards bacteria suspensions and mature biofilms and lack of cytotoxicity.

CHAPTER IV

Chitosan-hyaluronan nanoparticles (complexes)

3.4.1. Aim of work

The work presented in this chapter was primarily aimed at verifying the anti-inflammatory properties of butyrate upon two inflammatory cell models. Macrophages and neutrophils were considered because of their different involvement in the inflammation phase. The effect of butyrate on cytokine production by macrophages and on neutrophils respiratory burst was studied. As the anti-inflammatory activity of butyrate *versus* human neutrophils was demonstrated to be time-dependent, chitosan (CH)/hyaluronan (HA)-based nanoparticles (complexes) able to host butyrate (B-NPs) as payload were fabricated. The goal was to provide over time to the cells a constant supply of cargo.

The final target of this investigation is addressed: (*i*) to load B-NPs within the chitosan membranes described in the previous chapters for non-healing wounds applications, (*ii*) to use B-NPs alone for the treatment of inflammatory bowel diseases exploiting their mucoadhesive properties.

3.4.2. Materials and methods

3.4.2.1. Materials. The characteristics of the hydrochloride chitosans (kindly gifted by Prof. Kjell Morten Vårum, NTNU, Trondheim, Norway) used in this study are presented in Table 6.

Chitosan (Fa)	$[\eta]$ mL g^{-1}	M_w (kDa)	M_n (kDa)	PI (M_w/M_n)
< 0.008	480	183	65	2.82
0.64	300	112	61	1.84

Table 6. Features of chitosans used in the study. The intrinsic viscosity [η] was calculated by means of viscosimetry. The molecular weights (M_w, M_n) and polydispersity index (PI) were analyzed by SEC-MALLS. The fraction of acetylated units (Fa) was determined by ^{1}H-NMR.

The acetylation degree (Fa) was determined by means of ^{1}H-NMR whereas the polydispersity index (PI) and molecular weights (M_w and M_n) were analyzed by size-exclusion chromatography with a multiangle laser light scattering detector (SEC-MALLS).

The intrinsic viscosity was determined by viscosimetry analyses. Sodium Hyaluronate (M_w 180 kDa) was kindly provided by Sigea Srl, Padriciano (Trieste). Sodium tripolyphosphate pentabasic - $Na_5P_3O_{10}$ - (TPP ≥ 98%), sodium butyrate (NaBut 98%), Percoll, bovine serum albumin (BSA, ≥ 96% cell culture-tested), cytochrome *c* (type VI from horse heart), phorbol 12-myristate 13-acetate (PMA), N-formyl-L-methionyl-L-leucyl-L-phenylalanine (fMLP), xanthine/xanthine oxidase (from bovine milk), superoxide dismutase (SOD, from bovine erythrocytes) and lipopolysaccharides (LPS, from *E. coli*, suitable for cell culture) were purchased from Sigma-Aldrich Co. (St. Louis, MO). Fibronectin (FN), from human plasma, was from Roche Diagnostics GmbH (Penzberg, Germany). Human recombinant tumor necrosis factor-α (TNF-α, from yeast) was obtained from MiltenyiBiotec GmbH (BergischGladbach, Germany). High-purity Trypan Blue (TB, Color Index 23850) was obtained from Merck KgaA (Darmstadt, Germany), dissolved in distilled water at 5 mg mL^{-1} and filtered through a Millipore filter to remove non-solubilized material. All other reagents and chemicals were of the highest purity grade available. All solutions were made in endotoxin-free water or physiologic saline (0.9% NaCl) for clinical use.

3.4.2.2. U937: cell culture, differentiation, and induction of cytokine release. U937 human monocytic cells (Sigma) were cultured in RPMI 1640 medium with stable L-glutamine (2 mmol L^{-1}) (EuroClone, MI, Italy), supplemented with penicillin (100 U mL^{-1}), streptomycin (100 U mL^{-1}) and 10% fetal bovine serum. Cells were maintained under humidified atmosphere with 5% CO_2 at 37 °C. Differentiation of U937 cells into adherent macrophages was induced with PMA. Briefly, cell suspensions were centrifuged, resuspended in fresh complete medium and cell viability (> 95%) was assessed by trypan-blue dye exclusion. 1.5 x 10^5 cells were then seeded into each well of a 24-well plate in 0.5 mL as final volume of complete RPMI. Cells were cultured in the presence of 15 ng mL^{-1} PMA for 72 h and further grown for 24 h in fresh complete medium to allow cell recovery. Cells were then incubated for 24 h with butyrate in fresh complete medium before LPS stimulation (1 ng mL^{-1} as final concentration). Cell-free supernatants were collected and stored at -20 °C until measurements of cytokines. TNF-α, IL-1β and IL-6 in the culture supernatants were measured using commercially available ELISA kits (Invitrogen™, Life Technologies, Thermo Fisher Scientifics).

3.4.2.3. Neutrophil isolation. Institutional ethics committee approval was obtained and written informed consent was signed by healthy volunteers from which venous blood was

withdrawn. Neutrophils were isolated by a discontinuous Percoll gradient centrifugation, as described previously in (*200*) and suspended in Ca^{2+}- and Mg^{2+}-free PBS solution, pH 7.4, containing 5 mM glucose and 0.2% w/v BSA.

3.4.2.4. Preparation of FN-coated surfaces. Flat-bottom poly(styrene) wells (F16 MaxiSorp Nunc-Immuno^{TM} Modules, ThermoFisher Scientific Inc., Waltham, MA) or Falcon culture slides (8 chamber poly(styrene) vessel tissue culture treated glass slide, Becton Dickinson and Co., Franklin Lakes, NJ) were coated with FN as described elsewhere.(*201*) Briefly, 50 or 150 μL of FN solution (20 μg mL^{-1} in PBS) were put in each well or chamber, and the plate or the slide was left at 37 °C for 1-2 h in a humidified chamber. Just before use, the wells or slides were rinsed three times with PBS.

3.4.2.5. Assay of O_2^- production. O_2^- production was measured by the SOD-inhibitable cytochrome *c* reduction assay, as previously described.(*202*) Briefly, freshly isolated neutrophils were suspended at 3.75 x 10^6 cells mL^{-1} in PBS-BSA and prewarmed for 30 min at 37 °C in a shaking water bath to restore basal conditions. Five to ten minutes before starting the assay, the cell suspension was supplemented with 1 mM of $CaCl_2$ and 1 mM of $MgCl_2$. Aliquots (20 μL) were then added to FN-coated wells containing cytochrome *c* (0.12 mM as final concentration) and butyrate in a total volume of 0.16 mL PBS-BSA supplemented with 1 mM $CaCl_2$ and 1 mM $MgCl_2$ (Ca^{2+}/Mg^{2+} PBS-BSA). Immediately after the addition of the cells, 20 μL of TNF (10 ng mL^{-1} final concentration) or fMLP (5 μM final concentration) were pipetted in each well. The plate was then transferred in a thermostated microplate reader (MultiskanMCC/340; LabsystemOy, Helsinki, Finland) and readings were taken at intervals of 2.5 minutes for one hour. The amount of reduced cytochrome *c* was calculated from the absorbance difference between 550 nm and 540 nm, using an absorbance of 0.037 optical density (OD) units for 1 nmol reduced cytochrome *c* as a standard.

3.4.2.6. Measurement of adhesion. The number of neutrophils adherent to FN was assessed in the same wells in which O_2^- release had been measured as described elsewhere.(*200*) At the end of incubation, wells were filled with PBS, sealed with 8-cap strips and centrifuged upside-down for 5 min at 200 × *g* to remove non-adherent cells. The wells were then flicked empty and the adherent cells were quantified by measuring myeloperoxidase activity. Standards with known cell numbers were run in parallel for a

quantitative determination of adherent cells.

3.4.2.7. Preparation of blank nanoparticles (NPs) and butyrate-loaded nanoparticles (B-NPs). CH-HA-nanoparticles were fabricated by exploiting the protocol reported in (*203*) with slight modifications. Chitosan (0.6 mg mL^{-1}) and hyaluronan (1.25 mg mL^{-1}) solutions were prepared by solubilizing the polymers in deionized water. After the complete dissolution, both solutions were filtered (0.22 μm filters, Biosigma, Italy) and stored at room temperature prior the use. Plain NPs were fabricated from the addition of 100 μL of TPP solution (0.5 mg mL^{-1} dispersed in deionized water) to 2 mL of filtered HA mixture under stirring condition. Resulting solution (0.5 mL) was then gently added dropwise to 0.5, 1 and 2 mL of CS solution, respectively, in order to vary the HA/CH weight ratio. The formation of NPs occurred within 10 min of stirring. Resulting mixtures were then held at room temperature for 30 min so as allowing their stabilization. For the preparation of B-NPs, sodium butyrate was solubilized in deionized water so as to obtain three solutions with different concentrations (135, 13.5 and 1.35 mM). 80, 120, 200 μL of each butyrate solution were mixed with 0.5, 1 and 2 mL of CS solution, respectively, under stirring. The formation of B-NPs occurred in the same experimental conditions above discussed. The final butyrate concentration in B-NPs solutions was of 10, 1 and 0.1 mM.

3.4.2.8. Physical-chemical characterization of NPs and B-NPs. The size of both NPs and B-NPs was determined using Dynamic Light Scattering (DLS) on a Zetasizer Nano ZS (Malvern Instruments). Measurements were performed in deionized water at a temperature of 25 °C. The size is expressed as the Z-average hydrodynamic diameter obtained by a cumulative analysis of the correlation function using the viscosity and refractive index of water in the calculations. ζ-potential values were obtained by using the technique of laser doppler velocimetry. All the samples were diluted with deionized water (1:10) to adequate scattering intensity prior to the measurements.

Images of NPs were acquired by TEM. NPs were contrasted for ten minutes using $UO_2(CH_3COO)_2$ 1% w/v, diluted 1:10 in deionized water and gently deposited onto copper grids. Visual analysis and image record were performed using a PHILIPS EM Transmission Electron Microscope.

3.4.2.9. Fluorescent labelling of HA. Sodium hyaluronate was labeled using Fluoresceinamine isomer I - green fluorescence (Sigma Aldrich, Chemical Co.) by

exploiting the NHS-EDC reaction. HA was solubilized in MES buffer (50 mM, pH 5.5) with a final concentration of 3 mg mL^{-1}. Ethanol absolute 3.33 mL, NHS (43.3 mg) and EDC (71.6 mg) were progressively added into the HA mixture (30 mL) under stirring. Finally, 346 µL of fluoresceinamine solution (5 mg mL^{-1} ethanol as solvent) was added dropwise to HA mixture and the reaction was let occur in dark condition and room temperature overnight. By using this procedure 1 out of 50 repetitive units were labeled. The resulting solution was sealed in a dialysis bag (cutoff 12 kDa) and extensively dialyzed against $NaHCO_3$ 50 mM firstly and deionized water afterwards. The complete lack of free dye was confirmed by means of fluorescence spectroscopy. The pH of the resulting dialyzed mixture has been adjusted in the range 6.8 - 7.4. The labeled-polymer was finally freeze-dried and stored at 4 °C.

3.4.2.10. Evaluation of B-NPs stability. The stability of B-NPs was assessed in deionized water and in PBS buffer (pH 7.4 and physiological ionic strength). The formulations were diluted 1:10 either in deionized water or in PBS and stored at 37 °C. The stability was determined by evaluating the dimensions of nanoparticles over time up to three days. At time investigated, B-NPs were analyzed by dynamic light scattering (DLS) in the same experimental conditions above reported.

3.4.2.11. Encapsulation efficiency. To evaluate the encapsulation efficiency of butyrate, B-NPs were centrifuged (3000 × *g*; 10 min; 20 °C) and the un-encapsulated butyrate was recovered from the supernatant. Encapsulation efficiency was calculated as ((A x B) - (C x D) / (A x B)) x 100 where A and C are the concentrations of butyrate before and after the centrifugation, respectively, whereas B and D are the total suspension volume before centrifugation and the supernatant volume recovered after centrifugation, respectively. Butyrate supernatants were analyzed by means of mass spectrometry in ESI-mode on a Waters XevoTQ-S instrument coupled to an I-Class UPLC in SIR (single ion recording). The SIR ion was set to m/z 87.0972. UPLC was run isocratic using 30% water + 0.025 mM NH_3OH as mobile phase A and 70% ACN + 0.025 mM NH_3OH as mobile phase B on a Waters BEH HILIC 1.7 µm x 2.0 µm 100 mm column. A mixture of 10% ACN/90% water + 0.1% FA was used as wash and purge solvent. Flow rate was set to 0.150 mL min^{-1} and column temperature to 40 °C. Injection volume was in the range 2-10 µL. Total run time 2.5 min per sample. Capillary voltage was set to 2.5 kV, desolvation temperature 500 °C, desolvation gas flow 1000 L hr^{-1} and cone voltage 20 kV. Dwell time set to 0.15 s, adjusted

to get a minimum of 15 data points across the peak. Standard curves (R^2 > 0.99) were performed with known amount of butyrate and run in parallel.

3.4.2.12. Cell interaction and internalization of NPs. The interaction of NPs with neutrophils and their cell internalization was verified by means of flow cytometry. Flow cytometric analysis of neutrophils incubated with fluorescence-labeled NPs was conducted according to the method described by Busetto *et al*. with slight modifications.(*204*) Neutrophils, suspended at 2.5 × 10^6 mL^{-1} in Ca^{2+}/Mg^{2+} PBS - 0.05% BSA, were incubated at 37 °C in a shaking water bath with fluoresceinamine-isomer I-labeled NPs, in the presence of 10 ng mL^{-1} of TNF. At selected times, 250 μL (aliquots of the incubation mixtures) were withdrawn into the tubes used for flow cytometry analysis and put on ice. Some samples were washed twice with Ca^{2+}/Mg^{2+} PBS - 0.05% BSA (centrifugation at 1000 × *g* for 5 minutes) and resuspended in 250 μL of the same medium prior to the cooling step. Immediately before the analysis, samples were diluted with an equal volume of TB (75 μg mL^{-1}) dissolved in ice-cold 0.1 M citrate buffer, pH 4. After 1 min of incubation on ice, the samples were analyzed. Flow cytometry was performed with a FACScalibur (Becton Dickinson) equipped with an air-cooled 15-mW Argon-ion laser, operating at 488 nm. Fluoresceinamine green fluorescence (FL1) was collected using a 530 ± 30 band pass filter; red fluorescence emitted from TB bound to fluoresceinamine-isomer 1-labeled NP (FL3) was collected by using a 650 ± 13 bandpass filter. The data were collected using linear amplification for FSC and SSC, and logarithmic amplification for FL1 and FL3. For each sample 10 000 events were collected and analyzed by using CellQuest software from Becton Dickinson. Neutrophil population was identified by combined measurement of FSC and SSC and gated in R1 region. The percentage distribution of neutrophil subsets was calculated from dot plot analysis (FL-1 *vs*. FL-3) of R1-gated events.

3.4.2.13. Evaluation of O_2^- scavenging activity of NPs. The scavenging effect of NPs was investigated using the xanthine/xanthine oxidase system. Superoxide generation by the xanthine/xanthine oxidase system was measured by a cytochrome *c* reduction assay as previously described with slight modifications.(*205*) Xanthine (0.05 mM final concentration), cytochrome *c* (0.02 mM final concentration) and, when needed, NPs, chitosan, HA or butyrate were added to microplate wells and the reaction was started by the addition of xanthine oxidase (0.0025 U mL^{-1} as final concentration) to reach the final

volume of 200 µL of PBS. Final concentration of SOD, added as positive control, was 2.5 µg mL^{-1}. The plate was incubated at 37 °C in a thermostated microplate reader and readings were taken at 550 nm and 540 nm at the selected times.

3.4.2.14. *In vitro* release studies. The leakage of butyrate from B-NPs was studied in PBS buffer at 37 °C in order to mimic a physiological milieu. 0.1 mL of PBS 10X was added to 0.9 mL of B-NPs suspension in order to equilibrate the physiological ionic strength. Resulting dispersions were sealed in a dialysis tube (Sigma Aldrich, cutoff 12 kDa) and flooded in 2 mL of PBS dialysis solution under both dynamic (140 rpm) and static conditions. The PBS dialysis solution was replaced with fresh medium at time investigated in order to simulate infinite sink conditions. The amount of released butyrate was assessed by mass spectrometry in ESI-mode. In order to eliminate the salts from the buffer, butyrate samples were derivatized using the *ortho*-benzylhydroxylamine (o-BHA) and *N*-(3-Dimethylaminopropyl)-*N*′-ethylcarbodiimide hydrochloride (EDAC) protocol reported elsewhere(*206*) with slight modifications. The solvent for o-BHA and EDAC was prepared mixing 675 µL of HCl (12 M), 1.1 mL of pyridine and 11 mL of deionized water. 160 mg mL^{-1} o-BHA and 196 mg mL^{-1} EDAC were dissolved yielding a 1 M solution. Derivatization reagents have been made fresh for each analysis. Once the derivatization reagent was ready, UPLC analyses were performed: 20 µL of the samples/standards were added to a 1 mL tube, 50 µL of the o-BHA solution and then 50 µL of the EDAC solution were added to each tube and kept at room temperature for 45 minutes. 300 µL of Ethyl Acetate were added and subsequently vortexed for roughly 5 seconds. 100 µL of the top layer were removed and transferred to an HPLC vial, which was speedvaced for 20 minutes at 45 °C in order to remove the ethyl acetate. Resulting solution was re-dissolved in 400 µL of MetOH/water (1/1) directly in HPLC vial and 5 µL were then injected into the UPLC-MS. The leakage of the fatty acid from B-NPs was monitored up to three days and results are reported as the percentage of the cumulative release on time.

3.4.2.15. Biocompatibility studies. AlamarBlue assay was performed on NIH-3T3 cells in order to evaluate the effects of the nanoparticles on proliferation. All reagents for the preparation of nanoparticles were solubilized using sterile deionized water and resulting solutions were then filtered by 0.22 µm filters. All steps were performed in sterile conditions. 100 µL of cell suspension (2500 cells/well) were plated in a 96-well plates. Plates were finally incubated at 37 °C for 24 h allowing the attachment of cells. After that,

cells were rinsed with PBS 1X and treated with B-NPs with a final concentration of 0.5 mg mL^{-1} and 0.1 mg mL^{-1}. Untreated cells were considered as control. At selected times, the medium was removed and 130 µL of Alamar Blue (1:10 in the same medium) added and the plate incubated. After 4 hours of incubation at 37 °C, 100 µL of the Alamar Blue medium were transferred into a black multiwell plate; a blank constituted of only the Alamar Blue medium was included. Fluorescence (λ_{ex} 544 nm; λ_{em} 590 nm) was measured using FLUOStar Omega-BMG Labtech spectrofluorometer. Results are normalized with respect to Day 0.

3.4.2.16. NPs uptake in chitosan membrane. Chitosan membranes were fabricated as described in the Chapter I (see 3.1.2.3. paragraph). At the end of freeze-drying process, resulting membranes were cut in three pieces, weighed and incubated with a final volume of 1 mL containing fluorescence-labeled NPs (0.4 mL NPs suspension + 0.6 mL deionized water). Incubation proceeded for 24 h at room temperature and in dark conditions. At the end of incubation, membrane pieces were removed from the medium and the fluorescence was measured (λ_{ex} 485 nm; λ_{em} 520 nm) on the same medium. The percentage of NPs uptake has been calculated according to:

$$Uptake\ (\%) = \frac{V_0\ F_0 - V_f\ F_f}{V_0\ F_0} \times 100$$

where V_0 and V_f are the starting and final volume, respectively, whereas F_0 and F_f represents the fluorescence of the incubation medium at time zero and at the end of incubation. Percentage of uptake was therefore normalized for the weight of dried membranes and data expressed as µg of NPs *vs.* mg of dried membrane.

3.4.2.17. Evaluation of NPs mucoadhesiveness . *In vitro* mucoadhesive properties have been evaluated by assessing the interaction between NPs and mucin from porcine stomach (type III, bound sialic acid 0.5 - 1.5%, stored at 4 °C, Sigma Aldrich). Mucin was purified prior the use by dialysis against deionized water. The solution was thereafter filtered through 8 µm Millipore filters and then freeze-dried. Freeze-dried mucin was solubilized in deionized water at final concentration of 2 mg mL^{-1}. NPs (0.82 mg mL^{-1} as final concentration) and mucin were mixed at different concentration ratios and resulting mixtures have been analyzed by DLS measurements. The change of NPs size distribution

was used as parameter to evaluate adhesive phenomena.

3.4.2.18. Statistical analysis. Data are expressed as means and standard deviations (SD). Statistical analysis was performed using Student's t test, and a p value of < 0.05 was considered statistically significant.

3.4.3. Results and discussion

The first part of this chapter is addressed to describe the study of the anti-inflammatory properties of butyrate. Two cell models were used: human macrophages and neutrophils. These cells intervene at different time frame during wound healing process as described in the introduction of the thesis, thus is worth investigating upon biological properties of butyrate among both. Human monocytes are able to cross the membrane vessels and consequently migrate to inflamed site. Herein cells face numerous stimuli thus turning their phenotype into active macrophages able to tackle inflammation. To mimic such condition, monocytes have been differentiated into macrophages by PMA and afterwards stimulated by LPS, a potent pro-inflammatory endotoxin residing in the outer membrane of $Gram^-$ bacteria. Different concentrations of butyrate were explored to check the reduction of pro-inflammatory cytokines production by macrophages and results are pointed out in Figure 30. The take home message of this early investigation is that butyrate dampens the production of all cytokines in a dose-response manner with the highest activity at the concentration 0.5 mM. Interestingly, this activity was proved only when butyrate was pre-incubated with cells for 24 h prior stimulation with LPS. Conversely, if cells were treated with butyrate and LPS simultaneously, any anti-inflammatory evidence was not detected. It is well known that butyrate plays its biological activity mainly by two distinct pathways: a "quick" pathway through membrane-associated G-coupled proteins and a "slow" pathway through the inhibition of histone deacetylase (HDAC) causing histones hyperacetylation.(*82*) Given these considerations, it is reasonable to hypothesize that butyrate acts *via* HDAC pathway on the present cell model by modulating transcriptional regulation owing to HDAC inhibition. However, further analyses are needed to validate this supposition.

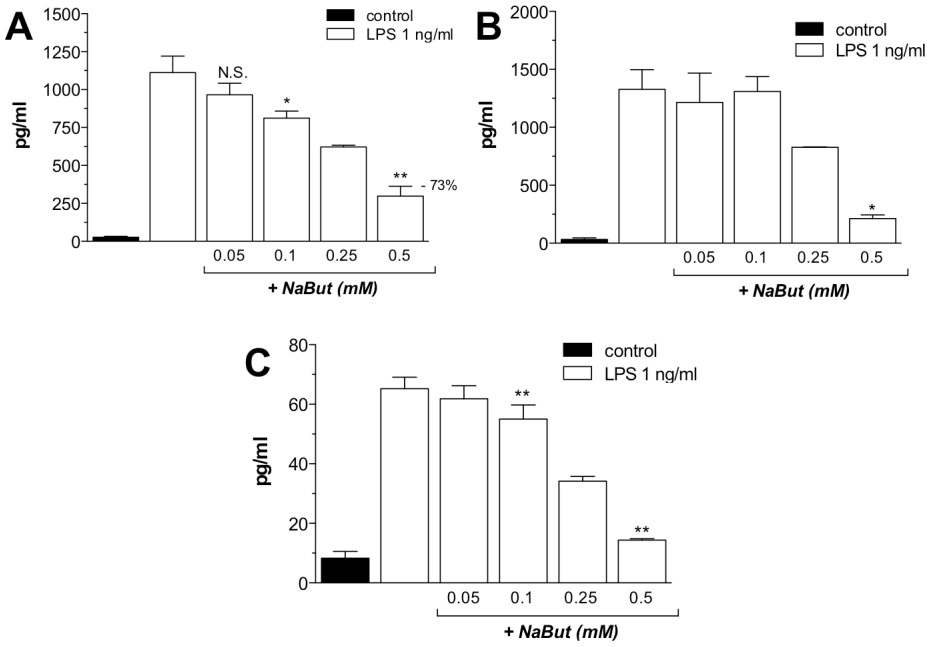

Figure 30. Effect of butyrate on the production of pro-inflammatory cytokines by LPS-stimulated macrophages: (A) TNF-α, (B) IL-6, (C) IL-1β. Control group represents non-stimulated cells. Cytokines are expressed as pg mL^{-1} and have been quantified by means of ELISA assays.

Concerning neutrophils, preliminarily it was observed that the degree of inhibition of superoxide production was strongly dependent on the length of preincubation with butyrate before the addition of TNF as pro-inflammatory stimulus. If cells were pretreated for 15 min with butyrate, superoxide production was reduced to a much lesser extent than cells encountering butyrate and TNF simultaneously. The inhibitory effect was unnoticeable if pretreatement with butyrate was extended to 30 - 60 minutes. As a consequence, experiments were performed by exposing neutrophils to butyrate immediately before addition of the stimulus. Figure 31A shows the dose-response curve of TNF-stimulated neutrophils residing on fibronectin (FN). Butyrate exerted its highest inhibitory activity at 1 mM, a concentration far lower than those generally reported in the literature.(*84*),(*89*) Such a discrepancy might be well justified by considering that (*i*) published results are obtained mostly with cells in suspension, which may behave much differently from neutrophils in adherent conditions, and (*ii*) preincubation of cells with butyrate before addition of agonist is a common procedure that could however limit butyrate efficacy in a manner similar to that discussed above, warranting the use of high concentrations to achieve a significant effect. In this regard, it is noteworthy that at concentrations equal or higher than 2.5 mM the effect of butyrate in the investigated model was comparable with

that of equimolar solutions of NaCl or sodium gluconate. This implies that at high butyrate concentrations the observed inhibition of the respiratory response is ascribable to the increased toxicity of the medium rather than to a specific effect of butyrate. It is well known, in fact, that neutrophils functions, especially in adherent conditions, are extremely susceptible even to slight hypertonic changes.(*207*) Since the metabolic activation of neutrophils in response to TNF is strictly adhesion-dependent, the interference with cell attachment and/or spreading was studied afterwards. The results reported in Figure 31B prove that neutrophil adhesion to FN was unaffected by the presence of butyrate.

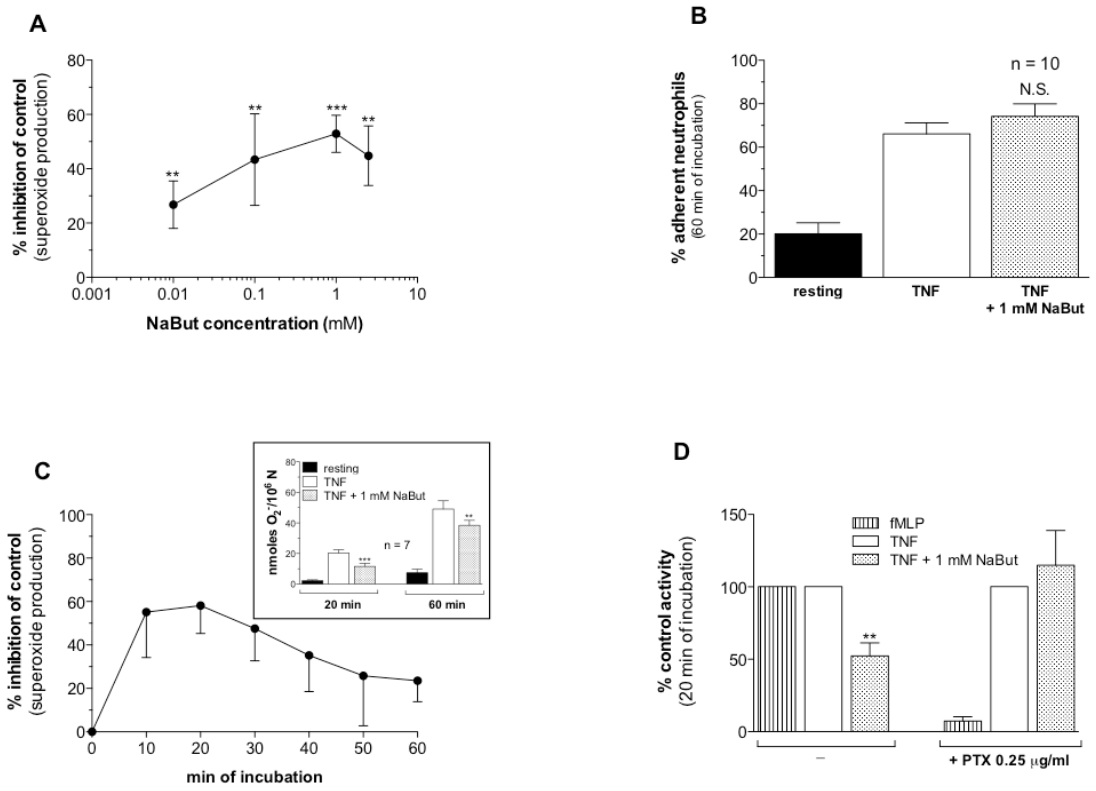

Figure 31. Biological properties of butyrate towards human neutrophils. (A) Percentage of inhibition with respect to control group of superoxide anion production by butyrate at different concentrations. (B) Effect on neutrophils adhesion on fibronectin by butyrate at 1 mM. (C) Time-dependency anti-inflammatory activity of 1 mM butyrate. (D) Elucidation on the possible mechanism of action of butyrate: cells were treated with pertussis toxin (G-coupled protein inhibitor) and stimulated either with fMLP or TNF. Statistical differences were determined by means of Student's t test. NS: no statistical differences; $^{**}p < 0.01$; $^{***}p < 0.01$.

Herein it has to be stressed that the effectiveness of butyrate in reducing O_2^- production appeared to be time-dependent: superoxide inhibition was maximal at about 20 min of incubation with TNF, then tended to decline with time (Figure 31C). A possible explanation for this trend comes from the experiments performed with pertussin toxin (PTX). As a G-protein inhibitor, PTX hinders the signaling pathway of the G-protein coupled receptor 43 (GPR43), which recognizes butyrate and is highly expressed on neutrophils. As shown in Figure 31D, the inhibitory effect of butyrate on TNF-induced superoxide production is abolished in the presence of PTX, indicating that butyrate activity is exerted mainly by interaction of extracellular butyrate with GPR43. Since butyrate uptake by neutrophils is likely rapid, as evidenced for other cell types as colonocytes, it can be hypothesized that the observed short-term inhibitory effect follows the actual butyrate concentration in the incubation medium, which is expected to diminish with time thus limiting butyrate binding to GPR43. This is supported also by preliminary observation above mentioned on the drastic reduction in butyrate effect when neutrophils are preincubated with the fatty acid prior to TNF exposure.

As described before, butyrate is a molecule able to manifest an anti-inflammatory activity by likely two different pathways in human macrophages and neutrophils. In spite of this, the activity of such molecule is reduced over time if neutrophil cells are considered. In order to prolong its biological properties, the idea was to produce a reservoir suitable to host and to fine control the leakage of butyrate thus providing a constant payload to the cells. Biopolymer nanoparticles (complexes) based on CH and HA were fabricated with the aim to encapsulate butyrate. The synthesis of nanoparticles take place in a step-by-step process depicted in Figure 32A.

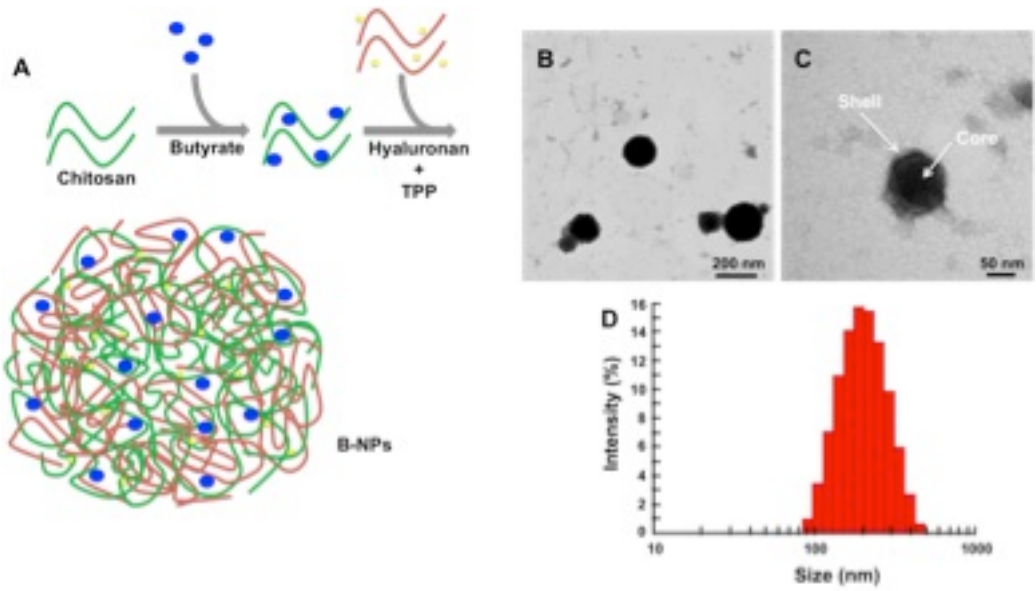

Figure 32. (A) Experimental setup to fabricate butyrate-loaded nanoparticles (B-NPs): the butyrate was first mixed with a chitosan solution under stirring; thereafter a solution of HA/TPP was added dropwise in order to favor the electrostatic/hydrophobic interactions between polysaccharides. The final construct is a nanoparticle containing butyrate. (B-C) TEM investigation at different magnification of NPs made of chitosan with Fa < 0.008 and HA/CH weight ratio of 2:1 demonstrated the presence of nanoparticles with a round-shape morphology and with a core-shell structure. (D) Size distribution of the previous formulation pointed out as percentage of DLS intensity.

Butyrate was first mixed with CH, wherein an electrostatic interaction between the carboxylic group of such molecule and the positive amino groups of polymer occurred. When the HA-TPP solution was dropped into the CH-butyrate mixture, resulting solution became progressively turbid so as to indicate the formation of nanoparticles. Herein, the opposite charge of both polysaccharides, the ability of chitosan to undergo a liquid-gel transition in the presence of TPP and the interchain interactions are considered the driving forces for the development of such nanoparticles.(*208*) The HA/CH weight ratio was varied so as to obtain several formulations. Dynamic Light Scattering and ζ-potential analyses were performed to investigate dimensions, surface charge and polydispersity and the outcomes are reported Table 7. Both chitosans demonstrated to foster the formation of NPs with different properties. This represented a very interesting finding in the case of the highly acetylated chitosan (Fa = 0.64) considering its very poor availability of positive charges to make the formation of NPs possible. TEM analyses at different magnification

(Figure 32B-C) in dried state confirmed the presence of nanoparticles with a round-shape morphology and with approximately similar dimensions to those calculated by means of DLS measurements. By comparing the butyrate-free formulations, interesting differences can be traced. NPs made of chitosan with Fa < 0.008 were found to gradually diminish their dimensions by increasing the HA/CH weight ratio. This phenomenon may be easily explained considering the porous nature of such NPs. Indeed, when HA is added to CH, the polyanion tends to penetrate along the chitosan network, which can accommodate the anionic polysaccharide in its internal structure leading to a more cross-linked and therefore shrunken core, as already described by Almalik *et al*.(*209*) The increasing of HA mass affects even the surface charge of NPs, by varying from ~ 52 to -25 mV when the HA/CH mass ratio was tuned from 1:2 to 2:1. The excess of HA is supposed to form a coating (Figure 32C), which cover the cross-linked core of CH and HA according to the core-shell model already proposed for either chitosan and alginate or chitosan and dextran complexes.(*210*),(*211*)

Nanoparticles	Chitosan (Fa)	Butyrate (mM)	HA:CH weight ratio	Particles size (nm)	ξ- potential (mV)	PDI
NPs	< 0.008	0	1:2	771 ± 20	51.7 ± 0.7	0.33 ± 0.05
			1:1	206 ± 3	34.0 ± 0.2	0.18 ± 0.01
			2:1	190 ± 1	- 24.8 ± 0.5	0.10 ± 0.01
B-NPs		0.1	1:2	905 ± 14	47.2 ± 2.0	0.28 ± 0.12
			1:1	201 ± 2	32.5 ± 0.6	0.24 ± 0.01
			2:1	212 ± 1	- 26.1 ± 0.4	0.15 ± 0.02
		1	1:2	300 ± 5	40.4 ± 0.5	0.32 ± 0.06
			1:1	175 ± 4	31.1 ± 0.4	0.11 ± 0.03
			2:1	232 ± 1	- 27.1 ± 0.2	0.16 ± 0.02
		10	1:2	189 ± 2	28.2 ± 0.6	0.12 ± 0.03
			1:1	422 ± 8	23.9 ± 0.9	0.06 ± 0.04
			2:1	317 ± 4	- 34.3 ± 1.0	0.20 ± 0.05
NPs	0.64	0	1:2	196 ± 2	20.7 ± 0.2	0.15 ± 0.02
			1:1	255 ± 2	- 22.6 ± 0.5	0.21 ± 0.01
			2:1	230 ± 4	- 25.3 ± 0.3	0.33 ± 0.04
B-NPs		0.1	1:2	465 ± 46	13.0 ± 0.3	0.09 ± 0.10
			1:1	268 ± 1	- 24.8 ± 0.4	0.21 ± 0.06
			2:1	434 ± 2	-30.0 ± 0.3	0.44 ± 0.11
		1	1:2	824 ± 4	13.7 ± 0.3	0.26 ± 0.04
			1:1	287 ± 1	- 23.1 ± 0.1	0.18 ± 0.04
			2:1	456 ± 9	- 27.6 ± 2.1	0.53 ± 0.41
		10	1:2	687 ± 23	- 3.9 ± 0.7	0.42 ± 0.07
			1:1	821 ± 109	- 23.3 ± 3.5	0.60 ± 0.06
			2:1	994 ± 116	-31.9 ± 0.3	0.66 ± 0.39

Table 7. Plain (NPs) and butyrate-loaded (B-NPs) nanoparticles were fabricated by using chitosans with different acetylation degree (Fa) by varying the butyrate concentration and the polymer's weight ratio. The particles size distribution, the ξ-potential and the polydispersity index were determined by Dynamic Light Scattering analyses. All results are the mean (± SD, $n = 3$).

The abundance of HA with respect to CH was found also to positively reduce the size distribution of NPs as demonstrated by the decrease of PDI (Table 7). In the case of NPs

produced with chitosan with Fa 0.64, the increasing amount of HA was not found to significantly influence the dimension of NPs (from ~ 196 to 230 nm when the HA/CH mass ratio was changed from 1:2 to 2:1). This is probably ascribed to the low availability of positive amino groups able to interact with HA, as proved by lower ζ-potential values. Conversely to the NPs made of CH with Fa < 0.008, the PDI progressively increased by augmenting the amount of HA for the NPs made of CH with Fa 0.64, a condition due to minor interactions between the two polysaccharides and consequently broadening of size distributions.

When butyrate was added at different concentrations to both chitosan solutions and the formation of B-NPs took place, some differences were identified with respect to NPs (Table 7). The presence of such molecule within the core of nanoparticles affects the hydrodynamic diameter, the surface charge and the particle size distribution. More in detail, the higher is the concentration of butyrate the lower is the ζ-potential for all formulations investigated, thus suggesting electrostatic interactions between the fatty acid and the chitosan. Nevertheless, hydrophobic interactions between the butyrate and the biopolymer's chains that successfully contribute to the encapsulation of the molecule can not be neglected.

The colloidal stability of B-NPs is a pivotal feature for such nano-systems. Opposite charged polyelectrolyte complexes are in fact strongly affected by the presence of salts (because of screening effects between charges) and by the pH.(*212*),(*210*) For instance it has been already demonstrated that the stability of CH/HA-based nanoparticles is influenced when they were moved from deionized water to PBS buffer.(*213*) This could represent the major issue for their potential use both in *in vitro* and *in vivo* models. Most recently Wu *et al*. demonstrated that CH/HA-polyelectrolyte complexes can be easily stabilized in physiological salts and pH conditions by the addition of metallic Zn^{+2},(*214*) but biocompatibility analyses are necessary for such system prior its use for biomedical applications. In the present study the time stability of B-NPs in both deionized water and PBS buffer was evaluated. The latter was conveniently selected because of its adequate ionic strength (~ 150 mM) and pH (7.4), which mimics a physiological milieu and the results are shown in Figure 33.

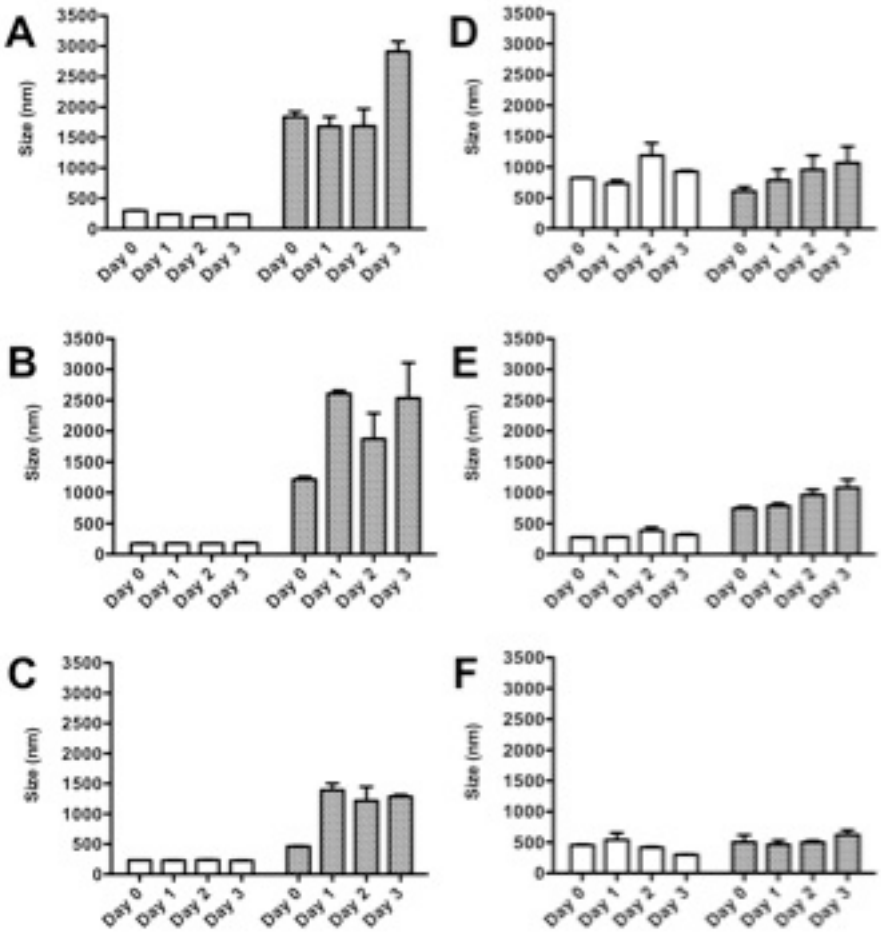

Figure 33. Evaluation of B-NPs stability in deionized water (empty columns) and in PBS buffer (filled columns) at 37 °C. The stability was studied by evaluating the particle size distribution up to three days by means of DLS analyses. (A,B,C) formulations made of chitosan with a Fa < 0.008. The weight ratios HA/CH were 1:2, 1:1 and 2:1, respectively. (D,E,F) formulations made of chitosan with a Fa = 0.64. The weight ratios HA/CH were 1:2, 1:1 and 2:1, respectively. All formulations studied were fabricated with a final butyrate concentration of 1 mM.

B-NPs made of chitosan with Fa < 0.008 and HA/CH of 1:2 are firmly affected by the change of medium: B-NPs rapidly increased their dimensions when dispersed in PBS until to reaching roughly 1.8 μm as hydrodynamic radius average (Figure 33A). B-NPs demonstrated to be stable in the first two days while again increased their dimensions in such conditions. Conversely, B-NPs in deionized water retained their size distribution in the same timeframe. A probable explanation is that the deprotonation of chitosan $-NH_3^+$ groups (due to the increase of pH), the ionic strength and the presence of phosphates in such buffer led to the destabilization of B-NPs causing aggregation phenomena. This

aspect was evident by the presence of a flocculated suspension after 24 h. Some attempts were performed by modulating pH and/or the ionic strength to understand which mechanism governs the aggregation. We observed that when 0.9% w/v of NaCl were added to B-NPs dispersed in deionized water and DLS analyses were carried out, particle size distribution increased in the same way, thus ruling out phosphates as probable cross-linkers between nanoparticles. On the contrary, no aggregation phenomena occurred when the pH was tuned in the range 7.0 - 7.4, so as to attribute to the ionic strength the origin of aggregation. By increasing the HA/CH weight ratio, the aggregation can be limited and resulting B-NPs in PBS are weakly larger with respect to those in deionized water at time zero (Figure 33B,C). Nevertheless, aggregation progressively occurred thereafter and dimensions were found similar to those described above. On the other hand, the size distribution of B-NPs made of chitosan with Fa 0.64 and dispersed in both media was almost comparable (Figure 33D,E,F). More in detail, no apparently aggregation phenomena were identified for formulations with 1 mM of butyrate and different HA/CH weight ratio. This can be ascribed to the highly acetylation degree of CH, resulting in a lower net positive charge. In these conditions, the increasing of pH and screening effects by the presence of salts did not allow aggregation phenomena since the stability was mostly ensured by hydrophobic interactions between the polysaccharides. The dimensions of such nanoparticles did not excessively increased (if compared to B-NPs made of chitosan with Fa < 0.008), albeit the size distribution was variable during the three days of incubation due to swelling phenomena. The possibility to avoid the aggregation (and following flocculation) of B-NPs in PBS buffer simply using a more acetylated chitosan represents a noteworthy result.

Some conclusions can be drawn: the behavior of B-NPs in physiological conditions varies on which CH is used and on the polysaccharide/butyrate concentration and their stability is sufficiently ensured only for a narrow range of formulations investigated. Another parameter to take into account is the role of HA as coating for B-NPs. Indeed, the presence of HA guarantees some advantages as well as a net negative surface charge allowing shield against the adsorption of proteins, protection *versus* macrophage uptake,(*215*) and feasibility to bind HA receptors as CD44 both on inflammatory and tumor cells enabling a selective targeting.(*216*),(*203*) Considering the parameters reported in Table 7 together with stability analyses above discussed and preliminary biological studies, the following best formulation was chosen for further analyses:

Chitosan with Fa = 0.64; butyrate 1 mM; HA/CH 1:1

The encapsulation efficiency was calculated and was assessed at 77%.

HA and CH are well known to possess the ability to react with ROS.(*217*) To investigate about scavenging properties of the resulting plain carrier, an acellular model based on the xanthine - xanthine oxidase system was used (Figure 34).

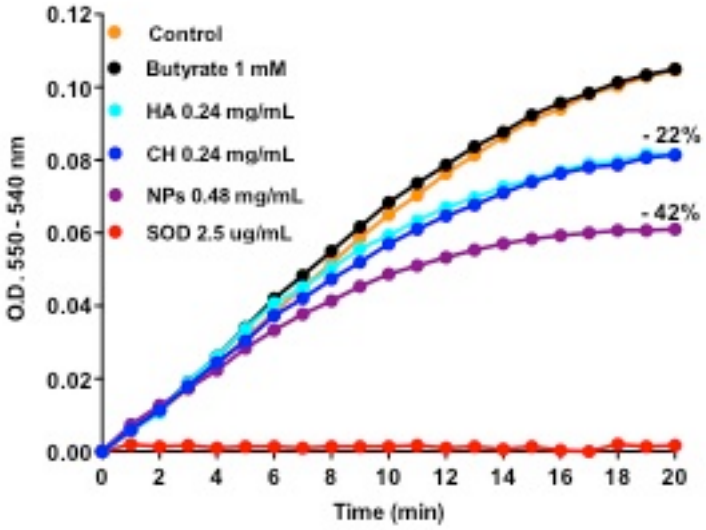

Figure 34. Evaluation of the NPs scavenging properties by means of the xanthine-xanthine oxidase model. NPs, butyrate and free polysaccharides were incubated at indicated concentrations and the kinetics was followed up to 20 minutes. Superoxide dismutase (SOD) was used as positive control.

HA and CH at the same concentrations as that in the best NP formulation induced a decrease in cytocrome *c* reduction up to 22%, while cytocrome c reduction induced by NPs was equal to 42%, thus demonstrating a significant sum scavenger effect.

Subsequently, the association and/or internalization of NPs in neutrophils were studied by means of cytometric analyses and the outcomes are pointed out in Figure 35.

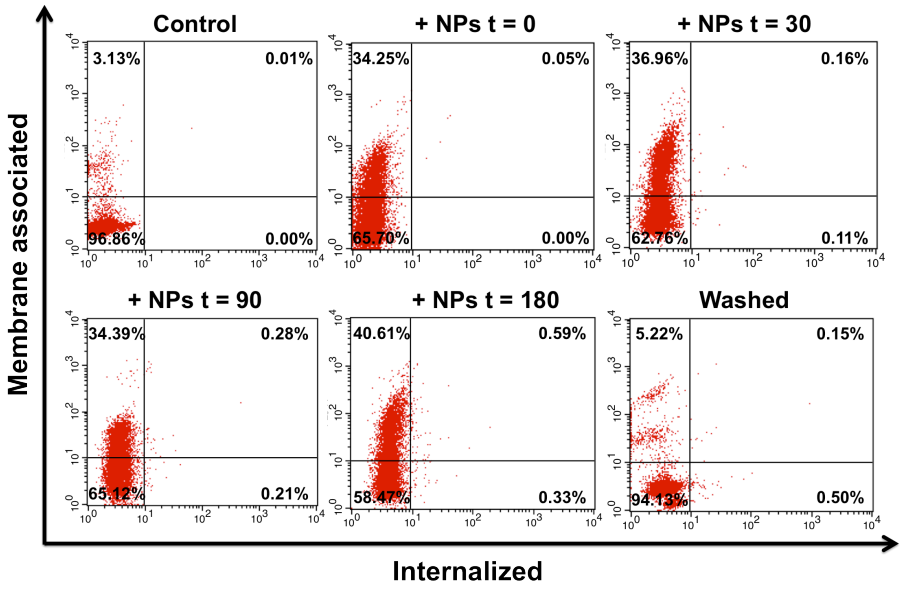

Figure 35. The association and the internalization of NPs *versus* human neutrophils was verified by means of flow cytometry. TNF-stimulated neutrophils were incubated at 37 °C with fluoresceinamine-isomer I-labeled NPs (except for control group) and analyzed at selected times (from t = 0 to 180 min). At the end of the experiment, neutrophils were centrifuged, resuspended and subsequently analyzed (washed panel). Green fluorescence due to fluoresceinamine-isomer I was collected using a 530 ± 30 band pass filter whereas red fluorescence emitted from trypan blue (75 μg mL^{-1} as final concentration) bound to fluoresceinamine-isomer 1 was collected by using a 650 ± 13 bandpass filter. For each sample 10 000 events were considered.

Control group shows the majority of the cells in the down left quadrant with the presence of only a small quenched fluorescence due to the presence of the TB. As soon as the NPs were added to the cells (t = 0 min) a significant red-shift occurred, ascribed to a quick association of the NPs with the cells. By increasing the time of exposure to t = 180 min, a progressively higher percentage of cells was found to be positive for both membrane binding (up left and right quadrant) and internalization (up and down right quadrant). By considering the percentage of cells who internalized NPs (0.33%) as well as the percentage of the cells which both internalized and associated NPs (0.59%), an internalization of ~ 1% and a binding efficacy of ~ 41% after 3 hours of incubation can be estimated. A further control was carried out in order to validate the presence of NPs at the membrane level. Human neutrophils were centrifuged at the end of incubation in order to favor the detachment of nanoparticles from the cells. The panel in Figure 35 shows that after centrifugation the quenched fluorescence reverted to the down left quadrant thereby

indicating that NPs were detached from cells and consequently eliminated when neutrophils were centrifuged and thereafter resuspended. By these evidences, it can be concluded that the association of the NPs with the neutrophils is weak (likely ascribed to the interaction between the HA and CD44 receptor of PMN)(*209*) whilst only a small amount of cells was effectively positive to the internalization. The percentage of uptake is lower compared to other models in which CH/HA-nanoparticles have been used. For instance, the overexpression of CD44 and a different experimental setup led to an internalization of ~ 80% in a breast cancer cell model.(*203*) This represents an advantage for the system presented in this chapter, considering that the anti-inflammatory activity of butyrate is probably exerted mainly *via* GPR43 receptor towards neutrophils.

Considering the time-dependence of the anti-inflammatory activity of butyrate, one of the main purposes for this work was to provide a smart tool able to guarantee the right amount of payload at the right time to neutrophils. To investigate this aspect, release studies of butyrate from B-NPs were performed in PBS buffer. As shown in Figure 36, the leakage profile of butyrate from B-NPs was almost constant in the first twenty minutes with approximately 45% of butyrate leaked from nanoparticles in such time frame. Further, the leakage tends to slow down and progressively to reach a plateau. The cumulative release reached ~ 87% up to 4 h of incubation. It is noteworthy mention that the cumulative release of butyrate from B-NPs did not significantly vary up to 72 h (not shown) never reaching 100%. Overall, chitosan-hyaluronan nanoparticles have proved behaving as break for the butyrate leakage, taking into account that preliminary experiments demonstrated that the release of free butyrate in the same experimental conditions reached 100% only after 2 hours of incubation. As a consequence, B-NPs may be considered as a controlled release system for the short chain fatty acid. However, by comparing such nanoparticles with similar ones reported in literature, a faster leakage was found, probably due to the different nature of the cargo and polysaccharide's features.(*203*)

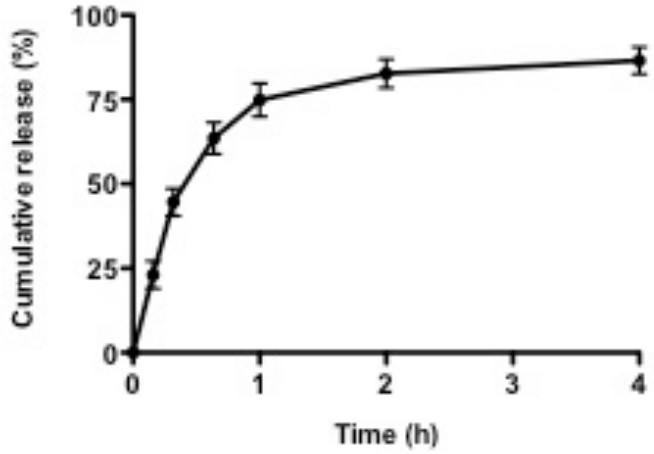

Figure 36. *In vitro* cumulative release of butyrate leaked from B-NPs (black solid line) with HA/CH of 1:1 and chitosan Fa 0.64 in the first 4 h of incubation. The experiments (n = 3) were performed in PBS buffer at 37 °C to mimic a physiological milieu.

To evaluate the lack of cytotoxicity of NPs, AlamarBlue assay was performed on murine fibroblast-like NIH-3T3 cells and results are reported in Figure 37.

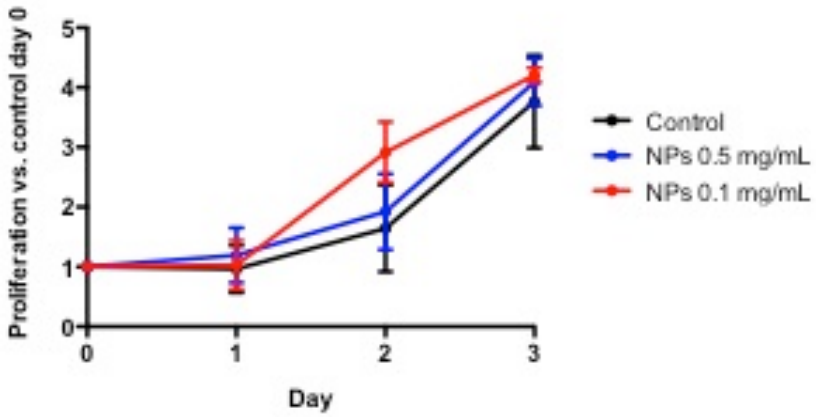

Figure 37. Proliferation rate of NIH-3T3 cells treated with NPs at different concentrations. Control group represents untreated cells. Proliferation was measured by means of AlamarBlue assay and data are normalized with respect to day 0 and expressed as mean (± SD, n = 6).

Figure 37 shows that NPs at different concentrations did not prove any effect on the proliferation of NIH-3T3 cells up to three days of incubation thereby suggesting lack of

toxicity of such constructs.

The further aim was to study the mucoadhesive properties of NPs for potential applications in inflammatory bowel disease treatments. Polysaccharide-based complexes can be extensively studied in terms of muco-adhesive properties by adopting several approaches. The most commons deal with the use of mucin as *in vitro* model of gastric mucus and with the use of portion of animal stomachs/intestines for *ex vivo* analyses. A very useful technique to verify mucoadhesive properties is to follow variations of dimension and distribution of aggregates by means of DLS measurements upon NPs and mucin mixing. This approach was followed in this work and results are pointed out in Figure 38. While the NPs show a typical unimodal size distribution with very low PDI (indicating the presence of a homogeneous dispersion of complexes in solution), mucin at concentration 1 mg mL^{-1} shows a bimodal distribution with the presence of two peaks at 642.7 and 54.7 nm. This mucin distribution is in agreement with other works. For instance, Sogias *et al.* demonstrated a bimodal distribution and similar range of dimensions for mucin at the same concentration.(*218*) By mixing NPs and mucin at different concentration ratios (*r*), a progressive increase of the Z-average was noticed by increasing the amount of mucin. More in detail, the Z-average was found to scale linearly with the concentration of mucin as pointed out in the plot of Figure 38 thereby indicating aggregation phenomena. At the same time, the peak 2 of mucin at ~ 50 nm disappeared by merging into a unique one when NPs were added, thus indicating the presence of a more uniform distribution, as even confirmed by reduced values of PDI. However, PDI tends to gradually increase by augmenting the amount of mucin so as suggesting the onset of more unstable colloidal systems. Sogias *et al.* concluded their work claiming that electrostatic interactions, hydrogen bonding and hydrophobic effects cooperate to favor mucoadhesive interactions between chitosan and mucin. Electrostatic interactions may be easily ruled out for the NPs presented in this chapter as contribution for mucoadhesion considering their negative ξ-potential (~ -20 mV) as well as the negative charge of mucin for the pH investigated (~ -18 mV).(*218*) Conversely, both hydrogen bonding and hydrophobic effects might be with no doubt considered the root of mucoadhesive interactions.

	Z-average (nm)	PDI	Peak 1 mean intensity (nm)	Peak 2 mean intensity (nm)	Peak 1 area intensity (%)	Peak 2 area intensity (%)
NPs	286.8	0.101	323.3	0	100	0
r: 0	281.6	1.000	642.7	54.7	84.4	15.6
r: 4.10	298.3	0.149	350.1	0	100	0
r: 0.82	340.1	0.240	439.8	0	100	0
r: 0.41	379.2	0.294	501.6	0	100	0

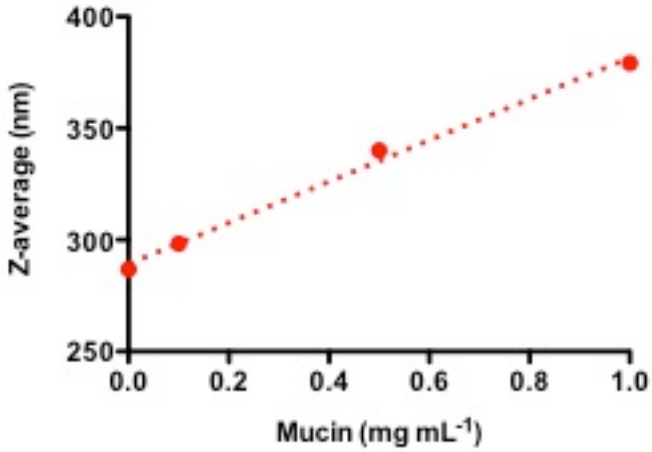

Figure 38. DLS analyses to elucidate the muco-adhesive properties of NPs. In the table are reported the hydrodynamic diameter (Z-average), the polydispersity index (PI), the percentages of intensities related to the dimensions and the area under the curves of size-distribution profiles. NPs (0.82 mg mL^{-1}) were added to mucin (0.1, 0.5 and 1 mg mL^{-1} as final concentrations) with 1:1 v/v. *r* value is the concentration ratio between NPs and mucin. Final pH after mixing was ~ 5.5. In the plot is pointed out the trend of Z-average of complexes *versus* amount of mucin. The dashed line represents the linear fitting among experimental points ($R^2 > 0.99$).

The last part of present work was addressed to load nanoparticles within the chitosan membranes described in the previous chapters of this thesis. As a proof of concept, plain carriers were considered. The basic idea was to load the NPs by exploiting the ability of membranes to uptake water and consequently to swell as already demonstrated beforehand. NPs present in the soaking medium are supposed to be internalized in the membranes by diffusion phenomena. As expected, when membranes were incubated for 24 h with NPs, the decrease of fluorescence in the incubation medium was evidenced, thus suggesting the incorporation of NPs within membranes. Considering the amount of water diffused during this time frame, the amount of NPs up taken was assessed being 4.86 ± 0.65 μg per mg of

dried membrane. Further studies are needed to evaluate the leakage of such constructs from chitosan matrices and, consequently, the release of the payload.

3.4.4. Main conclusions

- Butyrate demonstrated dose- and time-dependent anti-inflammatory activities on two immune cell models;
- The production of chitosan-hyaluronan nanoparticles (complexes) to host butyrate was addressed;
- The stability of the nanoparticles in a physiological medium was found being strongly affected by the acetylation degree of chitosans;
- Plain complexes demonstrated to behave as radical scavenger and to display lack of cytotoxicity and mucoadhesive properties;
- Complexes loaded with butyrate constitute a potential controlled release system for the delivery of the short chain fatty acid.

CHAPTER V

Biological properties of a silver/lipoate hyaluronan derivative

3.5.1 Aim of work

In this chapter, a novel complex of sodium hyaluronate-lipoate with silver ions (termed SHLS12) is described. It has been studied in terms of biological properties of a biomaterial usable for the treatment of non-healing wounds. The present contribution is part of a more extent work carried out in collaboration with Sigea Srl company, Trieste (Italy).

3.5.2. Materials and methods

3.5.2.1. Materials. Sodium hyaluronate (Phylcare Sodium Hyaluronate extra LW) employed in this study was purchased from Biophil Italia Spa (M_w ~ 100 - 400 kDa). Sodium hyaluronate-lipoate (SHL, see Figure 39), prepared as previously reported,(*219*) had a degree of substitution of 0.3 as determined by NMR analysis with a corresponding molar mass of the repeating unit equal to 457.5 g mol^{-1}. Neutral Red, Thiazolyl Blue Tetrazolium Bromide (MTT), phenazine methosulfate (PMS), bovine serum albumin (BSA) powders, fetal bovine serum, Luria-Bertani (LB) broth, LB Agar, Brain Heart Infusion (BHI) broth, silver acetate (≥ 99.0%) and phosphate buffered saline (PBS) were all purchased from Sigma-Aldrich (Chemical Co.). Dulbecco's Modified Eagle's Medium, fetal bovine serum, penicillin, streptomycin and glutamine solutions were purchased from EuroClone, Italy. All chemicals and reagents were of the highest purity grade commercially available.

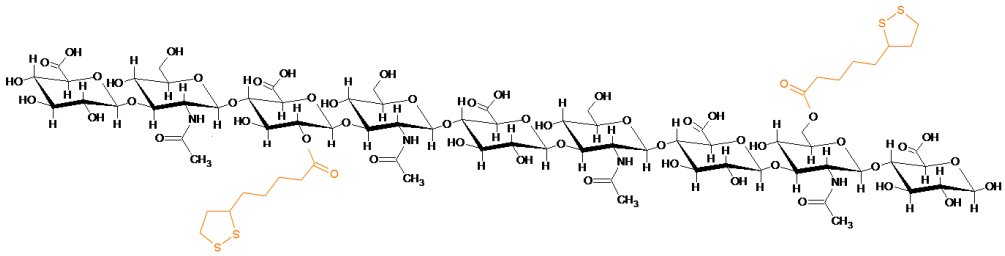

Figure 39. SHL structure.

3.5.2.2 Antibacterial tests. The antibacterial activity of SHLS12 was evaluated using strains of *Escherichia coli* (ATCC® 25922™), *Staphylococcus epidermidis* (ATCC® 12228™), *Staphylococcus aureus* (ATCC® 25923™) and *Pseudomonas aeruginosa* (ATCC® 27853™).

3.5.2.2.1 Growth inhibition assay. Growth inhibition assay was performed according to the protocol described in (*220*) with slight modifications. SHLS12 solution (0.2% w/v) was prepared by adding SHLS12 in LB broth and vigorously vortexed for 30 seconds in order to obtain a clear and homogeneous dispersion of the polymer in such medium. Bacterial suspensions were prepared by adding 20 µL of bacteria, preserved in glycerol, to 5 mL of LB broth. The obtained suspensions were incubated overnight at 37 °C. After 24 h, 500 µL of bacterial suspension was diluted in 10 mL of broth and grown up for 90 min at 37 °C in order to restore an exponential growth phase. Bacterial concentration was measured by means of optical density (OD) at 600 nm. After centrifugation (3500 rpm, 5 min), supernatants were removed and bacteria were resuspended with either SHLS12 solution in LB broth or LB broth to obtain a final concentration of 5 x 10^6 bacteria mL^{-1}. In the case of evaluation of the BSA influence on SHLS12 activity, bacteria were resuspended in LB broth added with either BSA (40 g L^{-1}) or BSA and SHLS12 (40 g L^{-1} and 0.2% w/v, respectively). All bacteria strains were then incubated at 37 °C for 4 h in shaking conditions (140 rpm). At the end of incubation, bacterial suspension was serially diluted in PBS buffer (from 10^{-1} to 10^{-5}) and 25 µL of each suspension were plated on LB agar. After overnight incubation at 37 °C, the colony forming units (CFUs) were counted. Outcomes were compared with the suspension of bacteria grown in liquid medium as control.

3.5.2.2.2 Biofilm formation. Bacterial suspensions of *S. aureus* and *P. aeruginosa* were prepared by adding 20 µL of bacteria, preserved in glycerol, to 5 mL of BHI broth *plus* 3% w/v sucrose. The obtained suspensions were incubated overnight at 37 °C. After 24 h, bacteria were diluted 1:100 in the same broth and plated (300 µL/well) into 24-well plates. For confocal laser scanning microscopy analyses, bacteria were plated on sterile 13 mm tissue culture coverslips (Sarstedt, USA) laid down on the bottom of the culture plate wells. Plates were incubated at 37 °C for 24 h to allow biofilm formation. After 24 h, broth was removed and formed biofilm was carefully rinsed twice with 100 µL of sterile PBS in order to remove planktonic cells. 300 µL of PBS containing 0.2% w/v of SHLS12 were

deposited on the bacterial layer. Biofilms were then incubated at 37 °C and MTT assay was performed according to the following protocol after 4 and 24 h of incubation.

3.5.2.2.3. Viable biomass assessment. The test was performed according to the protocol described elsewhere.(*197*) Briefly, MTT stock solution was prepared by dissolving 5 mg mL^{-1} of MTT powder in sterile PBS. PMS stock solution (0.3 mg mL^{-1}) was prepared by dissolving PMS powder in sterile PBS. Solutions were further filtered (0.22 μm filters, BioSigma, Italy) and stored at 2 °C in light-proof vials until the day of the experiment, when a fresh measurement solution (FMS) was prepared by mixing 0.5 mL of MTT stock solution, 0.5 mL of PMS stock solution, and 4 mL of sterile PBS. DMSO was used as lysing solution (LS). After the biofilm incubation period, SHLS12 and PBS were gently removed from the plates and each well was carefully rinsed three times with 100 μL of sterile PBS in order to remove non-adherent cells. 200 μL of FMS solution were placed into each well and the plates were incubated for 3 h under light-proof conditions at 37 °C. The FMS solution was then gently removed and formazan crystals were dissolved by adding 200 μL of LS to each well. Plates were additionally stored for 1 h under light-proof conditions at room temperature and then 100 μL of the solution were transferred into the wells of 96-well plates. The absorbance of the solution was measured using a spectrophotometer (FLUOStar Omega-BMG Labtech) at a wavelength of 550 nm. Outcomes were expressed as OD units.

3.5.2.3. Confocal laser scanning microscopy (LSCM). LSCM analyses were addressed at detecting viability of bacteria in the biofilm mass. FilmTracer Live/Dead biofilm viability kit (Invitrogen™) was used (see paragraph 3.3.2.9.).

3.5.2.4 Cell culture. Mouse fibroblast-like NIH-3T3 and immortalized human keratinocyte HaCaT cell lines were used for the in vitro experiments (see paragraph 3.3.2.10.).

3.5.2.5 Biocompatibility studies. *In vitro* cytotoxicity of SHLS12 was evaluated by using Neutral Red assay on both NIH-3T3 and HaCaT cells. 20 000 cells were plated on 24-well plates and, after complete adhesion, culture medium was changed with 300 μL of fresh medium. The cytotoxicity test was performed by direct contact of the cells with SHLS12 (50 μL of a solution 0.2% w/v) laid down on filter papers, (16 mm^2 as surface) placed in the middle of each well. As a positive control material, poly(urethane) films containing

0.25% zinc dibuthyldithiocarbamate (ZDBC) were used. As negative control material, plastic poly(styrene) sheets were used. Untreated cells (without any contact-material) were also considered as additional control. After 24 and 72 h, Neutral Red assay was performed according to the manufacture's protocol. Each material test was performed in triplicate. Cytotoxicity was expressed as percentage of viability by normalizing the OD_{540} nm of treated cells to the OD_{540} nm of the untreated cells.

3.5.2.6 Statistical analysis. Data are expressed as means and standard deviations (SD). Statistical analysis was performed using Student's t test, and a p value of < 0.05 was considered statistically significant.

3.5.3. Results and discussion

The main purpose for the present work was to use a hyaluronan-lipoate derivative (named Lipohyal)(*219*) to synthesize a silver complex with antibacterial properties and lack of toxicity towards eukaryotic cells. There are very few papers concerning the ability of HA to favor the binding and stabilization of silver in different chemical forms with respect to other biopolymers, *e.g.* chitosan or alginate.(*221*),(*222*) For instance, Abdel-Mohsen *et al.* developed HA fibers *via* wet-spinning method, which were formed and to stabilized silver nanoparticles.(*223*) Chudobova *et al.* demonstrated the formation of hyaluronate-silver complexes after the addition of silver nitrate to a solution of HA.(*224*)

The main characteristic of silver-containing biomaterials refers to their antibacterial properties against different bacteria strains without hindering the viability of mammalian cells. In this section, the ability of SHLS12 to influence the growth and viability of bacteria both in a planktonic and in an organized community state (biofilm) is reported. *E. coli*, *S. aureus*, *P. aeruginosa* and *S. epidermidis* strains were selected for such a purpose. Figure 40 points out the results obtained by growth inhibition assays. A small amount of SHLS12 (0.2% w/v) showed a marked antibacterial activity owing to the presence of silver ions. For all strains investigated, a significant drop of CFU (at least $p < 0.01$) was spotted for SHLS12-treated samples with respect to the control. This result is validated by visual observations as reported in Figure 40 E-H, which shows the growth of *S. aureus* colonies on LB agar for treated and untreated samples.

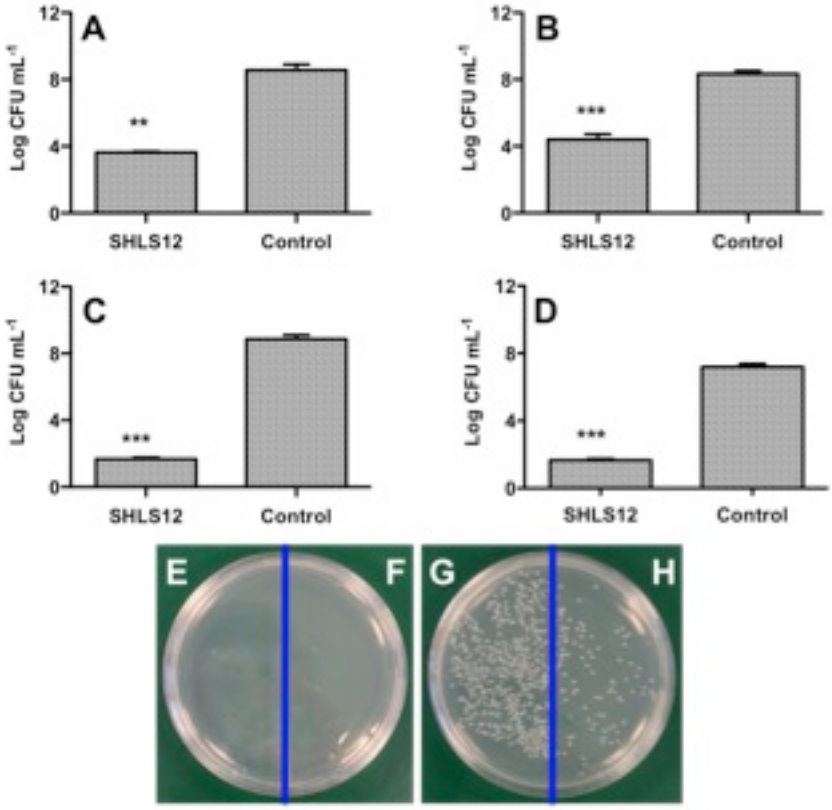

Figure 40. Growth inhibition rate expressed as Log CFU mL^{-1} of *S. aureus* (A), *S. epidermidis* (B), *E. coli* (C) and *P. aeruginosa* (D) following 4 h of treatment with SHLS12. Statistical differences were determined by means of Student's t test. $^{**}p < 0.01$; $^{***}p < 0.001$. *S. aureus* colonies on LB agar: diluted 10^{-4} (E) and diluted 10^{-5} (F) SHLS12-treated sample; diluted 10^{-4} (G) and diluted 10^{-5} (H) control sample.

The inactivation of silver by serum proteins can be a concern for *in vivo* applications of SHLS12. In particular, serum albumin has been shown to have specific binding sites for metal ions entering the bloodstream.(*225*),(*226*),(*227*) They are best characterized for human serum albumin (HSA) and for bovine serum albumin (BSA), which is often used as a model protein for HSA.(*228*) Zhao *et al.* proved the formation of complexes between Ag^{+} and BSA by spectroscopic investigation.(*229*) Ostermeyer *et al.* demonstrated that BSA dampened the toxicity of citrate silver nanoparticles by chelating silver ions leaked from silver nanoparticles (AgNPs) and by binding to AgNPs surface thereby preventing NH_3-dependent dissolution from occurring.(*230*) This aspect has also been investigated in another study where serum proteins reduced the antibacterial features of a colloidal solution of chitlac-nAg.(*75*) It should be reminded that at physiological pH the overall

charge of albumin is predominantly negative, thus electrostatic interactions with the chitlac polycation may be at the root of such an adverse effect. BSA at a concentration of 40 g L^{-1} was selected to verify its influence on the antibacterial properties of SHLS12. As shown in Figure 41, a significant drop of *S. aureus* and *P. aeruginosa* CFUs was spotted after 4 h of treatment with both SHLS12 and SHLS12 + BSA with respect to the control. By comparing SHLS12 with SHLS12 + BSA treated samples, no statistical differences were identified for *S. aureus*. Concerning *P. aeruginosa*, a significant but small difference was identified ($p < 0.05$), thus evidencing only a partial and minimal inhibitory effect of serum albumin towards SHLS12 antibacterial activity.

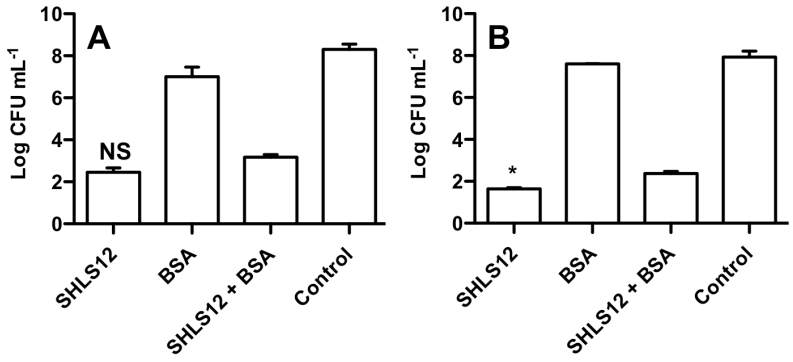

Figure 41. Growth inhibition rate in the presence/absence of BSA expressed as Log CFU mL^{-1} of *S. aureus* (A) and *P. aeruginosa* (B) following 4 h of treatment with SHLS12. Statistical differences were determined by means of Student's t test. NS no statistical differences between SHLS12 and SHLS12 + BSA-treated samples; *$p < 0.05$ between SHLS12 and SHLS12 + BSA-treated samples.

Another pivotal parameter that has been considered in this section is the capability of silver-complex to exert antibacterial activity towards organized-community of bacteria, so termed biofilms. Biofilms are characterized by an extracellular polymeric substance (EPS) that surrounds bacterial cells making them one thousand times more resistant to antibiotics and drugs than planktonic ones.(*38*) *S. aureus* and *P. aeruginosa* were selected for these studies because of their ability to form biofilms.(*220*),(*231*) Figure 42 A-B points out the outcomes obtained after 4 and 24 h of treatment of *S. aureus* and *P. aeruginosa* biofilms, respectively. In both cases, SHLS12 broke apart biofilm, as revealed by MTT colorimetric assay. The optical density (OD) of *S. aureus* treated with SHLS12 showed a reduction of ~

30% after 24 h of treatment compared to the control, whereas no statistical differences were observed after 4 h of treatment. At a variance, in the case of *P. aeruginosa* a marked OD reduction was spotted already after 4 h of treatment. It may be argued that *P. aeruginosa* is more susceptible than *S. aureus* strain to Ag^+ ions, likely because of their thinner cell wall, which enables silver ions to penetrate into the bacterial cell more easily.(*232*) These results were confirmed by differential biofilm staining for dead (red) and alive (green) cells and visualization with confocal laser scanning microscopy after treatment with SHLS12. In Figure 42 C-F *P. aeruginosa* and *S. aureus* biofilms show a green fluorescent layer indicating the good viability of bacteria in the case of control. Conversely, treated cells for 24 h with SHLS12 pointed out the presence of a non-homogeneous layer of bacteria with few viable green cells and a lot of reddish/yellow bacteria, so as to suggest cell suffering and biofilm disaggregation. These outcomes are in agreement with what evidenced in the viable biomass experiments reported above. Overall, growth inhibition assays and viable biomass assessment clearly proved antibacterial properties of SHLS12 thanks to the presence of silver ions which, as reported in literature, exert their activity (*i*) by interacting with thiol/phosphorus-groups of the cell wall and the plasma membrane proteins of bacteria,(*38*),(*56*) causing membrane damage or (*ii*) by binding DNA of microbes leading to cell division alterations.(*67*)

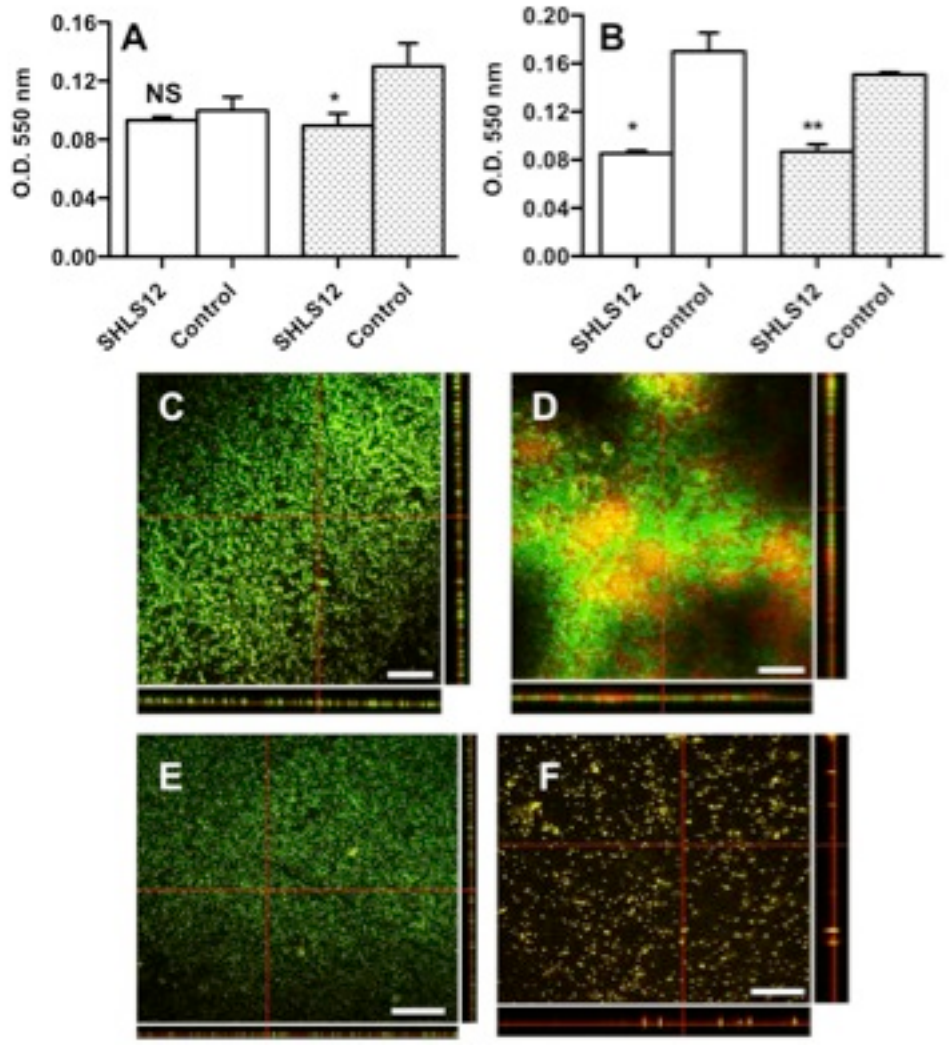

Figure 42. Viable biomass MTT assay expressed as O.D. at 550 nm of *S. aureus* (A) and *P. aeruginosa* (B) following 4 (empty columns) and 24 h (filled columns) of treatment with SHLS12. Statistical differences were determined by means of Student's t test. NS no statistical differences versus control; **p* < 0.05 versus control; ***p* < 0.01 versus control. LSCM images of *P. aeruginosa* biofilm: control group (C) and SHLS12-treated sample (D). LSCM images of *S. aureus* biofilm: control group (E) and SHLS12-treated sample (F). Biofilms were grown on tissue culture coverslips in BHI broth *plus* 3% w/v sucrose and following treated with SHLS12 for 24 hours. For cell staining, FilmTracer Live/Dead biofilm viability kit (Invitrogen™) was used. Green fluorescence indicates live cells whereas red and yellow fluorescence refers to dead and suffering ones, respectively. Scale bar was 50 μm for all images.

One of the most important challenge for silver-containing biomaterials concerns their ability to exert antibacterial activity without hindering the viability of eukaryotic cells. The toxicity of silver for mammalian cells is proportional to the amount of metal present in

environment, thus causing cellular damages if internalized.(*72*) A key strategy to dampen the toxicity of silver resides then in the fabrication of systems capable to avoid - or at least reduce - the leakage of silver, but at the same time, preserve its antimicrobial activity allowing for the direct interaction of the metal ions with the proteins localized on the bacterial surface. Polysaccharide-based materials loaded with silver nanoparticles have been already described to prevent an excess of silver release and thus not to affect the viability of mammalian cells.(*220*),(*62*),(*77*) In this view, it is reasonable that the amount of released metal is under the lethal dose threshold resulting not cytotoxic. To assess the biocompatibility of SHLS12, a Neutral Red cytotoxicity assay was carried out. As pointed out in Figure 43, SHLS12 did not exert any cytotoxic effect on the cell lines used. Indeed, there was no significant difference in Neutral Red signal between the SHLS12-treated and untreated cells after 24 and 72 h. The results of the positive control group on NIH-3T3 cells showed an apparently inexplicable result, namely a similar percentage of viability as the negative control after 4 h of treatment. However, this is likely ascribed to the slow cytotoxic activity of zinc dibuthyldithiocarbamate in poly(urethane) films towards such cell line. At 72 h the cytotoxicity of positive control was evident in all cases. The combination of results proves that SHLS12, besides providing a good antibacterial activity against biofilm-forming bacteria strains, is not dangerous for eukaryotic cells likely because silver ions are firmly coordinated and immobilized by the lipoate groups and therefore do not diffuse into the surrounding environment.

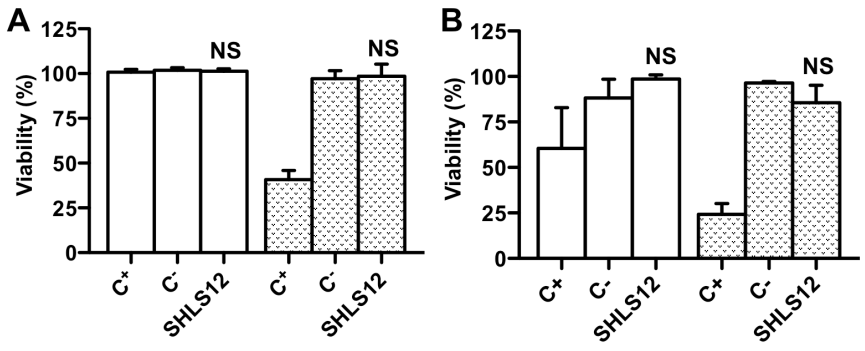

Figure 43. Percentage of viability of fibroblast NIH-3T3 (A) and ketatinocytes HaCaT (B) cells measured using Neutral Red assay. SHLS12 was kept in touch with cells and testing was performed after 24 (empty columns) and 72 h (filled columns) of treatment. Poly(urethane) sheets containing 0.25% zinc dibuthyldithiocarbamate were used as contact positive control (C^+) whereas plastic poly(styrene) sheets were used as contact negative control (C^-). Statistical differences were determined by means of Student's t test.

3.5.4. Main conclusions

- SHLS12 proved straightforward antibacterial properties towards different bacteria strains grown both in planktonic and sessile conditions;
- Such activity was mostly not affected by the presence of physiological amounts of serum proteins;
- The lack of cytotoxicity towards eukaryotic cells was demonstrated.

4. CONCLUDING REMARKS

Despite several medical resources are available for the treatment of lesions, non-healing wounds still represent a concern and challenge healthcare worldwide. Various non-surgical approaches have been investigated together with the use of numerous drugs to help the recovery of such wounds. Innovative polymer-based biomaterials are by far the most studied tools to entrap active molecules capable to face the multiplicity of negative aspects at damaged sites. In this context, the present thesis work wants to provide additional paradigms to tackle chronic wounds following an unambiguous thread starting from biomaterial fabrication to characterization.

Specifically, the main goals reached by the research activity presented in this thesis are summarized below.

- Homogeneous hydrogels and membranes based on chitosan and TPP were developed by exploiting an innovative approach through the ionotropic gelation process. A diffusion technique was selected in order to avoid the local saturation of chitosan binding sites, thus obtaining a macroscopic uniform hydrogel structure. The influence of chitosans with different Fa and M_w, concentrations of polymer, TPP and NaCl were studied in order to fabricate wall-to-wall systems and to tune the homogeneity of gelation. In addition, it was revealed that not only TPP but also PPi contributes to the gelation of chitosan. Soft and pliable biocompatible membranes have been finally prepared through a temperature-controlled freeze-drying procedure.

- Additional insights about the ionotropic gelation of chitosan-TPP-PPi system have been provided. Light scattering (turbidimetry), CD and ^{1}H-NMR demonstrated the higher ability of the former to interact with biopolymer and to induce chain reconfiguration by both. The demonstrated ability of not-traditional cross-linker PPi giving rise to the formation, by means of three-step process, of wall-to-wall hydrogels with tunable mechanical properties represents an innovation with great potential in biomedical field.

- A silver-containing antimicrobial membrane was successfully obtained. This nanocomposite material was proved to possess antimicrobial activity towards bacteria suspensions and mature biofilms. The stability of chitlac-coordinated AgNPs was not affected by mixture with chitosan and glycerol, enabling to prepare homogeneous macroscopic nanocomposite hydrogels and pliable membranes. Overall, the ability of AgNPs to enhance the antibacterial properties of chitosan, combined with the lack of cytotoxicity towards eukaryotic cell lines and the hydrophilic behavior of the construct, allow to consider this membrane as a promising biomaterial for the treatment of non-healing wounds.

- The ability of butyrate to dampen both pro-inflammatory cytokines production by stimulated macrophages and the respiratory burst of human neutrophils in a dose-manner is reported. The anti-inflammatory behavior of such molecule was also found to be time-dependent for the latter. As a consequence, the fabrication of smart reservoirs for butyrate was addressed. The stability in PBS medium of B-NPs with different composition was found being strongly affected mainly by the acetylation degree of chitosans. The stability, together with the surface charge, polydispersity and preliminary biological studies enabled to identify the most promising formulation (size: 287 ± 2 nm; surface charge: -23.0 ± 0.1 mV; polydispersity index: 0.18 ± 0.04). Related plain carrier demonstrated to behave as a radical scavenger and as a controlled release system. Considering all these aspects, together with the lack of cytotoxicity and mucoadhesive properties, complexes based on chitosan and hyaluronan may be considered as promising vehicles for the delivery of the anti-inflammatory butyrate molecule to inflamed tissues *in vivo*.

- SHLS12 proved straightforward antibacterial properties towards different bacteria strains grown both in planktonic and sessile conditions. Moreover, such activity was mostly not affected by the presence of physiological amounts of serum proteins. The lack of cytotoxicity towards eukaryotic cells was demonstrated with respect to two eukaryotic cell lines. The overall outcomes allow considering SHLS12 a promising biomaterial for further *in vivo* applications.

5. REFERENCES

1. B. K. Sun, Z. Siprashvili, P. A. Khavari, Advances in skin grafting and treatment of cutaneous wounds. *Science*. **346**, 941–5 (2014).

2. W. T. Lawrence, Physiology of the acute wound. *Clin. Plast. Surg.* **25**, 321–40 (1998).

3. J. G. Pool, Normal hemostatic mechanisms: a review. *Am. J. Med. Technol.* **43**, 776–80 (1977).

4. J. Jespersen, Pathophysiology and clinical aspects of fibrinolysis and inhibition of coagulation. Experimental and clinical studies with special reference to women on oral contraceptives and selected groups of thrombosis prone patients. *Dan. Med. Bull.* **35**, 1–33 (1988).

5. T. Velnar, T. Bailey, V. Smrkolj, The wound healing process: an overview of the cellular and molecular mechanisms. *J. Int. Med. Res.* **37**, 1528–42.

6. M. C. Robson, D. L. Steed, M. G. Franz, Wound healing: biologic features and approaches to maximize healing trajectories. *Curr. Probl. Surg.* **38**, 72–140 (2001).

7. J. Hart, Inflammation. 1: Its role in the healing of acute wounds. *J. Wound Care*. **11**, 205–9 (2002).

8. G. Broughton, J. E. Janis, C. E. Attinger, The basic science of wound healing. *Plast. Reconstr. Surg.* **117**, 12S–34S (2006).

9. H. L. Wright, R. J. Moots, S. W. Edwards, The multifactorial role of neutrophils in rheumatoid arthritis. *Nat. Rev. Rheumatol.* **10**, 593–601 (2014).

10. C. J. Sylvia, The role of neutrophil apoptosis in influencing tissue repair. *J. Wound Care*. **12**, 13–6 (2003).

11. G. R. Skover, Cellular and biochemical dynamics of wound repair. Wound environment in collagen regeneration. *Clin. Podiatr. Med. Surg.* **8**, 723–56 (1991).

12. K. Tschaikowsky, R. Sittl, G. G. Braun, W. Hering, E. Rügheimer, Increased fMet-Leu-Phe receptor expression and altered superoxide production of neutrophil granulocytes in septic and posttraumatic patients. *Clin. Investig.* **72**, 18–25 (1993).

13. G. F. Pierce, T. A. Mustoe, B. W. Altrock, T. F. Deuel, A. Thomason, Role of platelet-derived growth factor in wound healing. *J. Cell. Biochem.* **45**, 319–326 (1991).

14. S. S. Ramasastry, Acute wounds. *Clin. Plast. Surg.* **32**, 195–208 (2005).

15. W. J. Ennis, P. Meneses, Wound healing at the local level: the stunned wound.
Ostomy. Wound. Manage., **46**, 39-48 (2000).

16. T. K. Hunt, H. Hopf, Z. Hussain, Physiology of wound healing. *Adv. Skin Wound Care*. **13**, 6–11 (2000).

17. M. Y. Sieggreen, Healing of physical wounds. *Nurs. Clin. North Am.* **22**, 439–47 (1987).

18. R. Goldman, Growth factors and chronic wound healing: past, present, and future. *Adv. Skin Wound Care*. **17**, 24–35.

19. Y. Oike, Angiopoietin-related growth factor (AGF) promotes angiogenesis. *Blood*. **103**, 3760–3765 (2004).

20. D. Ribatti, A. Vacca, L. Roncali, F. Dammacco, Angiogenesis under normal and pathological conditions. *Haematologica*. **76**, 311–20.

21. V. P. Terranova *et al.*, Human endothelial cells are chemotactic to endothelial cell growth factor and heparin. *J. Cell Biol.* **101**, 2330–4 (1985).

22. C. L. Baum, C. J. Arpey, Normal cutaneous wound healing: clinical correlation with cellular and molecular events. *Dermatol. Surg.* **31**, 674-86 (2005).

23. R. A. Clark, Regulation of fibroplasia in cutaneous wound repair. *Am. J. Med. Sci.* **306**, 42–8 (1993).

24. G. D. Mulder, J. S. Vande Berg, Cellular senescence and matrix metalloproteinase activity in chronic wounds. Relevance to debridement and new technologies. *J. Am. Podiatr. Med. Assoc.* **92**, 34–7 (2002).

25. N. J. Percival, Classification of Wounds and their Management. *Surg.* **20**, 114–117 (2002).

26. K. G. Harding, H. L. Morris, G. K. Patel, Science, medicine and the future: healing chronic wounds. *BMJ*. **324**, 160–3 (2002).

27. T. Mustoe, Understanding chronic wounds: a unifying hypothesis on their pathogenesis and implications for therapy. *Am. J. Surg.* **187**, S65–S70 (2004).

28. G. Crovetti *et al.*, Platelet gel for healing cutaneous chronic wounds. *Transfus. Apher. Sci.* **30**, 145–51 (2004).

29. G. Zhao *et al.*, Biofilms and Inflammation in Chronic Wounds. *Adv. wound care*. **2**, 389–399 (2013).

30. L. Bolton, L. van Rijswijk, Wound dressings: meeting clinical and biological needs. *Dermatol. Nurs.* **3**, 146–61 (1991).

31. D. Krasner, K. L. Kennedy, B. S. Rolstad, A. W. Roma, *Ostomy. Wound. Manage.*, in press (available at http://www.ncbi.nlm.nih.gov/pubmed/8311909).

32. K. F. Cutting, R. J. White, Maceration of the skin and wound bed. 1: Its nature and causes. *J. Wound Care*. **11**, 275–8 (2002).

33. W. Y. Chen, A. A. Rogers, M. J. Lydon, Characterization of biologic properties of wound fluid collected during early stages of wound healing. *J. Invest. Dermatol.* **99**, 559–64 (1992).

34. S. J. Lee *et al.*, Electrospun chitosan nanofibers with controlled levels of silver nanoparticles. Preparation, characterization and antibacterial activity. *Carbohydr. Polym.* **111**, 530–537 (2014).

35. P. V Gawande, K. P. Leung, S. Madhyastha, Antibiofilm and antimicrobial efficacy of DispersinB®-KSL-W peptide-based wound gel against chronic wound infection associated bacteria. *Curr. Microbiol.* **68**, 635–41 (2014).

36. G. A. James *et al.*, Biofilms in chronic wounds. *Wound Repair Regen.* **16**, 37–44 (2008).

37. M. L. W. Knetsch, L. H. Koole, New Strategies in the Development of Antimicrobial Coatings: The Example of Increasing Usage of Silver and Silver Nanoparticles. *Polymers (Basel).* **3**, 340–366 (2011).

38. R. Y. Pelgrift, A. J. Friedman, Nanotechnology as a therapeutic tool to combat microbial resistance. *Adv. Drug Deliv. Rev.* **65**, 1803–15 (2013).

39. M. R. Parsek, P. K. Singh, Bacterial biofilms: an emerging link to disease pathogenesis. *Annu. Rev. Microbiol.* **57**, 677–701 (2003).

40. D. Lindsay, A. von Holy, Bacterial biofilms within the clinical setting: what healthcare professionals should know. *J. Hosp. Infect.* **64**, 313–325 (2006).

41. J. W. Costerton, P. S. Stewart, E. P. Greenberg, Bacterial biofilms: a common cause of persistent

infections. *Science*. **284**, 1318–22 (1999).

42. W. Costerton *et al.*, The application of biofilm science to the study and control of chronic bacterial infections. *J. Clin. Invest.* **112**, 1466–77 (2003).

43. P. G. Bowler, B. I. Duerden, D. G. Armstrong, Wound Microbiology and Associated Approaches to Wound Management. *Clin. Microbiol. Rev.* **14**, 244–269 (2001).

44. R. S. Howell-Jones, A review of the microbiology, antibiotic usage and resistance in chronic skin wounds. *J. Antimicrob. Chemother.* **55**, 143–149 (2005).

45. M. A. Fonder *et al.*, Treating the chronic wound: A practical approach to the care of nonhealing wounds and wound care dressings. *J. Am. Acad. Dermatol.* **58**, 185–206 (2008).

46. S. O'Meara, N. Cullum, M. Majid, T. Sheldon, Systematic reviews of wound care management: (3) antimicrobial agents for chronic wounds; (4) diabetic foot ulceration. *Health Technol. Assess.* **4**, 1–237 (2000).

47. G. R. Seabrook *et al.*, Comparison of serum and tissue antibiotic levels in diabetes-related foot infections. *Surgery*. **110**, 671-6 (1991).

48. A. S. Colsky, R. S. Kirsner, F. A. Kerdel, Analysis of antibiotic susceptibilities of skin wound flora in hospitalized dermatology patients. The crisis of antibiotic resistance has come to the surface. *Arch. Dermatol.* **134**, 1006–9 (1998).

49. D. Leaper, O. Assadian, C. E. Edmiston, Approach to chronic wound infections. *Br. J. Dermatol.* **173**, 351–8 (2015).

50. D. J. Leaper *et al.*, Extending the TIME concept: what have we learned in the past 10 years?(*). *Int. Wound J.* **9 Suppl 2**, 1–19 (2012).

51. D. Leaper, K. Harding, Antimicrobials and antiseptics. *J Wound Technol*, 34–5 (2010).

52. S. A. Kramer, Effect of povidone-iodine on wound healing: a review. *J. Vasc. Nurs.* **17**, 17–23 (1999).

53. H. . Klasen, A historical review of the use of silver in the treatment of burns. II. Renewed interest for silver. *Burns*. **26**, 131–138 (2000).

54. T. Uchihara, Silver diagnosis in neuropathology: principles, practice and revised interpretation. *Acta Neuropathol.* **113**, 483–99 (2007).

55. A. G. Skirtach *et al.*, Laser-induced release of encapsulated materials inside living cells. *Angew. Chem. Int. Ed. Engl.* **45**, 4612–7 (2006).

56. A. Travan *et al.*, Silver-polysaccharide nanocomposite antimicrobial coatings for methacrylic thermosets. *Acta Biomater.* **7**, 337–46 (2011).

57. N. Vigneshwaran, A. A. Kathe, P. V Varadarajan, R. P. Nachane, R. H. Balasubramanya, Functional finishing of cotton fabrics using silver nanoparticles. *J. Nanosci. Nanotechnol.* **7**, 1893–7 (2007).

58. T. Gunasekaran, T. Nigusse, M. D. Dhanaraju, Silver nanoparticles as real topical bullets for wound healing. *J. Am. Coll. Clin. Wound Spec.* **3**, 82–96 (2011).

59. T. Tsuji, K. Iryo, N. Watanabe, M. Tsuji, Preparation of silver nanoparticles by laser ablation in solution: influence of laser wavelength on particle size. *Appl. Surf. Sci.* **202**, 80–85 (2002).

60. D. D. Evanoff, G. Chumanov, Synthesis and optical properties of silver nanoparticles and arrays. *Chemphyschem*. **6**, 1221–31 (2005).

61. A. Pyatenko, M. Yamaguchi, M. Suzuki, Synthesis of Spherical Silver Nanoparticles with Controllable Sizes in Aqueous Solutions. *J. Phys. Chem. C*. **111**, 7910–7917 (2007).

62. A. Travan *et al.*, Non-cytotoxic silver nanoparticle-polysaccharide nanocomposites with antimicrobial activity. *Biomacromolecules*. **10**, 1429–35 (2009).

63. K. T. Nam, Y. J. Lee, E. M. Krauland, S. T. Kottmann, A. M. Belcher, Peptide-mediated reduction of silver ions on engineered biological scaffolds. *ACS Nano*. **2**, 1480–6 (2008).

64. B. S. Anisha, R. Biswas, K. P. Chennazhi, R. Jayakumar, Chitosan-hyaluronic acid/nano silver composite sponges for drug resistant bacteria infected diabetic wounds. *Int. J. Biol. Macromol.* **62**, 310–20 (2013).

65. L. Sintubin, W. Verstraete, N. Boon, Biologically produced nanosilver: current state and future perspectives. *Biotechnol. Bioeng.* **109**, 2422–36 (2012).

66. Z. Xiu, Q. Zhang, H. L. Puppala, V. L. Colvin, P. J. J. Alvarez, Negligible particle-specific antibacterial activity of silver nanoparticles. *Nano Lett.* **12**, 4271–5 (2012).

67. J. R. Morones *et al.*, The bactericidal effect of silver nanoparticles. *Nanotechnology*. **16**, 2346–53 (2005).

68. K. Madhumathi *et al.*, Development of novel chitin/nanosilver composite scaffolds for wound dressing applications. *J. Mater. Sci. Mater. Med.* **21**, 807–13 (2010).

69. Q. L. Feng *et al.*, A mechanistic study of the antibacterial effect of silver ions on Escherichia coli and Staphylococcus aureus. *J. Biomed. Mater. Res.* **52**, 662–8 (2000).

70. I. Sondi, B. Salopek-Sondi, Silver nanoparticles as antimicrobial agent: a case study on E. coli as a model for Gram-negative bacteria. *J. Colloid Interface Sci.* **275**, 177–82 (2004).

71. J. Chen, F. Wang, Q. Liu, J. Du, Antibacterial polymeric nanostructures for biomedical applications. *Chem. Commun. (Camb).* **50**, 14482–93 (2014).

72. Y.-H. Lee *et al.*, Cytotoxicity, oxidative stress, apoptosis and the autophagic effects of silver nanoparticles in mouse embryonic fibroblasts. *Biomaterials*. **35**, 4706–15 (2014).

73. T. Paz-Elizur *et al.*, DNA repair of oxidative DNA damage in human carcinogenesis: potential application for cancer risk assessment and prevention. *Cancer Lett.* **266**, 60–72 (2008).

74. M. Chen, A. von Mikecz, Formation of nucleoplasmic protein aggregates impairs nuclear function in response to SiO2 nanoparticles. *Exp. Cell Res.* **305**, 51–62 (2005).

75. E. Marsich *et al.*, Biological responses of silver-coated thermosets: an in vitro and in vivo study. *Acta Biomater.* **9**, 5088–99 (2013).

76. S. Nganga *et al.*, In vitro antimicrobial properties of silver-polysaccharide coatings on porous fiber-reinforced composites for bone implants. *J. Mater. Sci. Mater. Med.* **24**, 2775–85 (2013).

77. E. Marsich *et al.*, Nano-composite scaffolds for bone tissue engineering containing silver nanoparticles: preparation, characterization and biological properties. *J. Mater. Sci. Mater. Med.* **24**, 1799–807 (2013).

78. S. R. Karukonda *et al.*, The effects of drugs on wound healing--part II. Specific classes of drugs and their effect on healing wounds. *Int. J. Dermatol.* **39**, 321–33 (2000).

79. R. Bahramsoltani, M. H. Farzaei, R. Rahimi, Medicinal plants and their natural components as future drugs for the treatment of burn wounds: an integrative review. *Arch. Dermatol. Res.* **306**, 601–17 (2014).

80. J. Majtan, Honey: an immunomodulator in wound healing. *Wound Repair Regen.* **22**, 187–92 (2014).

81. P. Louis *et al.*, Restricted Distribution of the Butyrate Kinase Pathway among Butyrate-Producing Bacteria from the Human Colon. *J. Bacteriol.* **186**, 2099–2106 (2004).

82. P. Louis, G. L. Hold, H. J. Flint, The gut microbiota, bacterial metabolites and colorectal cancer. *Nat. Rev. Microbiol.* **12**, 661–72 (2014).

83. J. Tan *et al.*, The role of short-chain fatty acids in health and disease. *Adv. Immunol.* **121**, 91–119 (2014).

84. C. Dianzani *et al.*, Cholesteryl butyrate solid lipid nanoparticles inhibit adhesion of human neutrophils to endothelial cells. *Br. J. Pharmacol.* **148**, 648–56 (2006).

85. M. A. R. Vinolo *et al.*, Short-chain fatty acids stimulate the migration of neutrophils to inflammatory sites. *Clin. Sci. (Lond).* **117**, 331–8 (2009).

86. C. Eftimiadi, M. Tonetti, A. Cavallero, O. Sacco, G. A. Rossi, Short-chain fatty acids produced by anaerobic bacteria inhibit phagocytosis by human lung phagocytes. *J. Infect. Dis.* **161**, 138–42 (1990).

87. M. A. R. Vinolo *et al.*, Suppressive effect of short-chain fatty acids on production of proinflammatory mediators by neutrophils. *J. Nutr. Biochem.* **22**, 849–855 (2011).

88. K. M. Maslowski *et al.*, Regulation of inflammatory responses by gut microbiota and chemoattractant receptor GPR43. *Nature*. **461**, 1282–6 (2009).

89. M. A. R. Vinolo, E. Hatanaka, R. H. Lambertucci, P. Newsholme, R. Curi, Effects of short chain fatty acids on effector mechanisms of neutrophils. *Cell Biochem. Funct.* **27**, 48–55 (2009).

90. K. Y. C. Fung, L. Cosgrove, T. Lockett, R. Head, D. L. Topping, A review of the potential mechanisms for the lowering of colorectal oncogenesis by butyrate. *Br. J. Nutr.* **108**, 820–31 (2012).

91. P. Daniel *et al.*, Pharmacokinetic study of butyric acid administered in vivo as sodium and arginine butyrate salts. *Clin. Chim. Acta.* **181**, 255–63 (1989).

92. A. A. Miller, E. Kurschel, R. Osieka, C. G. Schmidt, Clinical pharmacology of sodium butyrate in patients with acute leukemia. *Eur. J. Cancer Clin. Oncol.* **23**, 1283–7 (1987).

93. L. Serpe *et al.*, Cholesteryl butyrate solid lipid nanoparticles as a butyric acid pro-drug: effects on cell proliferation, cell-cycle distribution and c-myc expression in human leukemic cells. *Anticancer. Drugs*. **15**, 525–36 (2004).

94. K. Zaher, M. El Kolli, F. Riahi, R. Doufnoune, Preparation and Characterization of Hydrocolloid Biopolymer-Based Films for Dressing Applications. *Int. J. Polym. Mater.* **58**, 665–680 (2009).

95. C. Weller, G. Sussman, Wound Dressings Update. *J. Pharm. Pract. Res.* **36**, 318–324 (2006).

96. L. M. Morton, T. J. Phillips, Wound healing update. *Semin. Cutan. Med. Surg.* **31**, 33–7 (2012).

97. L. L. Lloyd, J. F. Kennedy, P. Methacanon, M. Paterson, C. J. Knill, Carbohydrate polymers as wound management aids. *Carbohydr. Polym.* **37**, 315–322 (1998).

98. R. J. Morin, N. L. Tomaselli, Interactive dressings and topical agents. *Clin. Plast. Surg.* **34**, 643–58 (2007).

99. J. C. Dumville, M. O. Soares, S. O'Meara, N. Cullum, Systematic review and mixed treatment comparison: dressings to heal diabetic foot ulcers. *Diabetologia*. **55**, 1902–10 (2012).

100. J. Berger *et al.*, Structure and interactions in covalently and ionically crosslinked chitosan hydrogels

for biomedical applications. *Eur. J. Pharm. Biopharm.* **57**, 19–34 (2004).

101. J. S. Boateng, K. H. Matthews, H. N. E. Stevens, G. M. Eccleston, Wound healing dressings and drug delivery systems: a review. *J. Pharm. Sci.* **97**, 2892–923 (2008).

102. K. Kawai, S. Suzuki, Y. Tabata, Y. Nishimura, Accelerated wound healing through the incorporation of basic fibroblast growth factor-impregnated gelatin microspheres into artificial dermis using a pressure-induced decubitus ulcer model in genetically diabetic mice. *Br. J. Plast. Surg.* **58**, 1115–23 (2005).

103. V. Arul *et al.*, Glucose oxidase incorporated collagen matrices for dermal wound repair in diabetic rat models: a biochemical study. *J. Biomater. Appl.* **26**, 917–38 (2012).

104. N. Kanda *et al.*, Evaluation of a novel collagen-gelatin scaffold for achieving the sustained release of basic fibroblast growth factor in a diabetic mouse model. *J. Tissue Eng. Regen. Med.* **8**, 29–40 (2014).

105. A. M. Breen, P. Dockery, T. O'Brien, A. S. Pandit, The use of therapeutic gene eNOS delivered via a fibrin scaffold enhances wound healing in a compromised wound model. *Biomaterials*. **29**, 3143–51 (2008).

106. D. C. S. Pedroso *et al.*, Improved survival, vascular differentiation and wound healing potential of stem cells co-cultured with endothelial cells. *PLoS One*. **6**, e16114 (2011).

107. P. Inpanya, A. Faikrua, A. Ounaroon, A. Sittichokechaiwut, J. Viyoch, Effects of the blended fibroin/aloe gel film on wound healing in streptozotocin-induced diabetic rats. *Biomed. Mater.* **7**, 035008 (2012).

108. P. Koria *et al.*, Self-assembling elastin-like peptides growth factor chimeric nanoparticles for the treatment of chronic wounds. *Proc. Natl. Acad. Sci. U. S. A.* **108**, 1034–9 (2011).

109. W. Wang *et al.*, Acceleration of diabetic wound healing with chitosan-crosslinked collagen sponge containing recombinant human acidic fibroblast growth factor in healing-impaired STZ diabetic rats. *Life Sci.* **82**, 190–204 (2008).

110. R. Lobmann, D. Pittasch, I. Mühlen, H. Lehnert, Autologous human keratinocytes cultured on membranes composed of benzyl ester of hyaluronic acid for grafting in nonhealing diabetic foot lesions: a pilot study. *J. Diabetes Complications*. **17**, 199–204.

111. L. Sobotka, A. Smahelova, J. Pastorova, M. Kusalova, A case report of the treatment of diabetic foot ulcers using a sodium hyaluronate and iodine complex. *Int. J. Low. Extrem. Wounds*. **6**, 143–7 (2007).

112. Y. Matsumoto, Y. Kuroyanagi, Development of a wound dressing composed of hyaluronic acid sponge containing arginine and epidermal growth factor. *J. Biomater. Sci. Polym. Ed.* **21**, 715–26 (2010).

113. L. Abbruzzese *et al.*, Effectiveness and safety of a novel gel dressing in the management of neuropathic leg ulcers in diabetic patients: a prospective double-blind randomized trial. *Int. J. Low. Extrem. Wounds*. **8**, 134–40 (2009).

114. R. Jung, Y. Kim, H.-S. Kim, H.-J. Jin, Antimicrobial properties of hydrated cellulose membranes with silver nanoparticles. *J. Biomater. Sci. Polym. Ed.* **20**, 311–24 (2009).

115. D. S. Choi *et al.*, Hydrogel incorporated with chestnut honey accelerates wound healing and promotes early HO-1 protein expression in diabetic (db/db) mice. *Tissue Eng. Regen. Med.* **9**, 36–42 (2012).

116. J. Shaw *et al.*, The effect of topical phenytoin on healing in diabetic foot ulcers: a randomized controlled trial. *Diabet. Med.* **28**, 1154–7 (2011).

117. S. Manju, M. Antony, K. Sreenivasan, Synthesis and evaluation of a hydrogel that binds glucose and releases ciprofloxacin. *J. Mater. Sci.* **45**, 4006–4012 (2010).

118. J. S. Choi, S. H. Choi, H. S. Yoo, Coaxial electrospun nanofibers for treatment of diabetic ulcers with binary release of multiple growth factors. *J. Mater. Chem.* **21**, 5258 (2011).

119. Y. Li, P. I. Lee, Controlled nitric oxide delivery platform based on S-nitrosothiol conjugated interpolymer complexes for diabetic wound healing. *Mol. Pharm.* **7**, 254–66 (2010).

120. X. Dong *et al.*, Repair effect of diabetic ulcers with recombinant human epidermal growth factor loaded by sustained-release microspheres. *Sci. China. C. Life Sci.* **51**, 1039–44 (2008).

121. J. G. Merrell *et al.*, Curcumin-loaded poly(epsilon-caprolactone) nanofibres: diabetic wound dressing with anti-oxidant and anti-inflammatory properties. *Clin. Exp. Pharmacol. Physiol.* **36**, 1149–56 (2009).

122. Y. Yang *et al.*, Promotion of skin regeneration in diabetic rats by electrospun core-sheath fibers loaded with basic fibroblast growth factor. *Biomaterials*. **32**, 4243–54 (2011).

123. L. I. F. Moura, A. M. A. Dias, E. Carvalho, H. C. de Sousa, Recent advances on the development of wound dressings for diabetic foot ulcer treatment--a review. *Acta Biomater.* **9**, 7093–114 (2013).

124. G. D. Mogoşanu, A. M. Grumezescu, Natural and synthetic polymers for wounds and burns dressing. *Int. J. Pharm.* **463**, 127–36 (2014).

125. K. M. Vårum, O. Smidsrød, Structure-Property Relationship in Chitosans, in *Polysaccharides: Structural Diversity and Functional Versatility*, CRC Press, Second., 2004; vol. 30, pp. 625–642.

126. G. A. F. Roberts, *Chitin Chemistry*, Houndmills, UK, 1992.

127. K. M. Vårum, M. W. Anthonsen, H. Grasdalen, O. Smidsrød, Determination of the degree of N-acetylation and the distribution of N-acetyl groups in partially N-deacetylated chitins (chitosans) by high-field n.m.r. spectroscopy. *Carbohydr. Res.* **211**, 17–23 (1991).

128. K. M. Vårum, M. H. Ottøy, O. Smidsrød, Water-solubility of partially N-acetylated chitosans as a function of pH: effect of chemical composition and depolymerisation. *Carbohydr. Polym.* **25**, 65–70 (1994).

129. T. Sannan, K. Kurita, Y. Iwakura, Studies on chitin, 2. Effect of deacetylation on solubility. *Die Makromol. Chemie*. **177**, 3589–3600 (1976).

130. A. Domard, pH and c.d. measurements on a fully deacetylated chitosan: application to CuII—polymer interactions. *Int. J. Biol. Macromol.* **9**, 98–104 (1987).

131. S. P. Strand, K. Tømmeraas, K. M. Vårum, K. Østgaard, Electrophoretic light scattering studies of chitosans with different degrees of N-acetylation. *Biomacromolecules*. **2**, 1310–4 (2001).

132. M. W. Anthonsen, O. Smidsrød, Hydrogen ion titration of chitosans with varying degrees of N-acetylation by monitoring induced 1H-NMR chemical shifts. *Carbohydr. Polym.* **26**, 303–305 (1995).

133. P. Sorlier, A. Denuzière, C. Viton, A. Domard, Relation between the Degree of Acetylation and the Electrostatic Properties of Chitin and Chitosan. *Biomacromolecules*. **2**, 765–772 (2001).

134. I. M. Garnica-Palafox *et al.*, Mechanical and structural response of a hybrid hydrogel based on chitosan and poly(vinyl alcohol) cross-linked with epichlorohydrin for potential use in tissue engineering. *J. Biomater. Sci. Polym. Ed.* **25**, 32–50 (2014).

135. M. Grolik *et al.*, Hydrogel membranes based on genipin-cross-linked chitosan blends for corneal

epithelium tissue engineering. *J. Mater. Sci. Mater. Med.* **23**, 1991–2000 (2012).

136. W. Kangjian, D. Nianhua, X. Shiwei, Y. Yichun, D. Weihua, Preparation and characterization of collagen-chitosan-chondroitin sulfate composite membranes. *J. Membr. Biol.* **245**, 707–16 (2012).

137. S. S. Silva, S. G. Caridade, J. F. Mano, R. L. Reis, Effect of crosslinking in chitosan/aloe vera-based membranes for biomedical applications. *Carbohydr. Polym.* **98**, 581–8 (2013).

138. A. Montembault, C. Viton, A. Domard, Rheometric study of the gelation of chitosan in aqueous solution without cross-linking agent. *Biomacromolecules*. **6**, 653–62 (2005).

139. N. Boucard, C. Viton, A. Domard, New aspects of the formation of physical hydrogels of chitosan in a hydroalcoholic medium. *Biomacromolecules*. **6**, 3227–37 (2005).

140. M. V Risbud, A. A. Hardikar, S. V Bhat, R. R. Bhonde, pH-sensitive freeze-dried chitosan–polyvinyl pyrrolidone hydrogels as controlled release system for antibiotic delivery. *J. Control. Release*. **68**, 23–30 (2000).

141. E. P. Minet *et al.*, Slow delivery of a nitrification inhibitor (dicyandiamide) to soil using a biodegradable hydrogel of chitosan. *Chemosphere*. **93**, 2854–8 (2013).

142. C. Ji, A. Khademhosseini, F. Dehghani, Enhancing cell penetration and proliferation in chitosan hydrogels for tissue engineering applications. *Biomaterials*. **32**, 9719–29 (2011).

143. L. Cui, J. Jia, Y. Guo, Y. Liu, P. Zhu, Preparation and characterization of IPN hydrogels composed of chitosan and gelatin cross-linked by genipin. *Carbohydr. Polym.* **99**, 31–8 (2014).

144. F. Pati, B. Adhikari, S. Dhara, Development of chitosan-tripolyphosphate fibers through pH dependent ionotropic gelation. *Carbohydr. Res.* **346**, 2582–8 (2011).

145. A. Rampino, M. Borgogna, P. Blasi, B. Bellich, A. Cesàro, Chitosan nanoparticles: Preparation, size evolution and stability. *Int. J. Pharm.* **455**, 219–228 (2013).

146. H. Ueno *et al.*, Evaluation effects of chitosan for the extracellular matrix production by fibroblasts and the growth factors production by macrophages. *Biomaterials*. **22**, 2125–2130 (2001).

147. G. I. Howling *et al.*, The effect of chitin and chitosan on the proliferation of human skin fibroblasts and keratinocytes in vitro. *Biomaterials*. **22**, 2959–66 (2001).

148. M. Kong, X. G. Chen, K. Xing, H. J. Park, Antimicrobial properties of chitosan and mode of action: a state of the art review. *Int. J. Food Microbiol.* **144**, 51–63 (2010).

149. A. K. Azad, N. Sermsintham, S. Chandrkrachang, W. F. Stevens, Chitosan membrane as a wound-healing dressing: characterization and clinical application. *J. Biomed. Mater. Res. B. Appl. Biomater.* **69**, 216–22 (2004).

150. V. Thomas, M. M. Yallapu, B. Sreedhar, S. K. Bajpai, Fabrication, Characterization of Chitosan/Nanosilver Film and Its Potential Antibacterial Application. *J. Biomater. Sci. Polym. Ed.* **20**, 2129–2144 (2009).

151. A. D. Sezer *et al.*, Chitosan film containing fucoidan as a wound dressing for dermal burn healing: preparation and in vitro/in vivo evaluation. *AAPS PharmSciTech*. **8**, 39 (2007).

152. S. S. Silva *et al.*, An investigation of the potential application of chitosan/aloe-based membranes for regenerative medicine. *Acta Biomater.* **9**, 6790–7 (2013).

153. H. B. TVL, M. Vidyavathi, K. K, T. Sastry, S. kumar RV, Preparation and evaluation of ciprofloxacin loaded chitosan-gelatin composite films for wound healing activity. *Int. J. Drug Deliv.* **2** (2010).

154. M. PANDIMA DEVI *et al.*, A novel wound dressing material — fibrin–chitosan–sodium alginate composite sheet. *Bull. Mater. Sci.* **35**, 1157–1163 (2013).

155. P. T. Sudheesh Kumar *et al.*, In vitro and in vivo evaluation of microporous chitosan hydrogel/nanofibrin composite bandage for skin tissue regeneration. *Tissue Eng. Part A*. **19**, 380–92 (2013).

156. G. Kogan, L. Soltés, R. Stern, P. Gemeiner, Hyaluronic acid: a natural biopolymer with a broad range of biomedical and industrial applications. *Biotechnol. Lett.* **29**, 17–25 (2007).

157. D. Jiang, J. Liang, P. W. Noble, Hyaluronan in tissue injury and repair. *Annu. Rev. Cell Dev. Biol.* **23**, 435–61 (2007).

158. H. G. Garg, C. A. Hales, Eds., *Chemistry and Biology of Hyaluronan* (Elsevier Ltd, 2004).

159. Y.-S. Cho *et al.*, Hyaluronic acid and silver sulfadiazine-impregnated polyurethane foams for wound dressing application. *J. Mater. Sci. Mater. Med.* **13**, 861–5 (2002).

160. D. Eng, M. Caplan, M. Preul, A. Panitch, Hyaluronan scaffolds: a balance between backbone functionalization and bioactivity. *Acta Biomater.* **6**, 2407–14 (2010).

161. W. Chen, Preparation of hyaluronan-DNA matrices and films. *Cold Spring Harb. Protoc.* **2012**, 1117–20 (2012).

162. I. Donati *et al.*, The aggregation of pig articular chondrocyte and synthesis of extracellular matrix by a lactose-modified chitosan. *Biomaterials*. **26**, 987–98 (2005).

163. R. Lapasin, S. Pricl, *Rheology of industrial polysaccharides: theory and applications* (1995).

164. T. K. L. Meyvis, S. C. De Smedt, J. Demeester, W. E. Hennink, Rheological monitoring of long-term degrading polymer hydrogels. *J. Rheol. (N. Y. N. Y).* **43**, 933 (1999).

165. H. T. Edzes, Determination of the resonance frequency ratio of the31P and1H NMR resonance shift standards 85% orthophosphoric acid and tetramethylsilane. *Magn. Reson. Chem.* **30**, 850–854 (1992).

166. R. K. Harris, E. D. Becker, S. M. Cabral de Menezes, R. Goodfellow, P. Granger, in *Magnetic Resonance in Chemistry* (2002), vol. 40, pp. 489–505.

167. P. Calvo, C. Remunan-Lopez, J. L. Vila-Jato, M. J. Alonso, Novel hydrophilic chitosan-polyethylene oxide nanoparticles as protein carriers. *J. Appl. Polym. Sci.* **63**, 125–132 (1997).

168. P. Sacco *et al.*, Polysaccharide-Based Networks from Homogeneous Chitosan-Tripolyphosphate Hydrogels: Synthesis and Characterization. *Biomacromolecules*. **15**, 3396–405 (2014).

169. G. Skjåk-Bræk, H. Grasdalen, O. Smidsrød, Inhomogeneous polysaccharide ionic gels. *Carbohydr. Polym.* **10**, 31–54 (1989).

170. Y. Huang, Y. Lapitsky, Monovalent salt enhances colloidal stability during the formation of chitosan/tripolyphosphate microgels. *Langmuir*. **27**, 10392–9 (2011).

171. G. Berth, H. Dautzenberg, The degree of acetylation of chitosans and its effect on the chain conformation in aqueous solution. *Carbohydr. Polym.* **47**, 39–51 (2002).

172. G. Turco *et al.*, Mechanical spectroscopy and relaxometry on alginate hydrogels: a comparative analysis for structural characterization and network mesh size determination. *Biomacromolecules*. **12**, 1272–82 (2011).

173. H.-J. Kong, K. Y. Lee, D. J. Mooney, Decoupling the dependence of rheological/mechanical properties of hydrogels from solids concentration. *Polymer (Guildf).* **43**, 6239–6246 (2002).

174. Q. Wang, Z. Dong, Y. Du, J. F. Kennedy, Controlled release of ciprofloxacin hydrochloride from chitosan/polyethylene glycol blend films. *Carbohydr. Polym.* **69**, 336–343 (2007).

175. A. Pawlak, M. Mucha, Thermogravimetric and FTIR studies of chitosan blends. *Thermochim. Acta*. **396**, 153–166 (2003).

176. J. Ostrowska-Czubenko, M.; Gierszewska-Drużyńska, in *Progress on chemistry and application of chitin and its derivative, Volume XV*, M.M. Jaworska, Ed. (Polish Chitin Society, Łódź, 2010), pp. 25–32.

177. D. H. M. James G. Colson, Quantitative analysis by phosphorus-31 nuclear magnetic resonance spectrometry. *Anal. Chem.* **45**, 370–371 (1973).

178. P. Hrynczyszyn, A. Jastrzebska, E. Szłyk, Determination of phosphate compounds in meat products by 31-phosphorus nuclear magnetic resonance spectroscopy with methylenediphosphonic acid after alkaline extraction. *Anal. Chim. Acta*. **673**, 73–8 (2010).

179. S. E. Manahan, *Environmental Chemistry* (CRC Press LLC, Boca Raton, Seventh ed., 2010).

180. Y. Huang, Y. Lapitsky, Determining the colloidal behavior of ionically cross-linked polyelectrolytes with isothermal titration calorimetry. *J. Phys. Chem. B*. **117**, 9548–57 (2013).

181. Y. Cai, Y. Lapitsky, Formation and dissolution of chitosan/pyrophosphate nanoparticles: is the ionic crosslinking of chitosan reversible? *Colloids Surf. B. Biointerfaces*. **115**, 100–8 (2014).

182. F.-L. Mi, C.-T. Chen, Y.-C. Tseng, C.-Y. Kuan, S.-S. Shyu, Iron(III)-carboxymethylchitin microsphere for the pH-sensitive release of 6-mercaptopurine. *J. Control. Release*. **44**, 19–32 (1997).

183. F.-L. Mi *et al.*, Chitosan-polyelectrolyte complexation for the preparation of gel beads and controlled release of anticancer drug. II. Effect of pH-dependent ionic crosslinking or interpolymer complex using tripolyphosphate or polyphosphate as reagent. *J. Appl. Polym. Sci.* **74**, 1093–1107 (1999).

184. T. López-León, E. L. S. Carvalho, B. Seijo, J. L. Ortega-Vinuesa, D. Bastos-González, Physicochemical characterization of chitosan nanoparticles: electrokinetic and stability behavior. *J. Colloid Interface Sci.* **283**, 344–51 (2005).

185. G. Zheng, W. S. Price, Solvent signal suppression in NMR. *Prog. Nucl. Magn. Reson. Spectrosc.* **56**, 267–88 (2010).

186. C. K. Kuo, P. X. Ma, Ionically crosslinked alginate hydrogels as scaffolds for tissue engineering: part 1. Structure, gelation rate and mechanical properties. *Biomaterials*. **22**, 511–21 (2001).

187. M. Garcia-Fuentes, M. J. Alonso, Chitosan-based drug nanocarriers: where do we stand? *J. Control. Release*. **161**, 496–504 (2012).

188. W. Fan, W. Yan, Z. Xu, H. Ni, Formation mechanism of monodisperse, low molecular weight chitosan nanoparticles by ionic gelation technique. *Colloids Surf. B. Biointerfaces*. **90**, 21–7 (2012).

189. Y. Huang, Y. Lapitsky, Salt-assisted mechanistic analysis of chitosan/tripolyphosphate micro- and nanogel formation. *Biomacromolecules*. **13**, 3868–76 (2012).

190. I. Donati *et al.*, New hypothesis on the role of alternating sequences in calcium-alginate gels. *Biomacromolecules*. **6**, 1031–40.

191. I. Geremia *et al.*, Determination of the composition for binary mixtures of polyanions: the case of mixed solutions of alginate and hyaluronan. *Biomacromolecules*. **15**, 1069–73 (2014).

192. G. Paradossi, E. Chiessi, M. Venanzi, B. Pispisa, A. Palleschi, Branched-chain analogues of linear polysaccharides: a spectroscopic and conformational investigation of chitosan derivatives. *Int. J. Biol. Macromol.* **14**, 73–80 (1992).

193. C. Bustamante, I. Tinoco, M. F. Maestre, Circular differential scattering can be an important part of the circular dichroism of macromolecules. *Proc. Natl. Acad. Sci. U. S. A.* **80**, 3568–72 (1983).

194. R. Novoa-Carballal, E. Fernandez-Megia, R. Riguera, Dynamics of chitosan by (1)h NMR relaxation. *Biomacromolecules*. **11**, 2079–86 (2010).

195. Y. Lapitsky, Ionically crosslinked polyelectrolyte nanocarriers: Recent advances and open problems. *Curr. Opin. Colloid Interface Sci.* **19**, 122–130 (2014).

196. I. Donati *et al.*, Polyol synthesis of silver nanoparticles: mechanism of reduction by alditol bearing polysaccharides. *Biomacromolecules*. **10**, 210–3 (2009).

197. E. Brambilla *et al.*, Biofilm formation on composite resins for dental restorations: an in situ study on the effect of chlorhexidine mouthrinses. *Int. J. Artif. Organs*. **35**, 792–9 (2012).

198. A. Barui, R. Khare, S. Dhara, P. Banerjee, J. Chatterjee, Ex vivo bio-compatibility of honey-alginate fibrous matrix for HaCaT and 3T3 with prime molecular expressions. *J. Mater. Sci. Mater. Med.* **25**, 2659–67 (2014).

199. J. M. Silva *et al.*, Nanostructured 3D constructs based on chitosan and chondroitin sulphate multilayers for cartilage tissue engineering. *PLoS One*. **8**, e55451 (2013).

200. R. Menegazzi, S. Busetto, P. Dri, R. Cramer, P. Patriarca, Chloride ion efflux regulates adherence, spreading, and respiratory burst of neutrophils stimulated by tumor necrosis factor-alpha (TNF) on biologic surfaces. *J. Cell Biol.* **135**, 511–22 (1996).

201. P. Dri, R. Cramer, P. Spessotto, M. Romano, P. Patriarca, Eosinophil activation on biologic surfaces. Production of O2- in response to physiologic soluble stimuli is differentially modulated by extracellular matrix components and endothelial cells. *J. Immunol.* **147**, 613–20 (1991).

202. R. Menegazzi, R. Cramer, P. Patriarca, P. Scheurich, P. Dri, Evidence that tumor necrosis factor alpha (TNF)-induced activation of neutrophil respiratory burst on biologic surfaces is mediated by the p55 TNF receptor. *Blood*. **84**, 287–93 (1994).

203. X. Deng *et al.*, Hyaluronic acid-chitosan nanoparticles for co-delivery of MiR-34a and doxorubicin in therapy against triple negative breast cancer. *Biomaterials*. **35**, 4333–44 (2014).

204. S. Busetto, E. Trevisan, P. Patriarca, R. Menegazzi, A single-step, sensitive flow cytofluorometric assay for the simultaneous assessment of membrane-bound and ingested Candida albicans in phagocytosing neutrophils. *Cytometry. A*. **58**, 201–6 (2004).

205. J. M. McCord, I. Fridovich, Superoxide dismutase. An enzymic function for erythrocuprein (hemocuprein). *J. Biol. Chem.* **244**, 6049–55 (1969).

206. B. Tan, Z. Lu, S. Dong, G. Zhao, M.-S. Kuo, Derivatization of the tricarboxylic acid intermediates with O-benzylhydroxylamine for liquid chromatography-tandem mass spectrometry detection. *Anal. Biochem.* **465**, 134–47 (2014).

207. B. A. Kruskal, S. Shak, F. R. Maxfield, Spreading of human neutrophils is immediately preceded by a large increase in cytoplasmic free calcium. *Proc. Natl. Acad. Sci. U. S. A.* **83**, 2919–23 (1986).

208. M. de la Fuente, B. Seijo, M. J. Alonso, Novel hyaluronic acid-chitosan nanoparticles for ocular gene therapy. *Invest. Ophthalmol. Vis. Sci.* **49**, 2016–24 (2008).

209. A. Almalik *et al.*, Hyaluronic acid (HA) presentation as a tool to modulate and control the receptor-mediated uptake of HA-coated nanoparticles. *Biomaterials*. **34**, 5369–80 (2013).

210. H. V. Sæther, H. K. Holme, G. Maurstad, O. Smidsrød, B. T. Stokke, Polyelectrolyte complex formation using alginate and chitosan. *Carbohydr. Polym.* **74**, 813–821 (2008).

211. C. Schatz, A. Domard, C. Viton, C. Pichot, T. Delair, Versatile and efficient formation of colloids of biopolymer-based polyelectrolyte complexes. *Biomacromolecules*. **5**, 1882–92.

212. H. Dautzenberg, J. Kriz, Response of Polyelectrolyte Complexes to Subsequent Addition of Salts with Different Cations. *Langmuir*. **19**, 5204–5211 (2003).

213. Y. Parajó, I. D'Angelo, A. Welle, M. Garcia-Fuentes, M. J. Alonso, Hyaluronic acid/Chitosan nanoparticles as delivery vehicles for VEGF and PDGF-BB. *Drug Deliv.* **17**, 596–604 (2010).

214. D. Wu, T. Delair, Stabilization of chitosan/hyaluronan colloidal polyelectrolyte complexes in physiological conditions. *Carbohydr. Polym.* **119**, 149–58 (2015).

215. N. M. Zaki, A. Nasti, N. Tirelli, Nanocarriers for cytoplasmic delivery: cellular uptake and intracellular fate of chitosan and hyaluronic acid-coated chitosan nanoparticles in a phagocytic cell model. *Macromol. Biosci.* **11**, 1747–60 (2011).

216. A. Almalik, P. J. Day, N. Tirelli, HA-coated chitosan nanoparticles for CD44-mediated nucleic acid delivery. *Macromol. Biosci.* **13**, 1671–80 (2013).

217. S. Yang, Z. Guo, F. Miao, Q. Xue, S. Qin, The hydroxyl radical scavenging activity of chitosan, hyaluronan, starch and their O-carboxymethylated derivatives. *Carbohydr. Polym.* **82**, 1043–1045 (2010).

218. I. A. Sogias, A. C. Williams, V. V Khutoryanskiy, Why is chitosan mucoadhesive? *Biomacromolecules*. **9**, 1837–42 (2008).

219. F. Picotti *et al.*, Hyaluronic acid lipoate: synthesis and physicochemical properties. *Carbohydr. Polym.* **93**, 273–8 (2013).

220. P. Sacco, A. Travan, M. Borgogna, S. Paoletti, E. Marsich, Silver-containing antimicrobial membrane based on chitosan-TPP hydrogel for the treatment of wounds. *J. Mater. Sci. Mater. Med.* **26**, 128 (2015).

221. S. J. Lee *et al.*, Electrospun chitosan nanofibers with controlled levels of silver nanoparticles. Preparation, characterization and antibacterial activity. *Carbohydr. Polym.* **111**, 530–7 (2014).

222. J. Yang, H. Zheng, S. Han, Z. Jiang, X. Chen, The synthesis of nano-silver/sodium alginate composites and their antibacterial properties. *RSC Adv.* **5**, 2378–2382 (2015).

223. A. M. Abdel-Mohsen *et al.*, Green synthesis of hyaluronan fibers with silver nanoparticles. *Carbohydr. Polym.* **89**, 411–22 (2012).

224. D. Chudobova *et al.*, Complexes of Silver(I) Ions and Silver Phosphate Nanoparticles with Hyaluronic Acid and/or Chitosan as Promising Antimicrobial Agents for Vascular Grafts. *Int. J. Mol. Sci.* **14**, 13592–614 (2013).

225. B. Deng, Y. Wang, P. Zhu, X. Xu, X. Ning, Study of the binding equilibrium between Zn(II) and HSA by capillary electrophoresis-inductively coupled plasma optical emission spectrometry. *Anal. Chim. Acta*. **683**, 58–62 (2010).

226. C. V Durgadas, C. P. Sharma, K. Sreenivasan, Fluorescent gold clusters as nanosensors for copper ions in live cells. *Analyst*. **136**, 933–40 (2011).

227. M. R. Duff, C. V Kumar, The metallomics approach: use of Fe(II) and Cu(II) footprinting to examine metal binding sites on serum albumins. *Metallomics*. **1**, 518–23 (2009).

228. W. Bal, M. Sokołowska, E. Kurowska, P. Faller, Binding of transition metal ions to albumin: sites, affinities and rates. *Biochim. Biophys. Acta*. **1830**, 5444–55 (2013).

229. X. Zhao, R. Liu, Y. Teng, X. Liu, The interaction between Ag+ and bovine serum albumin: a spectroscopic investigation. *Sci. Total Environ.* **409**, 892–7 (2011).

230. A.-K. Ostermeyer, C. Kostigen Mumuper, L. Semprini, T. Radniecki, Influence of bovine serum albumin and alginate on silver nanoparticle dissolution and toxicity to Nitrosomonas europaea. *Environ. Sci. Technol.* **47**, 14403–10 (2013).

231. K. M. Hindi *et al.*, The antimicrobial efficacy of sustained release silver-carbene complex-loaded L-tyrosine polyphosphate nanoparticles: characterization, in vitro and in vivo studies. *Biomaterials*. **30**, 3771–9 (2009).

232. L. Huang, T. Dai, Y. Xuan, G. P. Tegos, M. R. Hamblin, Synergistic combination of chitosan acetate with nanoparticle silver as a topical antimicrobial: efficacy against bacterial burn infections. *Antimicrob. Agents Chemother.* **55**, 3432–8 (2011).